PURE SPIN CURRENT IN LATERAL STRUCTURES

by

Shuhan Chen

A dissertation submitted to the Faculty of the University of Delaware in partial fulfillment of the requirements for the degree of Doctor of Philosophy in Physics

Winter 2016

© 2016 Shuhan Chen
All Rights Reserved

ProQuest Number: 10055780

All rights reserved

INFORMATION TO ALL USERS
The quality of this reproduction is dependent upon the quality of the copy submitted.

In the unlikely event that the author did not send a complete manuscript
and there are missing pages, these will be noted. Also, if material had to be removed,
a note will indicate the deletion.

ProQuest 10055780

Published by ProQuest LLC (2016). Copyright of the Dissertation is held by the Author.

All rights reserved.
This work is protected against unauthorized copying under Title 17, United States Code
Microform Edition © ProQuest LLC.

ProQuest LLC.
789 East Eisenhower Parkway
P.O. Box 1346
Ann Arbor, MI 48106 - 1346

PURE SPIN CURRENT IN LATERAL STRUCTURES

by

Shuhan Chen

Approved: _____
Edmund R. Nowak, Ph.D.
Chair of the Department of Physics and Astronomy

Approved: _____
George H. Watson, Ph.D.
Dean of the College of Arts and Sciences

Approved: _____
Ann L. Ardis, Ph.D.
Interim Vice Provost for Graduate & Professional Education

I certify that I have read this dissertation and that in my opinion it meets the academic and professional standard required by the University as a dissertation for the degree of Doctor of Philosophy.

Signed: _____

Yi Ji, Ph.D.
Professor in charge of dissertation

I certify that I have read this dissertation and that in my opinion it meets the academic and professional standard required by the University as a dissertation for the degree of Doctor of Philosophy.

Signed: _____

Siu-Tat Chui, Ph.D.
Member of dissertation committee

I certify that I have read this dissertation and that in my opinion it meets the academic and professional standard required by the University as a dissertation for the degree of Doctor of Philosophy.

Signed: _____

Matthew DeCamp, Ph.D.
Member of dissertation committee

I certify that I have read this dissertation and that in my opinion it meets the academic and professional standard required by the University as a dissertation for the degree of Doctor of Philosophy.

Signed: _____

Chaoying Ni, Ph.D.
Member of dissertation committee

ACKNOWLEDGMENTS

To all those who make this dissertation possible:

First and foremost, it would be my great pleasure to express my feeling of gratitude to my academic adviser: Dr. Yi Ji. Without his selfless help, I would not have these achievements. He has built up such an advanced lab that I can take advantage of, provided so much heritages and resources to make my research life much easier and supported me most of the time of my PhD study. His inspiring wisdom, persistent pursuit for truth and upright integrity will continuously encourage me for my future life.

I would like to thank the kind guidance and help from my committee members: Professor Siu-Tat Chui, Professor Matthew DeCamp and Professor Chaoying Ni for their help during my PhD study. Especial thanks are owed to Dr. Siu-Tat Chui, for my research would not reach a higher level without his wonderful theoretical work for our experiments.

I would like to thank the help and company over the years from my colleagues: Dr. Xiaojun Wang, Dr. Han Zou, Chuan Qin, Yunjiao Cai, Fatih Kandaz, Dr. Xin Fan, Dr. Xiaoming Kou, Dr. Qi Lu, Dr. Xing Chen, Dr. Jian Shen, Dr. Ping Chen, Dr. Yang Zhou, Dr. Chong Bi, Yunpeng Chen, Jun Wu, Yunsong Xie, Yukun Wang, Tao Wang, Paul Parsons, Dr. Ryan Stearrett, Kevin Haughey, Brain Kelly and Dr. Wanfeng Li. The illuminating interactions with them motivate me all the time.

I would like to thank all staff members at Department of Physics and Astronomy for their kind help over these years. I would like to thank Tom Reed and

Thomas Reilly for their wonderful job at the machine shop. I would also like to thank Rob Schmidt for his support on all the instruments and facility support.

At the end, I would like to express my deepest appreciation to my devoted parents in China. Thanks for their selfless love and support from the very beginning of my life. Their love is the permanent and peaceful harbor for my mind.

TABLE OF CONTENTS

LIST OF TABLES ix
LIST OF FIGURES x
ABSTRACT xv

Chapter

1 INTRODUCTION 1

REFERENCES 4

2 BACKGROUND OF MAGNETISM AND INTRODUCTION TO SPINTRONICS 5

2.1 History of the Discovery and Application of Magnetism 5
2.2 Magnetism: Hysteresis Loop 8
2.3 Magnetism: Spintronics 10

2.3.1 GMR: The Beginning of Spintronics 11
2.3.2 TMR: A Breakthrough for Spintronics 15

2.4 Introduction for Nonlocal Spin Valve 17
2.5 Motivation for Further Studies Related to NLSVs 24
2.6 The Spin Hall Effect 27

2.6.1 Introduction to the Spin Hall Effect 27
2.6.2 Controversies Over Spin Hall Effect Research 32

REFERENCES 36

3 EXPERIMENTAL METHODS 41

3.1 Lithography 41

3.1.1 Photolithography 41
3.1.2 Electron-Beam-Lithography 44

3.2 Electron Beam Evaporation 52

3.2.1 Principle 52
3.2.2 High Vacuum Chamber 53
3.2.3 Electron Beam Evaporation System and Deposition Process 54

3.3 Measurement Techniques 60
3.4 Cryogenic system 65

REFERENCES 67

4 ABSENCE OF HIGH SURFACE SPIN-FLIP RATE IN MESOSCOPIC SILVER CHANNELS 68

4.1 Introduction 68
4.2 Fabrication of Silver Channel Based NLSVs 69
4.3 Results Discussion 73
4.4 Conclusion 78

REFERENCES 79

5 ASYMMETRIC SPIN ABSORPTION ACROSS A LOW-RESISTANCE OXIDE BARRIER 81

5.1 Introduction 81
5.2 Fabrication of Unconventional Samples 82
5.3 Measurement and Discussion 85

5.3.1 Measurement Results 85
5.3.2 Asymmetric Spin Absorption 88
5.3.3 Reciprocal Measurements for Asymmetric Spin Injection 91

5.4 Conclusion 93

REFERENCES 95

6 LARGE SPIN ACCUMULATION NEAR A RESISTIVE INTERFACE DUE TO SPIN-CHARGE COUPLING 97

6.1 Introduction 97
6.2 Experiments 98

6.2.1 Regular nonlocal spin signal 98
6.2.2 Break-junction nonlocal spin valves 102

6.2.2.1 Break-junction: inverted spin signals from Py-Cu NLSVs 104

6.2.2.2 Break-junction: inverted spin signals from Co-Cu NLSVs 108
6.2.2.3 Break-junction: non-inverted spin signals from Py-Cu NLSVs 110

6.3 Theory 111

6.3.1 Basic Assumptions and Equations 111
6.3.2 Profiles of Electrochemical Potentials 117
6.3.3 Specific Examples of Non-inverted and Inverted Large Spin Signals 124

6.4 Conclusion 128

REFERENCES 129

7 EFFICIENT ROOM TEMPERATURE SPIN-HALL INJECTION ACROSS AN OXIDE BARRIER 131

7.1 Introduction 131
7.2 Experiments and Measurements 133

7.2.1 Sample Fabrication and Regular NLSV Measurements 133
7.2.2 SHE Measurement Set-up and Results 135
7.2.3 ISHE Measurement Set-up and Results 138

7.3 Discussion of Results: Estimation of Spin Hall Angle 139
7.4 Conclusion 142

REFERENCES 144

Appendix

A REPRINT PERMISSION LETTERS 146

LIST OF TABLES

Table 4.1: Estimated spin diffusion lengths (nm) of the silver channels assuming P = 0.21 at 4.5 K and P = 0.14 at 295 K. (Copyright (2015) The Japan Society of Applied Physics) 74

LIST OF FIGURES

Figure 2.1: A Hysteresis Loop..... 10

Figure 2.2: A schematic of mechanism of GMR: In the anti-parallel magnetic configuration (left), electrons with both spins will experience higher "spin resistance" in each magnetic layer and the external circuit will show a high resistance. In the parallel magnetic configuration (right), at least electrons with one of the spins will pass through both magnetic layers easily and the external circuit will show a low resistance. 13

Figure 2.3: Diagrams for CIP (left) CPP (right) configurations..... 15

Figure 2.4: Schematics for nonlocal spin valve with band structures of F_1, F_2 and N. The self-diffuse spin current will travel a distance called spin diffusion length from F_1 to F_2 and detected as a voltage contrast ΔVnl according to the spin orientation of F_2 manipulated by external magnetic field. 20

Figure 2.5: (a) A schematic of Mark Johnson's experiment for spin injection. A bar of pure bulk metal, about 50 μm thick and 100 μm wide, is coated with an insulating film. The distance between two electrodes is L. Reprinted with permission from [40]. 23

Figure 2.5: (b) Scanning electron microscope image of Jedema's device with a cobalt (Co) electrode spacing of $L = 650\ nm$. Current is sent from Co1 into the Al strip. The voltage is measured between Co2 and the right side of the Al strip. Reprinted with permission from [42]..... 23

Figure 2.6: A simple sketch for spin Hall effect (SHE). In some nonmagnetic normal materials, as a charge current passes through, a spin current will be generated in the transverse direction due to strong spin-orbit coupling and build up spin accumulation along the two edges. On the contrary, a spin current will induce electrical voltage detectable in the transverse direction, which is called inverse spin Hall effect (iSHE). 27

Figure 2.7: A scanning electron micrograph of the device and the measurement scheme for iSHE in Aluminum. Reprinted with permission from [72]. . 29

Figure 2.8: Left: a scanning electron microscope of Kimura's reversible SHE device. Right: a scheme for showing the arrangement of the device in 3D. Reprinted with permission from [73]. 30

Figure 2.9: (a) I. M. Miron's Hall cross device schematic and current-induced switching geometry. Black and white arrows indicate the "up" and "down" equilibrium magnetization states of the cobalt layer, respectively. Reprinted with permission from [83]. 32

Figure 2.9: (b) Sample geometry for the ST-FMR measurement in Luqiao Liu's experiments. IRF is the applied radio frequency current. HRF is the corresponding Oersted field. $\tau H = -M \times HRF$ is the torque on the magnetization due to the Oersted field and τST is the torque from the spin Hall effect. Reprinted with permission from [84]. 33

Figure 2.10: AlO_x/Co/Pt Hall cross with current and voltage leads. The thick arrows indicate the direction and amplitude of $T \perp$ (red) and $T \parallel$ (blue). The thin arrows indicate the equivalent fields $B \perp$ (red) and $B \parallel$ (blue). Reprinted with permission from [88]. 35

Figure 3.1: (a) Silicon wafer substrate with a clean surface; (b) spin coating for positive photoresist; (c) exposure with photo mask by UV light from photolithography machine; (d) development for exposed photoresist for leaving space for filling in materials; (e) deposition for desired materials; (f) lift-off photoresist residue, leaving only materials on substrate in designed patterns. (g) Photo pattern after lift-off, taken by optical at 100X. 43

Figure 3.2: A picture shows Raith e-LiNE machine we use in UMD. 46

Figure 3.3: (a) Clean substrate with pre-photolithography patterns; (b) spin coating with double layer e-beam resist PMGI and PMMA; (c) Exposure by e-beam lithography; (d) & (e) two-step development for forming space for filling in materials; (f) deposited desired materials; (g) lift-off resist residue leaving only designed patterns; (h-k) show the optical pictures took after PMMA development, PMGI development, e-beam evaporation separately. 52

Figure 3.4: A schematic drawing of the vacuum chamber in Ji's group (right side view). 54

Figure 3.5: A schematic shows the crucible holding evaporation materials and the self-seal protector above it. 57

Figure 3.6: A step-step illustration for fabrication of a nanoscale spin valve. (a) and (b): Py is deposited through different large angles from two orientations to ensure connection with NM materials from future deposition; (c) and (d): AlO_x and Cu are deposited through normal direction. 58

Figure 3.7: A schematic for e-beam angle evaporation for nanoscale structures. 59

Figure 3.8: General wire configuration for NLSV measurement. The switches stand by the switch box. 61

Figure 3.9: A picture for the measurement and cryogenic system in Ji's group. 64

Figure 3.10: A picture showing the electromagnets in Ji's group. 65

Figure 4.1: (a) SEM image of device #2. The Py spin detector is outlined using dashed lines to guide the eye. (b) Illustration of the angle deposition through a shadow mask made of PMMA/PMGI. (Copyright (2015) The Japan Society of Applied Physics) 70

Figure 4.2: (a) The R_S versus B curve for device #2 at 4.5 K showing ΔR_S = 38 mΩ; (b) The R_S versus B curve for device #2 at 295 K showing ΔR_S = 12 mΩ; (c) The ΔR_S versus T for devices #1 through #4. (Copyright (2015) The Japan Society of Applied Physics) 72

Figure 4.3: Cross-sectional views of the Ag channel during evaporation through the PMMA/PMGI shadow mask. (a) Initial stage of growth with isolated Ag islands; (b) coalescence of the Ag islands; (c) lateral expansion of the Ag channel on the substrate after coalescence. (Copyright (2015) The Japan Society of Applied Physics) 77

Figure 5.1: (a) SEM picture for our NLSV device. (b) Angle evaporation through a suspended resist mask. 84

Figure 5.2: Cartoon illustrations of (a) the "small-overlap" structure and (b) the "full-overlap" structure and the measurement configuration. Plot of the R_S versus B curves for the (c) small-overlap structure and the (d) full-overlap structure. 86

Figure 5.3: (a) A simple model which illustrates the asymmetric spin absorption across the $Cu/AlO_x/F_2$ interface. For the small-overlap structure, the magnetization under the interface behaves as a single domain. (b) For the full-overlap structure, it is possible that the two sections of the junction have different reversal fields and therefore a domain wall can be trapped underneath the junction between two reversal fields. The constructed curves of ε_1, -ε_2, and $Vnl \propto (\varepsilon 1 - \varepsilon 2)$ as functions of magnetic field *B* for (c) the small-overlap structure and (d) the full-overlap structure. 87

Figure 5.4: (a) The probe configuration of the reciprocal measurement. (b) A simple model that takes into account of the shunting effect of the Cu channel and the asymmetric spin injection. Plot of R_s versus *B* curve in the reciprocal measurement for (c) the small-overlap structure and (d) the full-overlap structure..... 92

Figure 6.1: (a) Cartoon illustration of a nonlocal spin valve. (b) SEM picture of a nonlocal spin valve. The scale bar represents 200 nm. (c) Nonlocal resistance R_s versus magnetic field *B* curve at 4.2 K. (d) R_s versus *B* curve at 295 K. (e) ΔR_s versus *L* curves on semi-log scale at 4.2 K (squares) and 295 K (circles) and fits (straight lines). 100

Figure 6.2: (a) Illustration of a break-junction NLSV structure. (b) SEM picture of a break-junction NLSV structure. The scale bar represents 200 nm. (c) R_s versus *B* curve of a Py/Cu break-junction NLSV measured at 100 Hz, (d) 346 Hz, and (e) 2000 Hz. 103

Figure 6.3: Evolution of R_s versus *B* curves for a Co-Cu break-junction NLSV structure at 4.2 K. (a) through (d) are arranged in temporal order. 107

Figure 6.4: Several non-inverted spin signals from Py-Cu break-junction NLSV structures. (a) Non-inverted 19 mΩ at 110 K; (b) non-inverted 30 mΩ at 295 K; (c) non-inverted 40 mΩ at 295; (d) After a catastrophic break is formed in the device used for the data in (c), no spin signal is detected; (e) SEM picture showing the catastrophic break between F_2 and Cu..... 109

Figure 6.5: (a) Basic assumptions of the one dimensional theoretical model. Nonmagnetic metal (N) is located in the region where $x < 0$, and F_2 is located in the region where $x > 0$. A tunneling barrier is formed at $x = 0$. The spin current is continuous across the barrier. (b) The spin accumulations across the N/F_2 interface. 111

Figure 6.6: The spatial dependence of $\boldsymbol{uecp1}\uparrow$ for different values of $\boldsymbol{\sigma ND}$ and δn_{10}. 118

Figure 6.7: The electro chemical potentials at $x = 0^-$ and $x = 0^+$ for the magnetization of F_2 oriented (a) up and (b) down. The inset of (a) shows a configuration which violates the boundary conditions. 121

Figure 6.8: The profiles of $\boldsymbol{uecp1}\uparrow$ (red) and $\boldsymbol{uecp1}\downarrow$ (blue) in F_2 for an inverted large spin signal. 124

Figure 6.9: The profiles of $\boldsymbol{uecp1}\uparrow$ (red) and $\boldsymbol{uecp1}\downarrow$ (blue) for a non-inverted large spin signal. 126

Figure 7.1: (a) SEM picture of a mesoscopic SHE/ISHE structure; (b) angle evaporation of the SHE/SHE structure through a shadow mask; (c) angle evaporation of a NLSV structure through a shadow mask; (d) SEM picture of a NLSV structure; (e) R_s versus B curve for the NLSV 133

Figure 7.2: (a) Measurement configuration for SHE; (b) distribution of spins (spin moments) throughout the structure; (c) R_s versus B curve with field applied along x axis; (d) R_s versus B curve with field applied along y axis 135

Figure 7.3: (a) Measurement configuration for the ISHE; (b) distribution of spins throughout the structure; (c) R_s versus B curve with field applied along x axis; (d) R_s versus B curve with field applied along y axis. 137

Figure 7.4: (a) Dimensions of the SHE/ISHE structure; (b) R_s versus B curve for a standard NLSV showing a spin signal of 1.8 mΩ; a cartoon of the structure is shown in the inset; (c) R_s versus B curve for a NLSV with a Pt wire under the Cu channel showing a spin signal of 1.1 mΩ; a cartoon of the structure is shown in the inset. 139

ABSTRACT

Spintronics, a frontier academic research area, is advancing rapidly in recent years. It has been chosen as one of the promising candidates for overcoming the obstacles in continuing the “Moore’s Law” of the electronics industry. Spintronics employs both spin and charge degrees of freedom of electrons to reduce energy consumption and increase the flexibility of IC design. To achieve this, it is extremely important to understand the generation, transport, and detection of the spin polarized current (spin current).

In this work we use a mesoscopic metallic spintronic structure-nonlocal spin valve (NLSV)-for fundamental studies of spintronics. A nonlocal spin valve consists of two ferromagnetic electrodes (a spin injector and a spin detector) bridged by a non-magnetic spin channel. A thin aluminum oxide barrier (~ 2 - 3 nm) has been shown to effectively enhance the spin injection and detection polarizations. We have studied spin injection and detection in these nanoscale structures. Several topics will be discussed in this work.

In Chapter 4 we explore spin transport in NLSVs with Ag channels. Substantial spin signals are observed. The temperature dependence of the spin signals indicates long spin diffusion lengths and low surface spin-flip rate in the mesoscopic Ag channels. Chapter 5 will focus on the asymmetric spin absorption across the low-resistance AlO_x barriers in NLSVs. This effect allows for a more simplified and efficient detection scheme for the spin accumulation. Then in Chapter 6 we report a large spin signal owing to a highly resistive break-junction. We have also developed a

model to describe the spin-charge coupling effect which enables the large spin signal. In the end, Spin Hall Effect (SHE) is investigated in Chapter 7. A mesoscopic Pt film is utilized to inject a spin accumulation into a mesoscopic Cu channel via the SHE. The spin accumulation in Cu can be detected by the nonlocal method. The reciprocal effect – the inverse Spin Hall Effect - (iSHE) is also observed in the same structure. A quantification method is described to estimate the spin Hall angle of Pt.

Chapter 1

INTRODUCTION

For humans, the information era has begun. One of the dominant rules of this revolution, Moore's law, predicts the doubling of transistor density every 18 months. However, as the size of electronic devices continues to shrink, Moore's law will be limited by the heating and quantum interference of electrons. [1] Scientists and researchers have made numerous efforts and proposed many alternatives for solving this issue. Spintronics has been selected as one of the most promising of these. Unlike traditional electronics that are based on a charge's degree of freedom, spintronics takes advantage of the "spin," one of the intrinsic degrees of freedom of electrons, to generate, transport, and store information. [2] This will not only open a novel field of magnetism research, it will also likely continue the miniaturization of electronic devices as predicted by Moore's law. Since it is at the core of spintronic research, the importance of researching spin transport can never be overemphasized. This thesis will mainly focus on the fundamental research of spin transport in a promising spintronic structure: nonlocal spin valves (NLSV).

This thesis is organized in the following manner. **Chapter 2**, first of all, will review the basic knowledge and recent progress of research in magnetism and spin transport. It will also discuss how the authors' research projects fit into the larger picture of spintronics. Basic concepts of the nonlocal spin valve will be discussed.

Chapter 3 will describe the experimental techniques that were utilized in this dissertation. Both the fabrication and measurement equipment will be discussed.

Chapter 4 through Chapter 7 will focus on the main research results of this dissertation that are related to nonlocal spin valves and spin Hall effects. **Chapter 4** will introduce our research regarding the absence of a high surface spin flip rate in mesoscopic silver channels. Note that the NLSV structures used in this research were fabricated with silver nonmagnetic channels. Large spin signals have been observed at room temperature as well as at 4.5 K, [3] indicating that silver garners long spin diffusion lengths. Furthermore, the temperature dependence of the spin signals in this research was monotonic, in contrast to the previously observed anomalous temperature dependence in copper channels. This difference can be explained by the silver channels' unusual morphological characteristics.

Following this discussion, we will then describe a project about asymmetric spin absorption in a nonlocal spin valve in **Chapter 5**. This chapter explores a new nonlocal spin detection method. In the conventional nonlocal detection method, the voltage is measured between the magnetic spin detector and the nonmagnetic channel. When using this new method, the nonlocal voltage is detected between the two ends of the extended magnetic spin detector. Clear nonlocal spin signals have been observed at room temperature and can be explained by asymmetric spin absorption across the low-resistance oxide interface. This method simplifies the nonlocal detection geometry and provides additional flexibility in designed spintronic structures.

Chapter 6 focuses on NLSV structures with break-junction interfaces between the magnetic spin detector and the nonmagnetic channel. Spin signals with both non-inverted and inverted signs have been detected with magnitudes that are substantially higher than regular nonlocal spin signals. The break junctions are formed by electrostatic discharge. A theory that was developed by our collaborator Siu-Tat Chui

[4, 5] will be used to explain the large magnitudes and the signs of the spin signals in break-junction structures. [6]

Chapter 7 will describe our work regarding efficient room temperature spin Hall injection across an oxide barrier. The spin Hall effect (SHE) is a rapidly developing area in magnetism research because of how it allows the conversion from charge current to spin current without the use of magnetic materials. This novel phenomenon occurs in heavy nonmagnetic metals such as platinum and will enrich the capabilities of spintronics. The inverse spin Hall effect (ISHE), on the other hand, converts a pure spin current into a charge current in the heavy metals; it is considered to be the reciprocal effect of SHE. This work will explain our unique SHE/ISHE structure, in which both the SHE and ISHE can be measured. This structure is closely related to the NLSV structures; it will be described in the upcoming chapters.

Chapter 7 will also detail how we have observed clear spin Hall signals at room temperature, whose magnitudes are higher than those that have been reported in previous studies. We have performed a quantitative analysis of the data in order to extract its relevant parameters, such as the spin Hall angle of platinum. [7]

REFERENCES

[1] http://en.wikipedia.org/wiki/Moore%27s_law.

[2] G. A. Prinz, Science, **282**, 1660 (1998).

[3] S. Chen, H. Zou, C. Qin, and Y. Ji, Applied Physics Express, **7**, 113001 (2014).

[4] S. T. Chui and Z. F. Lin, Physical Review B, 77 (9), 094432 (2008).

[5] S. T. Chui, "Multiple magnetic tunnel junctions", U.S. Patent 5757056, May 26, 1998.

[6] S. Chen, H. Zou, S. T. Chui, and Y. Ji, Jounral of Applied Physics, **114**, 223906 (2013).

[7] S. Chen, C. Qin, and Y. Ji, *et al*., Applied Physics Letters, **105**, 082402 (2014).

Chapter 2

BACKGROUND OF MAGNETISM AND INTRODUCTION TO SPINTRONICS

Stimulated by the discovery of giant magnetoresistance (GMR) in 1988, research related to magnetism has been prosperous for several decades. [1, 2] The momentum of this research was sustained by the emergence of spintronics at the end of 20th century. [3, 4] In this chapter, we will introduce some crucial concepts in magnetics and spintronics and show how this thesis fits into the larger picture of this field.

2.1 History of the Discovery and Application of Magnetism

The investigation of magnetism and its associated applications has a long history. In the thousands of years before the electromagnetic revolution, the research and application of magnetism mainly focused on military navigation. [5] In 1820, Hans Christian Ørsted demonstrated that a metallic wire carrying some electrical current would produce a circumferential field that could deflect a compass needle. [6] During the same time period, Andre-Marie Ampere and Dominique Francois Arago showed that a current-carrying winding coil was equivalent to a magnet. [7] Michael Faraday discovered electromagnetic induction and demonstrated an initial principle of the electric motor. [8] He also discovered a connection between magnetism and light; this was named the magneto-optic Faraday effect in 1845. [9]

All of this experimental work inspired James Clerk Maxwell to formulate a unified theory of electricity, magnetism, and light in 1864, which is summarized in the following four equations: [10]

$$\nabla \cdot B = 0,$$
$$\nabla \cdot E = \frac{\rho}{\varepsilon_0},$$
$$\nabla \times B = \mu_0 j + \mu_0 \varepsilon_0 \frac{\partial E}{\partial t},$$
$$\nabla \times E = -\frac{\partial B}{\partial t}.$$

These equations relate the electric and magnetic fields *E* and *B* at a point in free space to the distributions of electric charge and current densities ρ and j in surrounding space. This was a successful theoretical attempt to discover the relationship between *E* and *B*.

Maxwell's equations solve the behavior of the electromagnetic field in the media of continuous space or regular materials, but the origins of ferromagnetism were still mysterious until the emergence of quantum mechanics. Discovered by George Uhlenbeck and Samuel Goudsmit in 1925, the intrinsic spin of the electron was quantized for only two possible orientations in a magnetic field, "up" and "down." [11] Later on, spin was known as the source of the electron's intrinsic magnetic moment, which is the Bohr magneton $\mu_B = 9.274 \times 10^{-24}$ Am^2. [12] Gradually, scientists realized that magnetic properties arise mainly from the magnetic moments of the electrons in atoms. The interactions that are responsible for ferromagnetism were shown by Werner Heisenberg in the Hamiltonian $H = -2J\, S_i \cdot S_j$, wherein J is the exchange constant. The magnitude and polarity of J will determine the magnetic property of a specific material. It has been proven that, when the exchange interaction J is positive, a solid will exhibit ferromagnetism. When J is negative, there will be a

tendency for the spins at sites i and j to align antiparallel rather than parallel, leading to antiferromagnetism. It should be noted that magnetic properties also depend on the topology of the crystal lattice. [5]

Stimulated by Heisenberg's theory, the details of ferromagnetism were progressively revealed by both experimentalists and theorists. As the first prerequisite to producing micro-magnetism, ferromagnetism requires unpaired electrons on the outmost atomic orbitals. Due to the Pauli Exclusion Principle, electrons with identical spin orientations are not allowed to exist on the same angular momentum orbital. [12] As a result, electrons fill up from the inner shell to the outmost one by forming a pair of spins ("up" and "down") on each angular momentum orbit. If there are an odd number of electrons on the outmost orbital, the atom achieves a net gain in magnetic moments.

The second prerequisite of ferromagnetism is that electrons tend to expel each other due to Coulomb interaction and to minimize the total energy produced from this. Consequently, a balance is achieved in the band structure between Coulomb interaction and the minimum energy requirement. [12] The third prerequisite, as described by Heisenberg's theory, is that the exchange interaction between different spins also plays an important role in forming different types of magnetism. In addition, the hybridization of orbits in atoms as well as band structures in solids also needs to be considered in order to understand magnetic properties. For example, the exchange interaction in transition metals will try to align the spins according to the polarity of J. However, inter-atomic hybridization and band formation tend to surpass the spin polarization because of the principle of the minimization of total energy. A result of the balance between the exchange interaction and the hybridization is ferromagnetism.

If the hybridization is too weak to reduce the spin polarization, the solid becomes ferromagnetic. [13] Summarizing all of these conditions for the various elements, only iron (Fe), cobalt (Co), nickel (Ni), and their certain alloys will show ferromagnetism, since they each have a partially filled 3d shell and 4f orbits that reduce atomic hybridization. In other words, ferromagnetic structures are not that common because of the complexity of atomic-level interaction and interference from the band structure. [13]

2.2 Magnetism: Hysteresis Loop

Quantum mechanics can help to explain the origins of ferromagnetism. In reality, however, we still need to understand large-scale magnetism in order to explore the magnetic properties of materials at a macroscopic level. It is generally known that there are three basic magnetic vectors defined for this purpose: the magnetic induction intensity B, the magnetization M, and the magnetic field H. The sources of the B-field are the electric current or magnetic moments carried by electrons as they move around atoms, making B a real physics quantity. When characterizing magnetic properties in media, the H-field becomes a convenient auxiliary field. In free space, the relationship between the B-field and the H-field is trivial and can be defined by the equation $B = \mu_0 H$. When there is a medium in the space, however, the relation will be intimidating: $\nabla \times B = \mu_0(j_c + j_m)$, wherein j_c is the conduction current in electrical wires and j_m is the Amperian magnetization current associated with the magnetized medium. Due to a lack of methods for precisely measuring the Amperian magnetization current, it is convenient to separate different sources of magnetic field by defining $H = B/\mu_0 - M$, $\nabla \times H = j_c$, and $\nabla \cdot H = -\nabla \cdot M$. In fact, the H-field is

more commonly used in experimental magnetism research, since it is directly related to the applied external field and makes calculating the Ørsted field easier. [10]

It is indispensable to talk about hysteresis loops when it comes to magnetism and magnetic material research, since the hysteresis loop illustrates the irreversible nonlinear response of magnetization to the external field. When there is an imposed external magnetic field H on a ferromagnetic material, the practical response of the magnetization M should be characterized by the hysteresis loop. **Figure 2.1** shows an example hysteresis loop as M vs. H. The arrows indicate the direction of the loop's sweep. The dashed line shows the initial magnetization process when applied field H increases. H will be decreased and switched to the opposite direction after the magnetization reaches saturation, known as M_S. After this, M will reach the remnant state at the zero field, $M = M_r$. When H reaches the coercive field, H_c, M changes sign. M_r and H_c are known as the remanence and the coercivity of this material. [13] It is important to remember that this process is irreversible, indicating a mnemonic application of magnetic materials holding their magnetization orientations until the applied external field reaches H_c in the opposite direction. Hard magnets (ferromagnets with large coercivity) possess broad, squared loops with large coercivity H_c. Once they are magnetized by applying field $H \geq H_c$, they will remain in a magnetized state even when the field is removed. They are suitable for permanent magnet applications (in electric generators, electric motors, etc.) and magnetic recording media. On the contrary, soft magnetic materials (ferromagnets with small coercivity H_c) have very narrow and smooth loops and readily change their magnetization after a small reversal field is applied. They are suitable for applications in the recording heads of hard drive disks.

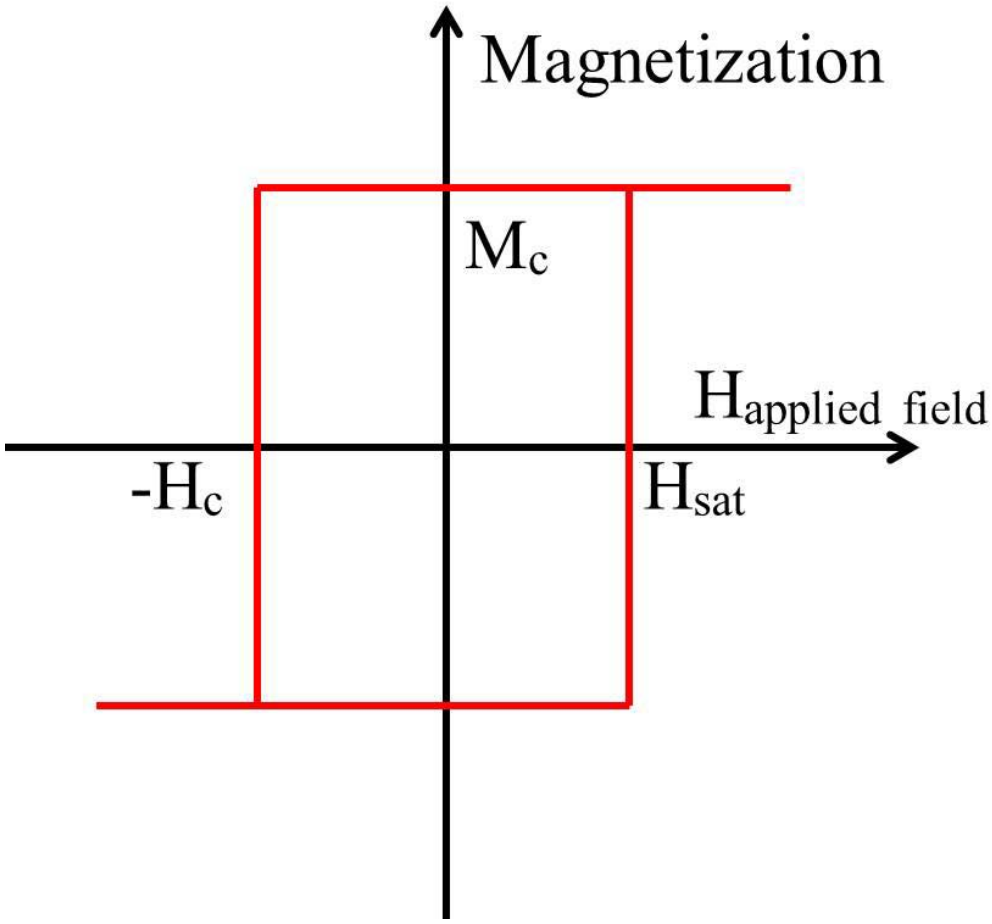

Figure 2.1: A Hysteresis Loop

2.3 Magnetism: Spintronics

To accomplish the goal of applying both charge and spin degrees of freedom to the next revolution in information technology, it is crucial to understand the generation, transport, and detection of spins in various materials and artificial structures. Here, we will mainly focus on several crucial concepts such as giant magnetoresistance (GMR), tunnel magnetoresistance (TMR), spin polarization, and spin diffusion length.

2.3.1 GMR: The Beginning of Spintronics

First suggested by Mott in 1936, [14] the influence of spin on the mobility of the electrons in ferromagnetic metals has been experimentally demonstrated and theoretically described in several literatures. [15-18] The spin dependence of conduction was formerly understood as originating from the band structure of a ferromagnetic metal. [14] The splitting between the energies of the "spin majority" and "spin minority" enables the electrons at the Fermi level of ferromagnetic materials to have different density of states for opposite spin directions ("up" and "down") and to therefore exhibit different conduction properties. Fert confirmed that the resistivities of the two channels can be quite different based upon the two-current model for conduction in ferromagnetic metals. [15-17] His model is based on spin-mixing, i.e. the coupling between spin "up" and spin "down" currents. Spin mixing comes from the exchange of momentum by spin-flip scattering between the two spin channels, which mainly occurs because of how electron-magnon scattering partially evens the spin "up" and spin "down" currents. In most cases, the interpretation of the spintronic phenomena is based on a simplified version that neglects spin mixing and assumes that no interference occurs between the two independent spin-conducting channels. [19]

It was anisotropic mangetoresistance (AMR) that first drew attention to the application of magnets during the electric age; this is because AMR involves controlling charge current by changing the external field, although the ratio that was used was very small (~3%). [13] The giant magnetoresistance (GMR) is substantially larger than the AMR effect, and its magnetoresistance (MR) ratio is >10%. [20, 21] The GMR was a groundbreaking discovery for magnetic field sensor technology as well as for the understanding of spin transport. Its application in the magnetic recording read heads of hard drive disks contributed greatly to the rise of information

storage and to the extension of hard drive disk technology within consumer electronics. [5, 13] Furthermore, the development of GMR expedited the research of many other spintronic phenomena, such as spin accumulation and injection, spin transfer torque, and spin Hall effect; these are all related to the control and manipulation of spin currents.

The principles of GMR may be best explained by describing its basic structure- three layers of metals, one non-magnetic metallic layer sandwiched between two ferromagnetic layers [**Fig. 2.2]**. According to the two-current model, the resistivity values for two spin channels are different. The resistance of the tri-layer model depends on the layers' relative magnetization orientations. Generally, the conductive electrons will encounter lower resistance if their spin orientation is parallel to the magnetization of the ferromagnetic channel layer. On the contrary, the electrical resistance will be higher if the conducting electrons possess anti-parallel spin orientations to the magnetization of the ferromagnetic channel layer. In a sandwiched tri-layer system, therefore, the conducting electrons will be "filtered" by the layers with an anti-parallel magnetization. If the magnetizations of both magnetic layers are parallel, only the electrons that are conducting the opposite spin orientation will be "filtered," allowing the other electrons to pass. A low electrical resistance is produced. If the ferromagnetic layers are anti-parallel, the conducting electrons with either spin orientation will be "filtered" so that the total resistance is high. The different resistance values for parallel and anti-parallel states will be converted into proper digital voltage signal levels and captured by next-level detectors. [19]

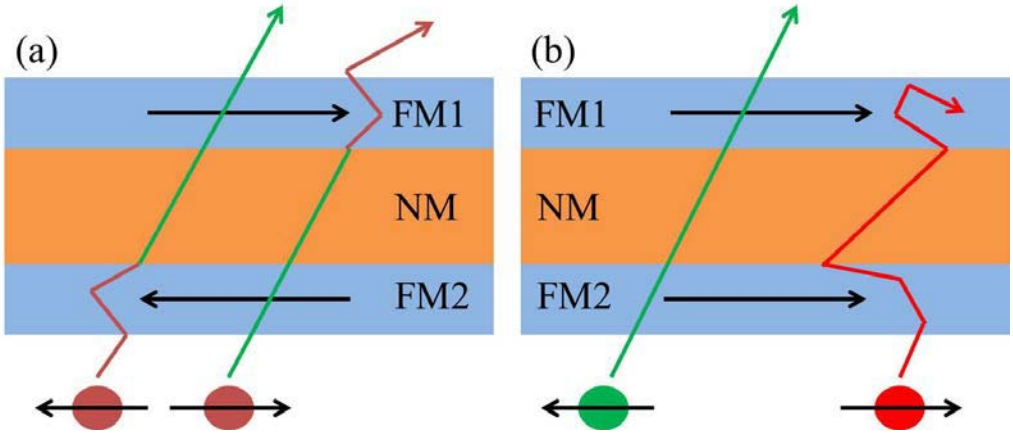

Figure 2.2: A schematic of mechanism of GMR: In the anti-parallel magnetic configuration (left), electrons with both spins will experience higher "spin resistance" in each magnetic layer and the external circuit will show a high resistance. In the parallel magnetic configuration (right), at least electrons with one of the spins will pass through both magnetic layers easily and the external circuit will show a low resistance.

The relative orientations of the two ferromagnetic layers can be felt by electrons only when the layers' thickness is smaller than the electrons' mean free path (MFP), which can range from a few to hundreds of nanometers. This is one of the reasons why spintronic research and the hard drive disk industry rely on thin film processing and other relevant nanotechnology. We will introduce many of those techniques in Chapter 3.

There are basically two kinds of GMR structures that are used for research and applications. They are classified by the direction of current in multilayer structures. The above structure is called a current-perpendicular-to-plane (CPP) structure. The other option is called a current-in-plane (CIP) structure. [**Fig. 2.3]** In a CIP structure, the current flows into the plane of the multilayered structure and experiences scattering from all of the layers simultaneously. However, the electrical resistance of

the device still depends on the relative orientations of the magnetic layers. When the magnetic layers are aligned in parallel, the electrons with the same orientation will be scattered by both layers; the opposite spin orientation electrons will be scattered less. Therefore, this system demonstrates low resistance. When the two magnetic layers are aligned anti-parallel, on the other hand, electrons with both sub-band spins will experience higher scattering rates, giving the system a high resistance. This configuration presents a huge difficulty for theoretical research because it mixes the influence on the spin channels from both magnetic layers. In CPP structures, on the other hand, the current passes through the tri-layer-structure perpendicularly, experiencing the scattering layer by layer. This is easier to study theoretically because it allows researchers to build transmission wave functions with desired and clear boundary conditions for specific interfaces. Also, the CPP structure makes it easier to fabricate complex and large-scale structures. [22] Furthermore, the CPP structure shows a more significant spin accumulation effect around magnetic-nonmagnetic interfaces than the CIP structure. [23] This effect actually dominates the propagation of spin-polarized currents through a series of multilayer devices. It allows a spin-polarized current to travel a long spin diffusion length, which can be calculated as:

$$L_{sf} = \sqrt{D\tau_{sf}} = \sqrt{\frac{1}{3}\lambda_t v_F \tau_{sf}} = \sqrt{\frac{1}{3}\lambda_t \lambda_{sf}}$$

where D is the diffusion constant, τ_{sf} is the mean time between spin-flipping events, λ_t is the transport mean free path, v_F is the Fermi velocity, and λ_{sf} is the spin-flip length. [24]

The spin diffusion length can be understood as the distance between spin-flip events in the direction of electron flow. It is another critical parameter in the spintronic

research community because it spatially describes how long electrons will transport within certain materials without losing their carried spin information.

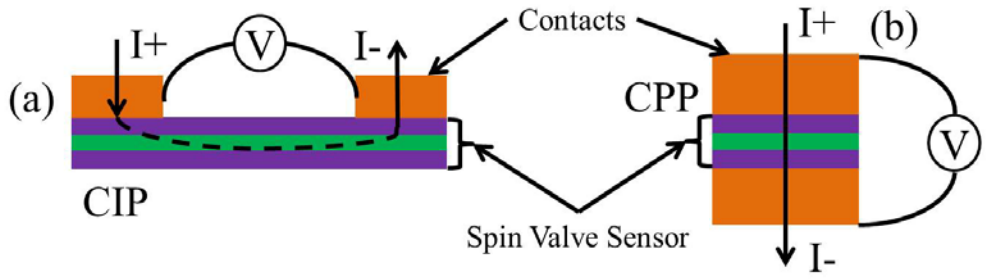

Figure 2.3: Diagrams for CIP (left) CPP (right) configurations.

2.3.2 TMR: A Breakthrough for Spintronics

Another milestone in spintronics is the research on tunneling magnetoresistance (TMR) in the magnetic tunnel junction (MTJ). The TMR ratio of the MTJ was initially >20% [25, 26]; later, very large TMR values of >200% were found in MgO-based tunnel junctions. [27, 28] The structure of MTJs is a very thin insulating oxide layer sandwiched between two ferromagnetic layers. There is a significant difference between their resistance values for the parallel and antiparallel magnetic configurations of the ferromagnetic electrodes.

The interest in this subject comes from, first, the fact that the vertical direction of the current in CPP-structure MTJs aids theoretical analysis; secondly, the lateral size of metallic spin valves can be reduced to the nanoscale by lithographic techniques. The MTJs are the basis of magnetic recording read heads in hard drive disks and the emerging technology of magnetoresistive random-access memory (MRAM). Some early observations of TMR effects at low temperatures were reported

by Jullière in 1975. [29] The important breakthroughs in this field were made in 2004 by Parkin *et al*. [27] and Yuasa *et al*., [28] who found that up to 200% TMR ratios at room temperature could be obtained from MTJs with MgO tunneling layers of a very high structural quality. Because the single crystal barrier of MgO screens the symmetry of the wave functions of the tunneling electrons, the TMR depends on the spin polarization of the ferromagnetic electrodes with the designated symmetry. [30-32] It should also be noted that the fact that a high TMR ratio that can be obtained from a single crystal tunneling barrier is a very good illustration of spin polarization, which can be defined as the following:

$$P = \frac{N_{\uparrow}(E_F) - N_{\downarrow}(E_F)}{N_{\uparrow}(E_F) + N_{\downarrow}(E_F)}$$

where $N_{\uparrow}(E_F)$ ($N_{\downarrow}(E_F)$) stands for the density of states (DOS) for spin-up and spin-down electrons at the Fermi level. For normal nonmagnetic metals, the symmetrical band structure at the Fermi level for spin-up and spin-down electrons results in no spin polarization, or $P = 0$. However, for ferromagnetic materials, the band structure at the Fermi level is asymmetrical for spin-up and spin-down sub-bands, which is one of the reasons why the materials are ferromagnetic in the first place. The splitting of two spin sub-bands unbalances the DOS for spin-up and spin-down, giving us $0 < P < 1$. For a half-metallic ferromagnet, there is only one spin state that exists at the Fermi level, so $P = 1$. [28] Because of this, spin polarization describes to what extent the conducting electrons at the Fermi level spin polarized or around junctions in certain materials. This is a vital concept in spintronics because researchers prefer to use higher spin polarization materials for spintronic devices in order to create giant spin accumulation and spin current. For example, Fert's group has obtained a very high spin polarization

of 95% and a TMR ratio of 1800% with $La_{2/3}Sr_{1/3}MnO_3$ electrodes. [33] The TMR can actually be written in the form of spin polarization as following: [22]

$$TMR = \frac{2P_{top}P_{bottom}}{1 - P_{top}P_{bottom}}$$

where P_{top} and P_{bottom} are the spin polarizations at the FM/NM interfaces. It can be seen that the higher the spin polarization, the higher the potential TMR.

The next section will introduce spin accumulation and nonlocal spin valves (NLSV).

2.4 Introduction for Nonlocal Spin Valve

Nonlocal spin valves (NLSVs) are also known as lateral spin valves; they and related structures are the main focus of this dissertation. Compared to other CPP spintronic devices, nonlocal spin valves have unique advantages because of their design flexibility for multi-terminal devices. The ability to easily generate a pure spin current in NLSVs is attractive. It is also possible to manipulate spins during transport in the nonmagnetic channels of NLSV structures.

Since spin polarization, spin diffusion length, and spin accumulation are crucial for the study of spintronics, it is extremely important to examine them accurately and efficiently. To accomplish this, we first need to generate a spin accumulation and perform a spin injection from one material to another. There must, therefore, be a reliable mechanism to evaluate this spin injection and the other parameters. There are numerous methods to achieve this, such as spin pumping, spin Seebeck effect, spin Hall effect, and electrical injection through certain magneto-electric devices (such as NLSVs). This thesis will focus on the latter two items.

Before explaining the concept and structure of the NLSV, the concept of spin accumulation should be introduced. Spin accumulation occurs when an electron flux crosses the interface between a ferromagnetic and a nonmagnetic material. Typically, the charge current will be injected from magnetic electrodes into a nonmagnetic region, though in MTJ it needs to overcome the tunneling barrier first. In the magnetic material, the current with major spin polarity will dominate over the polarity far from the interface. Let us assume that this current is spin "up." On the other side (i.e., on the nonmagnetic material), the current is equally distributed in the two spin channels. There is then an accumulation of spin-up electrons and a suppression of spin-down electrons around the interface; in other words, there is a split between the Fermi energies (chemical potentials) of the spin-up and spin-down electrons. Then, an accumulation-induced spin current will diffuse from the interface to the distance of the spin diffusion length (SDL). Spin flips are also experienced by these electrons during this process, with a steady energy level reached when the number of incoming and outgoing fluxes of spin-up and spin-down electrons cancel each other out. Therefore, there is a broad zone of spin accumulation that extends to the distance of the SDL. During this process, the current will be progressively depolarized by the spin flips or other spin decoherence efforts. [34-37]

Now, we will introduce the experimental aspects for NLSV. Normally, a nonlocal spin valve consists of two ferromagnetic (FM) electrodes that are connected by a nonmagnetic (NM) channel. **[Fig. 2.4]** The equation for calculating spin resistance signal ΔR_S is also shown in **Figure 2.4**. The left FM electrode is used as a spin injector (F_1), while the other FM electrode is used as a spin detector (F_2). The NM channel can include metals, semiconductors, insulators, or other novel materials

(organic materials or graphene). During measurement, an electrical current will be injected through F_1 to the left end of the NM channel, and the voltage will be detected through F_2 to the right end of the NM channel. This is called a nonlocal measurement technique (i.e., when the current injection loop and the voltage detection loop are separated), which eliminates spurious effects such as anisotropic magnetoresistance (AMR) from local measurements. An external magnetic field H will be applied parallel to the easy axis of F_1 or F_2, sweeping back and forth from positive to negative polarity. In the NM channel and at the interface between the FM and NM materials, a spin accumulation is generated as a result of the electrical spin injection. The spin accumulation, expressed as $\delta\mu = \mu_{\uparrow} - \mu_{\downarrow}$, is actually a splitting of electro-chemical potentials at the Fermi level for spin-up and spin-down electrons. The spin accumulation drives spin currents in both directions along the nonmagnetic channel. The magnitude of spin accumulation decays exponentially, and the characteristic decay length is the spin diffusion length λ_{sf}. Apparently, spin current on the right side of F_1 is a result of self-diffusion; therefore, it is a pure spin current without a net charge current. Depending on the relative spin orientations between the detector and the injector, a voltage change can be measured across the interface between F_2 and N. When F_2 is aligned parallel to the spin accumulation around the interface of F_1/N, its Fermi level is aligned with the upper Fermi level in N, thus exhibiting a high voltage. When F_2 is aligned antiparallel to the spin accumulation in N, a low electrical potential can be detected.

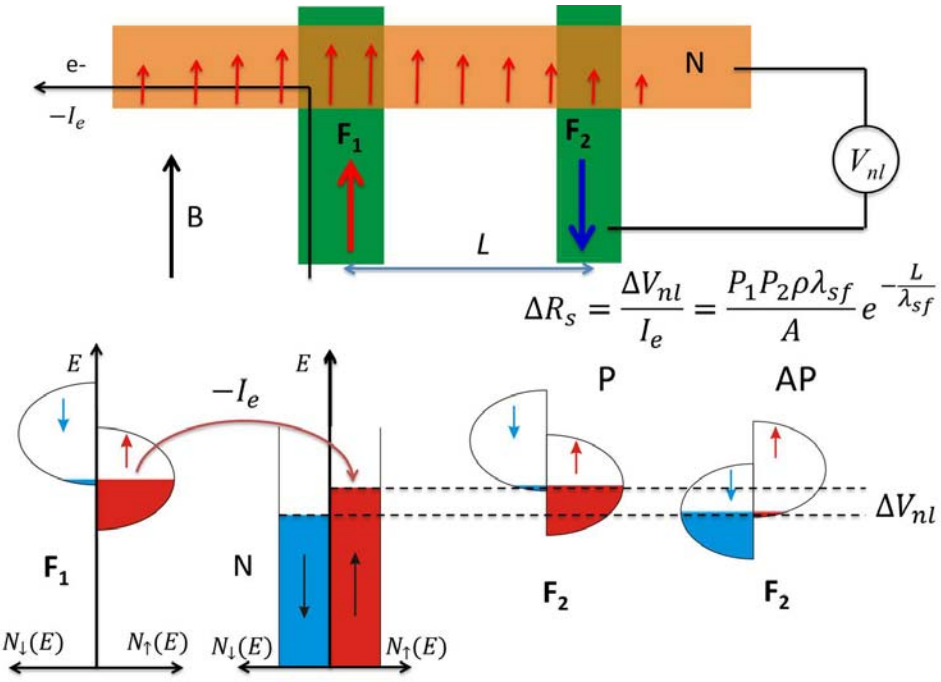

Figure 2.4: Schematics for nonlocal spin valve with band structures of F_1, F_2 and N. The self-diffuse spin current will travel a distance called spin diffusion length from F_1 to F_2 and detected as a voltage contrast ΔV_{nl} according to the spin orientation of F_2 manipulated by external magnetic field.

We would also like to review some theoretical calculations about spin transport in NLSVs. According to electron transport theory, the current density j_σ in the spin channel σ is written with the drift term and the diffusion term characterized by non-equilibrium electron density δn_σ:

$$j_\sigma = \sigma_\sigma E - eD_\sigma \nabla \delta n_\sigma, \qquad (2.1)$$

where σ_σ, D_σ and E are the conductivity, the diffusion constant of each spin channel σ, and the electrical field, respectively. If we apply $E = -\nabla \phi_e$, the Einstein relation $\sigma_\sigma = e^2 N_\sigma D_\sigma$ and $\delta n_\sigma = N_\sigma \delta \varepsilon_\sigma$, it is going to have:

$$j_\sigma = -\frac{\sigma_\sigma}{e}(e\nabla\phi_e + \nabla \delta n \varepsilon_\sigma) = -\frac{\sigma_\sigma}{e}\nabla \mu_\sigma, \qquad (2.2)$$

where ϕ_e and $\delta\varepsilon_\sigma$ are the electrical potential and the shift in the electrical chemical potential of electrons from its equilibrium value (typically the Fermi level). The figure μ_σ represents the electro-chemical potential.

When we apply the continuity equations to the charge and spin that is current in the steady state, we obtain the following equations:

$$\nabla \cdot (j_\uparrow + j_\downarrow) = 0, \qquad (2.3)$$

$$\nabla \cdot (j_\uparrow - j_\downarrow) = -e\frac{\delta n_\uparrow}{\tau_{\uparrow\downarrow}} + e\frac{\delta n_\downarrow}{\tau_{\downarrow\uparrow}}, \qquad (2.4)$$

where the $\tau_{\sigma\sigma'}$ is the spin scattering time from one spin channel σ to another spin channel σ'. By combining these with the above expressions for j_σ, the equilibrium relation $\frac{N_\uparrow}{\tau_{\uparrow\downarrow}} = \frac{N_\downarrow}{\tau_{\downarrow\uparrow}}$, and the definition $\tau_{sf}^{-1} = (\tau_{\uparrow\downarrow}^{-1} + \tau_{\downarrow\uparrow}^{-1})/2$, $D^{-1} = (N_\uparrow D_\downarrow^{-1} + N_\downarrow D_\uparrow^{-1})(N_\uparrow + N_\downarrow)$, we obtain:

$$\nabla^2 \cdot (\sigma_\uparrow \mu_\uparrow + \sigma_\downarrow \mu_\downarrow) = 0, \qquad (2.5)$$

$$\nabla^2 \cdot (\mu_\uparrow - \mu_\downarrow) = \lambda_{sf}^{-2}(\mu_\uparrow - \mu_\downarrow), \qquad (2.6)$$

where $\lambda_{sf} = \sqrt{D\tau_{sf}}$, which is the spin diffusion length. The spin current can be expressed as:

$$j_s = -\frac{\sigma_s}{2e}\nabla\delta\mu, \qquad (2.7)$$

where σ_s stands for the conductivity of a certain spin state. The relationship between spin current density and electric-chemical potential has here been deduced.

This idea of electrical spin injection and detection as a method to create non-equilibrium spin accumulation in nonmagnetic metals was first proposed in 1976 by Aronov and Pikus theoretically. [38] Van Son *et al.* also obtained basic equations for change in electro-chemical potentials that describe the charge and spin transport across an interface between two different materials. [39] Experimentally, the first successful

attempt was performed by Mark Johnson and R. H. Silsbee in 1985 in a “bulk” single-crystal aluminum bar. [40, **Fig. 2.5 (a)**]

Mark Johnson’s experiment demonstrated the concept of a coupling between charge and spin at an interface between a ferromagnetic and a paramagnetic metal. Johnson’s researchers claimed that a nonequilibirum magnetization in a paramagnet can be detected as an electric voltage. They also achieved Hanle effect measurement results. [40] Although they detected the spin-dependent voltage change, the macroscopic size of the sample (aluminum sliced into a bar 50 μm by 100 μm by 1.5 cm) prevented the further application of this method within micro- or nano-electronics.

Later in 2001, Jedema and other researchers demonstrated nonlocal spin injection and detection in nanoscale Py/Cu/Py lateral structures at room temperature [41, **Fig. 2.5 (b)**]. Note that Py is a magnetic alloy known as permalloy with the composition of $Ni_{80}Fe_{20}$. By studying the dependence of nonlocal spin signals upon the distances between the spin injector and detector (from 250 nm to 2 μm), the spin diffusion length of Cu can be estimated to be 350 nm at room temperature and 1000 nm at 4.2 K. In 2002, these researchers performed Hanle effect measurements in nanoscale Al stripes, clearly demonstrating that the nonlocal spin resistance signal is caused by spin injection and transport. [42] In addition, the injection and detection barriers are oxide tunnel junctions instead of transparent ohmic junctions.

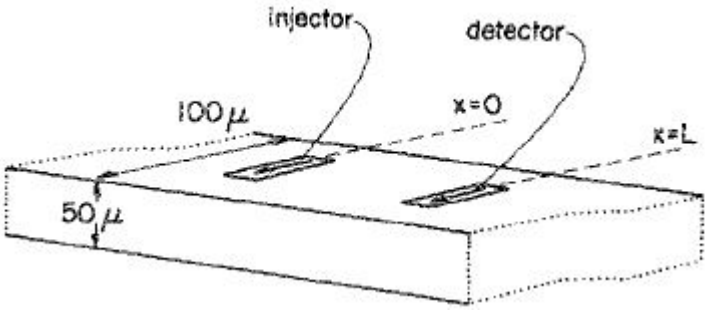

Figure 2.5: (a) A schematic of Mark Johnson's experiment for spin injection. A bar of pure bulk metal, about 50 μm thick and 100 μm wide, is coated with an insulating film. The distance between two electrodes is L. Reprinted with permission from [40].

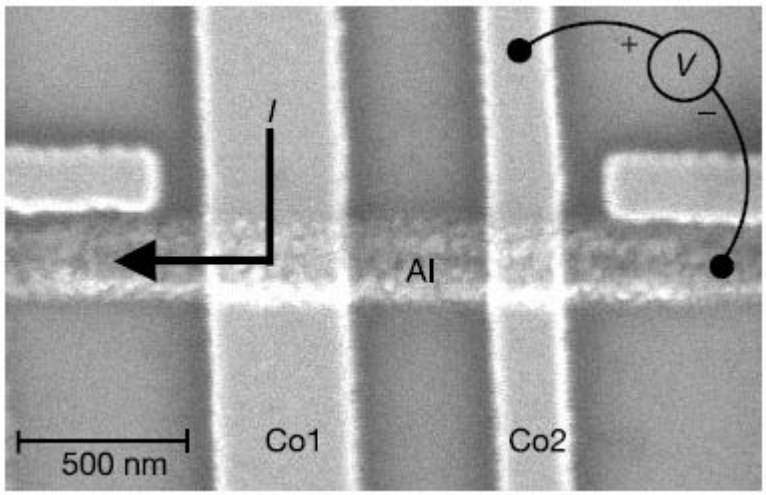

Figure 2.5: (b) Scanning electron microscope image of Jedema's device with a cobalt (Co) electrode spacing of $L = 650\ nm$. Current is sent from Co1 into the Al strip. The voltage is measured between Co2 and the right side of the Al strip. Reprinted with permission from [42].

Jedema *et al.*'s results stimulated interest in the study of spin injection, transport, and detection using nonlocal structures. Objective-specific aspects of this will be reviewed in Sections 2.5 and 2.6.

2.5 Motivation for Further Studies Related to NLSVs

The understanding of spin transport mechanisms in nonmagnetic materials is essential and can help to enhance the spin signals in NLSVs. In modern nanotechnology development, when one or more dimensions of a structure become comparable to the characteristic length scale of a physical process, even classical boundary or surface effects can give rise to dramatically different behavior than that expected from the bulk material. An important question to be addressed in spintronics is how the size of a spin conductor or its surface conditions affects the transport of spin currents. In particular, to what extent does this confinement affect the spin diffusion length and spin relaxation time? Due to the relatively longer spin diffusion length than mean free path, confinement effects can sometimes be more pronounced for spin transport in metals. As summarized below, various groups have conducted studies to address this question.

Otani's group, for example, demonstrated a large spin accumulation in Py/Ag/Py and Py/Cu/Py spin valves [43, 44]. Their results indicate that spin relaxation lengths are about 700 nm for Ag and 400 nm for Cu at room temperature. They also found that the spin transport in Cu and Ag spin valves is affected in contact junction size, temperature, and spin absorption by an extra FM electrode inserted between the injector and the detector. [45, 46] They also clearly showed that the spin polarization in nonmagnetic metals can be manipulated by changing the spin-polarized angle of the injected current. [47] Additionally, they obtained giant spin resistance signals (up to 100 mΩ at low temperatures) from MgO-based lateral spin valves with two spin injectors. [48]

This dissertation investigates a new spin-charge coupling mechanism across a nanometer-sized break junction that amplifies spin accumulation. The spin signals

from the break-junction NLSVs are large, and the signs can be either positive or negative. [49] The signals are detectable at various temperatures. The origin of the large magnitudes and sign reversals of the signals can be explained by a spin-charge coupling theory that was developed by our collaborator S. T. Chui. [50, 51] The details of this theory will be presented in Chapter 6.

The diffusion properties of spin current and the bias dependence of the spin transport have been studied in nonlocal spin valves by many different groups, including Valenzuela *et al.*, [52] Casanova *et al.*, [53] and Ji *et al.*, [54, 55]; this contributed to the research on the manipulation of spin polarization. G. Mihajlovic *et al.* [56] researched spin flip probability in Ag channels with NLSVs, presenting a model that was based on the Elliott-Yafet (EY) mechanism of spin relaxation in order to quantify spin flip probabilities for phonon, impurity, and surface scattering in mesoscopic metal wires. Au-based nonlocal spin valves were studied by Ji *et al*. [57] in regards to spin injection, diffusion, and detection. These researchers found that the spin relaxation length is about 60 *nm* at 10 K. Zou *et al*., [58] furthermore, discovered the non-monotonic dependence of spin signals on temperature in Py/Cu/Py based NLSVs, which they attributed to magnetic impurities near the surface of nonmagnetic channels caused by shadow evaporation methods.

This dissertation demonstrates large spin signals in Py-Ag based NLSV structures. In addition (and in contrast to the observation described above), we observed a monotonic decrease of spin signal with increasing temperature. This can be attributed to the morphology of the Ag channel, which was formed in Volmer-Weber growth mode during the deposition. [59] The details of this work will be presented in Chapter 4. We also demonstrate a novel nonlocal spin accumulation detection method

that relies on asymmetric spin absorption at the detector-side interface. This will be discussed in Chapter 5.

It is advantageous to utilize NLSVs for research on other spin transport phenomena, such as the spin Hall effect. Employing multiple types of measurements based on different techniques makes it convenient to separate various spurious effects and perform research on one topic from multiple angles.

Other than the research on spin injection, spin accumulation, and spin current transport described above, researchers have used lateral spin valves to study spin dynamics, spin transfer torque, the spin Seebeck effect, and the spin Hall effect. Spin dynamics needs an external microwave source to trigger spin precession, which is indispensable for spin pumping realization. [60, 61] The spin transfer torque switching mechanism (which is actually an inverse physical process to spin pumping) and its relationship to spin torque can be explained with a model proposed by Slonczewski [62] and Berger [63]. In this model, the torque exerted on the magnetization is proportional to the injected spin current. This clearly demonstrates that the spin current could be essential in realizing magnetization switching due to spin injection. [64, 65] Also, the spin Seebeck effect uses spin currents driven by thermal derivatives (temperature gradients) to realize spin injection; this is a promising, but still controversial application of spintronics [66, 67].

The next section and Chapter 7 will focus on the spin Hall effect and related research.

2.6 The Spin Hall Effect

2.6.1 Introduction to the Spin Hall Effect

The spin Hall effect (SHE) was predicted by Dayakonov and Perel about 40 years ago. [68, **Fig. 2.6**] They proposed that an unpolarized electrical current would lead to a transverse spin polarized current in a strong relativistic spin–orbit system. As they pointed out, SHE is induced by spin-orbit coupling via Mott scattering when impurities induce a spatial separation of electrons with opposite spins. In SHE, the polarization axes of spins, the direction of the transverse spin current, and the direction of the longitudinal electrical current are perpendicular to each other, exhibiting an orthogonality similar to a normal Hall effect.

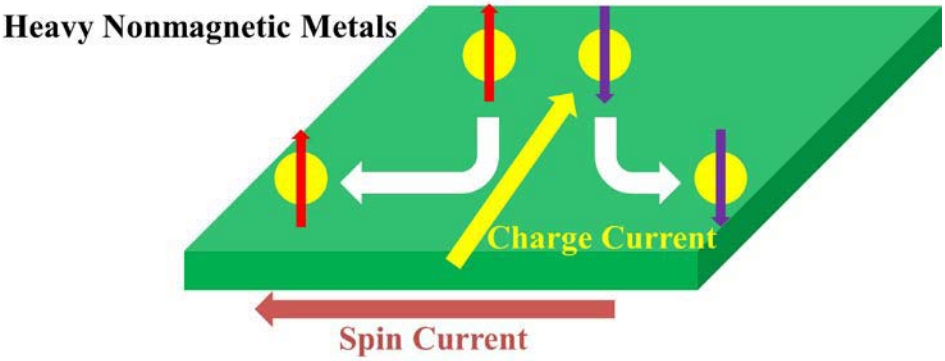

Figure 2.6: A simple sketch for spin Hall effect (SHE). In some nonmagnetic normal materials, as a charge current passes through, a spin current will be generated in the transverse direction due to strong spin-orbit coupling and build up spin accumulation along the two edges. On the contrary, a spin current will induce electrical voltage detectable in the transverse direction, which is called inverse spin Hall effect (iSHE).

Nearly 30 years after the original theoretical proposal, concepts for the experimental detection of this phenomenon were introduced by Hirsch and Zhang. Hirsch proposed a reciprocal effect to SHE: inverse spin Hall effect (iSHE), [69] in

which the spin current generates a transverse current of charge. When this charge current accumulates at the edges of the sample, the charge accumulation can be detected electrically as a voltage. Based on SHE and iSHE, Hirsch further proposed that charge current can be injected into part of a system to generate spin current. This spin current will be transferred to another part of the system, where it can be detected as a voltage because it has converted back to charge accumulation via iSHE. Zhang suggested that the edge spin accumulation produced by SHE could be detected electrically by attaching a ferromagnetic probe to the edge of the sample. [70] This method is based on changing the relative magnetic orientation of the ferromagnetic detector to the edge spin accumulation and measuring the accumulation's electro-chemical potential. Both of these methods were not realized experimentally until several years later. They have played key roles in establishing basic physical principles. They have also been utilized for both the electrical injection and detection of spin (charge) currents via SHE and iSHE in nonmagnetic materials. In reality, connecting SHE systems with a ferromagnet for spin injection and detection has powered numerous important studies of SHE and its inverse process.

Hirsch and Zhang's proposals mainly apply to metals. However, the first time researchers observed SHE was in a semiconductor system by optical detection. [71] This is because there is also strong spin-orbit coupling in semiconductors, making it easier to produce a high SHE signal. Also, the SHE in semiconductors is generally extrinsic, i.e. induced by scattering from impurities, etc.

In 2006, Valenzuela and Tinkham performed direct electrical detection for iSHE experiments in metallic lateral spin valves at 4 K; this is shown in **Figure 2.7**. [72] A spin current was injected from a ferromagnetic CoFe electrode into a non-

magnetic aluminum Hall bar (NM channel). An external sweeping field was applied perpendicular to the sample plane to change the out-of-plane component of the magnetization of the CoFe spin injector. The polarization of the injected spin current can be changed by this field. As proposed by Hirsch, the transverse voltage across the Hall bar would be proportional to the out-of-plane component of the spin polarization of the injected spin current. The spin Hall angle, which is defined as the ratio of produced spin current to the injected charge current, was around $1\sim3 \times 10^{-4}$, which fit very well with the theoretical estimate for extrinsic iSHE in Al.

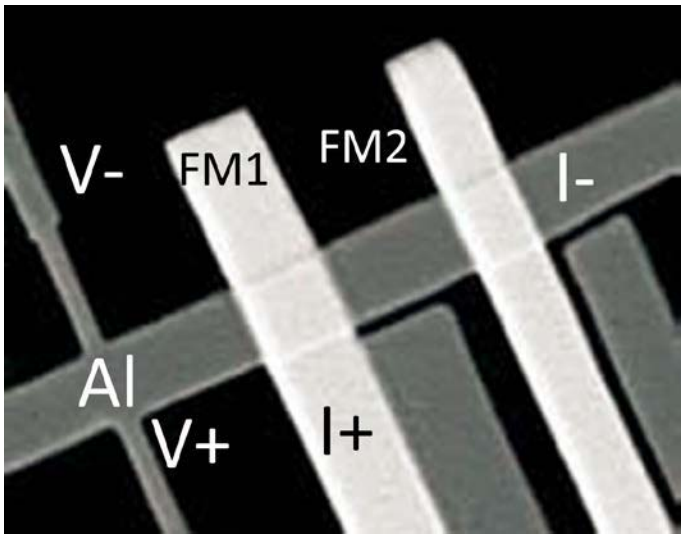

Figure 2.7: A scanning electron micrograph of the device and the measurement scheme for iSHE in Aluminum. Reprinted with permission from [72].

Following the exciting outcome described above, Kimura *et al*. demonstrated iSHE and SHE in a mesoscopic Pt stripe connected to a NiFe/Cu lateral spin valve; this is shown in **Figure 2.8**. [73] The external field was applied in the sample plane parallel to the hard axis of NiFe along the *x* direction. The first step in this process was

using NiFe as a spin injector and measuring iSHE across the Pt stripe. The injected spin current flowed through the Cu channel and was absorbed into the Pt stripe. A charge voltage developed between the two ends of the Pt stripe due to the iSHE. In a direct SHE measurement setup, the measurement configuration is inverted so that the charge current is passed through the Pt stripe, generating a transverse spin current via SHE. The spin current is then diffused into the Cu channel and detected by measuring the NLSV spin signal between the NiFe electrode and the Cu channel. The data of this research provided experimental evidence of the Onsager reciprocal relationship of SHE and iSHE as a spin injection and detection tool. This was the first time that researchers had measured SHE/iSHE in a noble metal (Pt); theorists had previously predicted it to have a large spin-orbit coupling. The SHA was as large as 0.021, which was the largest SHA that had been detected at that time.

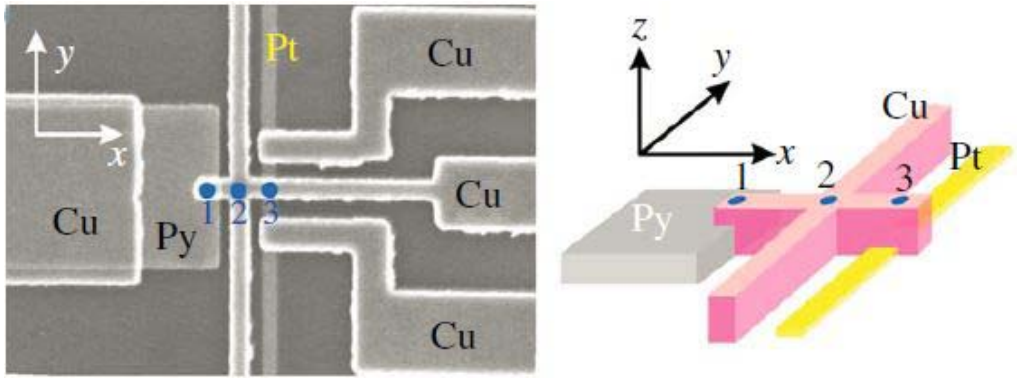

Figure 2.8: Left: a scanning electron microscope of Kimura's reversible SHE device. Right: a scheme for showing the arrangement of the device in 3D. Reprinted with permission from [73].

Kimura *et al*. also researched the temperature and size dependence of the SHE/iSHE signal in Pt wire by spin absorption. [74] A structure similar to an NLSV

with a line of the interested material (Pt) inserted parallel to the original ferromagnetic injector and detector was used for this research. According to spin absorption theory, spin current prefers to be absorbed into materials with smaller “spin resistance”; this is similar to charge current tending to flow into areas of lesser resistance. [35] Since the spin resistance of Pt is much smaller than that of Cu, a substantial amount of spin current was absorbed into the inserted Pt wire. The researchers found that the spin Hall conductivity in Pt is smaller at low temperatures and larger at RT, which could be due to the dominant contribution of impurities instead of the band structure in the Pt wires. In other words, the major mechanism for SHE in Pt is extrinsic rather than intrinsic due to side jumps.

Inspired by this result, a flux of research sprang up based on various techniques. Besides the spin absorption methods mentioned above, researchers also used spin pumping for spin current generation and transport into SHE materials. [75] Additionally, SHE has been used as a spin current generator and detector for other research (i.e., on the spin Seebeck effect). [66] The research on electrical spin injection in lateral spin valves has been extended to search for larger spin Hall angle (SHA) materials. Niimi *et al.* found out that Cu with small impurities of some transition metals, such as iridium, bismuth, etc. (0.1~0.5%), will induce huge SHA due to higher chance for being scattered. The SHA angle was as large as 0.24 in CuBi. The experimental setup of this was similar to the spin absorption method, except that the middle channel was substituted as needed. [76-78] These results point to a new direction for SHE research.

2.6.2 Controversies Over Spin Hall Effect Research

The initial controversies of SHE research mainly centered on the origins of SHE in different kinds of materials, focusing on whether this was dominated by intrinsic or extrinsic mechanisms. [79, 80] With the rapid development of applications involving SHE (such as current-induced spin torque switching for magnetic bilayers), these debates are maturing and transferring into the domains of SHA and spin diffusion lengths in certain noble and transition materials like Pt or Ta. This foregrounded controversy was triggered by a pioneer work by I. M. Miron *et al*. about the Rashba effect-induced switching of the perpendicular anisotropy Co layer in asymmetric, magnetic, single-layer structures. [81-83, **Fig. 2.9(a)**]

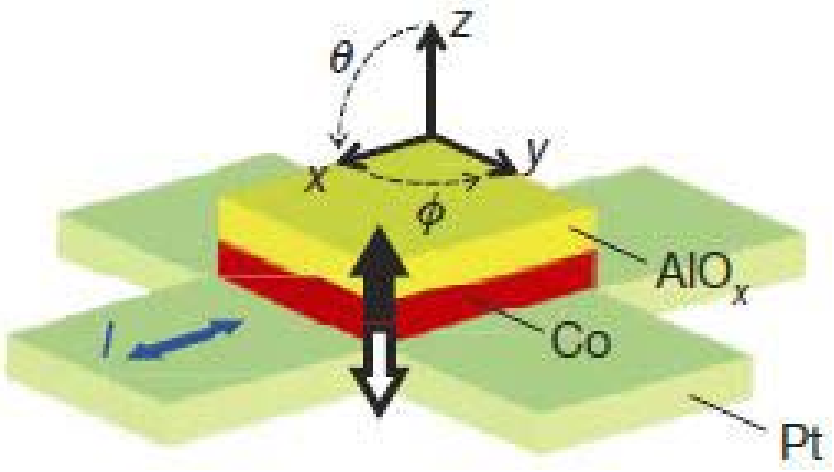

Figure 2.9: (a) I. M. Miron's Hall cross device schematic and current-induced switching geometry. Black and white arrows indicate the "up" and "down" equilibrium magnetization states of the cobalt layer, respectively. Reprinted with permission from [83].

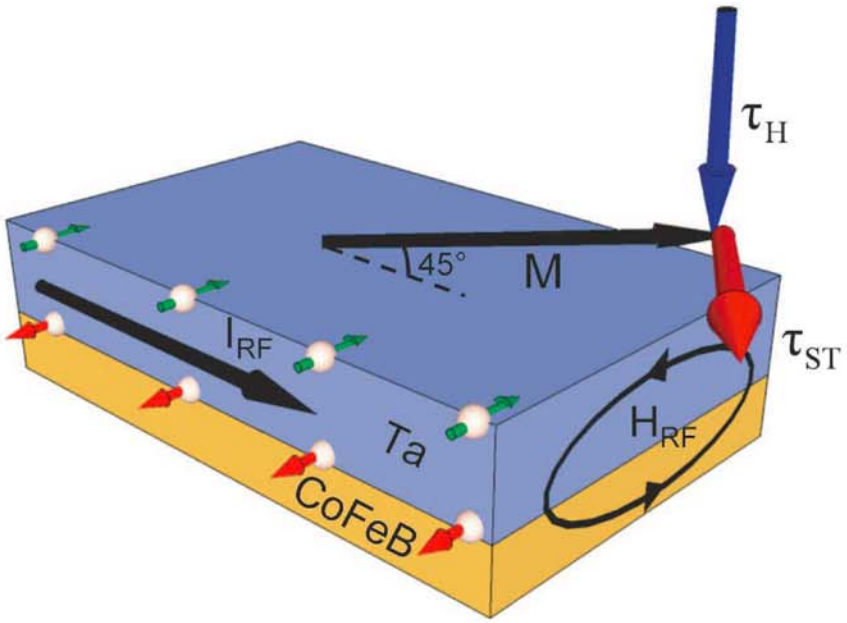

Figure 2.9: (b) Sample geometry for the ST-FMR measurement in Luqiao Liu's experiments. I_{RF} is the applied radio frequency current. H_{RF} is the corresponding Oersted field. $\vec{\tau}_H = -\vec{M} \times \vec{H}_{RF}$ is the torque on the magnetization due to the Oersted field and $\vec{\tau}_{ST}$ is the torque from the spin Hall effect. Reprinted with permission from [84].

These researchers claimed that the electric charge flow in Pt would experience strong spin-orbit coupling (SOC) and produce a Rashba effective field, which would be responsible for the switching of the adjacent single Co layer. On the other hand, Liu *et al*. conducted current-induced switching experiments in heavy-metal/ferromagnetic bilayers and concluded that single magnetic layer switching could be due to SHE instead of a Rashba effective field. [84] They also commented on Otani's nonlocal SHE measurements and pointed out that shunting currents from the Cu channel contacting a Pt stripe would dramatically reduce the estimation of spin signals and SHA. They designed another measurement technique, reevaluating the SHA measurements and calculations from microwave spin dynamic methods that had been

used by other groups. They believed the incorrect estimation of spin diffusion length in Pt or Ta should be partially responsible for such a large discrepancy in SHA values. [85] This would alter the debates and provide a new experimental way for characterizing SHE. **[Fig. 2.9 (b)]** Relatedly, there are plenty of publications that focus on measuring SHA and estimating spin diffusion length in Pt/Ta. Junyeon Kim *et al*. [86] and Xin Fan *et al*. [87] found that there is thickness dependence in the mechanism for spin torque switching. The effective field that is induced by spin current even changed sign when the thickness of the Ta layer decreased below 1 *nm*, meaning that there could be other competing effects contributing to it. Kevin Garello *et al*., [88] additionally, developed a 3D vector measurement technique, implying that further explanation and theory beyond the Rashba effect is needed to understand SHE. These researchers found that the effective field $B^{\perp}$ (perpendicular to both current direction and out-of-plane z direction; see **Fig. 2.10**) that is generated by the injected current also contains magnetization-dependent components perpendicular to the current itself. However, the Rashba model can only explain the components that are generated parallel to the current. This indicates that the previous theory of a spin transfer torque-like component induced by the Rashba effective field, or the theory of the spin torque-induced, field-like component, has to be corrected or extended. Also, Otani's group tried to verify the spin diffusion length in Pt by using the weak anti-localization (WAL) method. [89] They measured spin diffusion length in Pt by using both the spin absorption method in lateral spin valves and the WAL method at extremely low temperatures. They argued that both techniques show similar spin diffusion length in Pt, which is comparable to previous measurements. The SDL that these researchers obtained is much longer than that from Liu's measurements, meaning that Liu's

argument about discrepancy in spin diffusion lengths could not be the reason for underestimating the SHA.

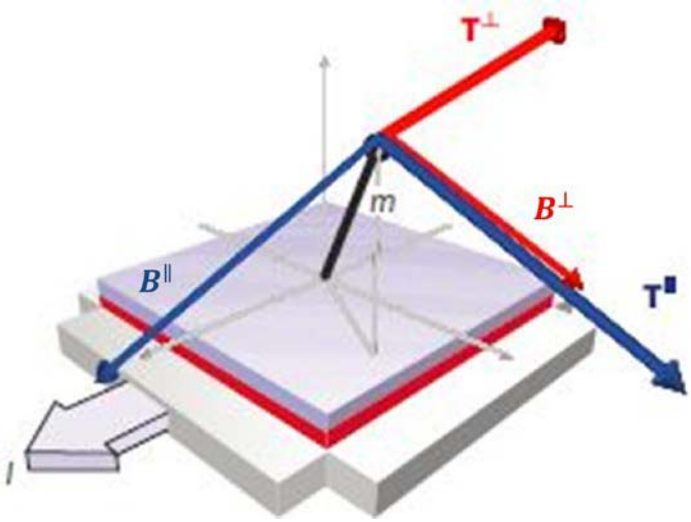

Figure 2.10: AlO_x/Co/Pt Hall cross with current and voltage leads. The thick arrows indicate the direction and amplitude of $T^{\perp}$ (red) and $T^{\parallel}$ (blue). The thin arrows indicate the equivalent fields $B^{\perp}$ (red) and $B^{\parallel}$ (blue). Reprinted with permission from [88].

Owing to the attention paid to SHE research and the heavy debates about it, we decided to conduct SHE measurements in NLSVs with new features. In our work, an oxide layer was placed between the noble metal stripe and the Cu channel in order to reduce the shunting effect and increase the accuracy of our measurements. Note that all previous SHE research used ohmic contacts for spin injection and detection. The details of this work will be presented in Chapter 7. [90]

REFERENCES

[1] M. N. Baibich, J. M. Broto, A. Fert, *et al*., Physical Review Letters, **61**, 2472 (1988).

[2] G. Binasch, P. Grunberg, F. Saurenbach, *et al*., Physical Review B, **39**, 4828 (1989).

[3] Wolf, S. A., D. D. Awschalom, R. A. Buhrman, *et al*., Science, **294**, 1488 (2001).

[4] I. Žutić, J. Fabian, and S. Das Sarma, Review of Modern Physics, **76**, 323 (2004).

[5] J. M. D. Coey, *Magnetism and Magnetic Materials*, 2010: Cambridge University Press.

[6] http://en.wikipedia.org/wiki/Hans_Christian_%C3%98rsted#cite_note-5.

[7] http://en.wikipedia.org/wiki/Andr%C3%A9-Marie_Amp%C3%A8re.

[8] http://en.wikipedia.org/wiki/Michael_Faraday.[9] http://en.wikipedia.org/wiki/Magneto-optic_effect.

[10] D. J. Griffith, *Introduction to Electrodynamics*, 4th ed, 2012: Addison-Wesley.

[11] R. Shankar, *Principles of quantum mechanics*, 1980: Plenum Press, New York.

[12] Max Born, Atomic physics, 1969: Blackie Press, London.

[13] R. C. O'Handley, *Modern Magnetic Materials*, 2000: John Wiley & Sons, Inc.

[14] N. F. Mott, Proceeding of Royal Society A, **153**, 699 (1936).

[15] A. Fert and I. A. Campbell, Physical Review Letters, **21**, 1190 (1968).

[16] A. Fert and I. A. Campbell, Journal of Physics Colloq. (Paris), **32**, C1 (1971).

[17] A. Fert and I. A. Campbell, Journal of Physics F: Met. Physics, **6**, 849 (1976).

[18] J W F Dorleijn and A R Miedema, Journal of Physics F: Met. Phys. 5 487 (1975).

[19] A. Fert, Review of Modern Physics, **80**, 1517 (2008).

[20] S. S. P Parkin, N. More, and K. P. Roche, Physical Review Letters, **64**, 2304 (1990).

[21] T. Shinjo and H. Yamamoto, Journal of Physical Society Japan, **59**, 3061 (1990).

[22] X. J. Wang, Dissertation for PhD degree at University of Delaware, (2010).

[23] W. P. Pratt, *et al*., Physical Review Letters, **66**, 3060 (1991).

[24] J. Bass and W. P. Pratt Jr, Journal of Physics: Condensed Matter, **19** 183201 (2007).

[25] T. Miyazaki and N. Tezuka, Journal of Magnetism and Magnetic Materials, **139**, 231 (1995).

[26] J. S. Moodera, L. R. Kinder, T. M. Wong, and R. Meservey, Physical Review Letters **74**, 3273 (1995).

[27] S. S. P. Parkin, *et al*., Nature Materials, **3**, 862 (2004).

[28] S. Yuasa, *et al*., Nature Materials, **3**, 868 (2004).

[29] M. Jullière, Physical Letter A, **54**, 225 (1975).

[30] J. Mathon and A. Umerski, Physical Review B, **60**, 1117 (1999).

[31] Ph. Mavropoulos, N. Papanikolaou, and P. H. Dederichs, Physical Review Letters, **85**, 1088 (2000).

[32] X. G. Zhang, and W. H. Butler, Physical Review B, **70**, 172407 (2004).

[33] M. Bowen, et al., Applied Physics Letters, 82, 233 (2003).

[34] S Takahashi and S Maekawa, Physical Review B, **67**, 052409 (2003).

[35] S Maekawa (ed), *Concepts in Spin Electronics*, 2006: Oxford University Press.

[36] S. Takahashi and S. Maekawa, Science and Technology of Advanced Materials, **9(1)**, 014105 (2008).

[37] Evgeny Y. Tsymbal and Igor Zutic, *Handbook of Spin Transport and Magnetism*, 2011: CRC Press.

[38] A. G. Aronov and G. E. Pikus, JETP Letter, **24**, 32 (1976).

[39] P. C. van Son, H. van Kempen, and P. Wyder, Physics Review Letter, **58**, 2271 (1987).

[40] M. Johnson and R. H. Silsbee, Physical Review Letters, **55**, 1790 (1985).

[41] F. J. Jedema, A. T. Filip, and B. J. van Wees, Nature, **410**, 345 (2001).

[42] F. J. Jedema, H. B. Heersche, A. T. Filip, *et al*., Nature, **416**, 713 (2002).

[43] J. Hamrle, T. Kimura, Y. Otani, *et al*., Physical Review B, **71**, 094402 (2005).

[44] T. Kimura and Y. Otani, Physical Review Letters, **99**, 196604 (2007).

[45] T. Kimura, Y. Otani, and J. Hamrle, Physical Review B, **73**, 132405 (2006).

[46] T. Kimura, J. Hamrle, and Y. Otani, Physical Review B, **72**, 014461 (2005).

[47] T. Kimura, Y. Otani, and P.M. Levy, Physical Review Letters, **99**, 166601 (2007).

[48] Y. Fukuma, L. Wang, H. Idzuchi, *et.al*, Nature Materials, **10**, 527 (2011).

[49] S. Chen, H. Zou, S. T. Chui, and Y. Ji, Jounral of Applied Physics, **114**, 223906 (2013).

[50] S. T. Chui and Z. F. Lin, Physical Review B, 77 (9), 094432 (2008).

[51] S. T. Chui, "Multiple magnetic tunnel junctions", U.S. Patent 5757056, May 26, 1998.

[52] S. O. Valenzuela, D. J. Monsma, C. M. Marcus, *et.al*, Physical Review Letters, **94**, 196601 (2007).

[53] F. Casanova, A. Sharoni, M. Erekhinsky, and I. K. Schuller, Physical Review B, **79**, 184415 (2009).

[54] X. J. Wang, H. Zou, and Y. Ji, Physical Review B, **81**, 104409 (2010).

[55] X. J. Wang, H. Zou, L. E. Ocola, and Y. Ji, Applied Physics Letters, **95**, 022519 (2009).

[56] G. Mihajlovic, J. E. Pearson, S. D. Bader, and A. Hoffmann, Physical Review Letters, **104**, 237202 (2010).

[57] Y. Ji, A. Hoffmann, J. S. Jiang, and S. D. Bader, Applied Physics Letters, **85**, 6218 (2004).

[58] H. Zou and Y. Ji, Applied Physics Letters, **101**, 082401 (2012).

[59] S. Chen, H. Zou, C. Qin, and Y. Ji, Applied Physics Express, **7**, 113001 (2014).

[60] R. Urban, G. Woltersdorf, and B. Heinrich, Physical Review Letters, **87**, 217204 (2001).

[61] Y. Tserkovnyak, A. Brataas, and G. E. W. Bauer, Physical Review Letters, **88**, 117601 (2002).

[62] J. C. Slonczewski, Journal of Magnetism and Magnetic Materials, **159**, L1 (1996).

[63] L. Berger, Physical Review B, **54**, 9353 (1996).

[64] J. A. Katine, F. J. Albert, R. A. Buhrman, *et al*., Physical Review Letters, **84**, 3149 (2000).

[65] A. Brataas, Y. Tserkovnyak, G. E. W. Bauer, and P. J. Kelly, Preprint at http://arXiv.org/abs/1108.0385, (2011).

[66] K. Uchida, S. Takahashi, K. Harii, *et al*., Nature, 455 (2008).

[67] S. Y. Huang, X. Fan, D. Qu, *et al*., Physical Review Letters, **109**, 107204 (2012).

[68] M. I. Dyakonov and V. I. Perel, Physical Letters A. **35**, 459 (1971).

[69] J. E. Hirsch, Physics Review Letters, **83**, 1834 (1999).

[70] S Zhang, Physics Review Letters, **85**, 393 (2000).

[71] Y. K. Kato, R. C. Myers, A. C. Gossard, and D.D. Awschalom, Science, **306**, 1910 (2004).

[72] S. O. Valenzuela and M. Tinkham, Nature, **442**, 176 (2006).

[73] T. Kimura, Y. Otani, T. Sato, *et al*., Physical Review Letters, **98**, 156601 (2007).

[74] L. Vila, T. Kimura, and Y. Otani, Physical Review Letters, **99**, 226604 (2007).

[75] K. Ando, S. Takahashi, K. Harii, *et al*., Physical Review Letters, **101**, 036601 (2008).

[76] M. Morota, Y. Niimi, K. Ohnishi, *et al*., Physical Review B, **83**, 174405 (2011).

[77] Y. Niimi, M. Morota, D. H. Wei, *et al*., Physical Review Letters, **106**, 126601 (2011).

[78] Y. Niimi, Y. Kawanishi, D. H. Wei, *et al*., Physical Review Letters, **109**, 156602 (2012).

[79] T. Jungwirth, Q. Niu, and A. H. MacDonald, Physical Review Letters, **88**, 207208 (2002).

[80] J. Sinova, *et al*., Physical Review Letters, **92**, 126603 (2004).

[81] I. M. Miron, G. Gaudin, S. Auffret, *et al*., Nature Materials, **9**, 230 (2010).

[82] I. M. Miron, T. Moore, H. Szambolics, *et al*., Nature Materials, **10**, 419 (2011).

[83] I. M. Miron, K. Garello, G. Gaudin, *et al*., Nature, **476**, 189 (2011).

[84] L. Liu, C. F. Pai, Y. Li, *et al*., Science, **336**, 555 (2012).

[85] L. Liu, R. A. Buhrman, and D. C. Ralph, arXiv:1111.3702 (2011).

[86] J. Kim, J. Sinha, M. Hayashi, *et al*., Nature Materials, **12**, 240 (2012).

[87] X. Fan, J. Wu, Y. Chen, *et al*., Nature Communications, **4**, 1799 (2013).

[88] K. Garello, I. M. Miron, C. O. Avci, *et al*., Nature Nanotechnology, **8**, 587 (2013).

[89] Y, Niimi, D. Wei, H. Idzuchi, *et al*., Physical Review Letters, **110**, 016805 (2013).

[90] S. Chen, C. Qin, and Y. Ji, *et al*., Applied Physics Letters, **105**, 082402 (2014).

Chapter 3

EXPERIMENTAL METHODS

This chapter will review the instruments and experimental techniques that we used in this work.

3.1 Lithography

Lithography is a method of printing original, specific patterns onto a desired base with chosen materials. It is the major pattern-transferring scheme for integrated circuits and microelectromechanical systems. Two kinds of lithography techniques were used in this work: photolithography, for creating contact pads, and electron beam lithography, for fabricating nanoscale nonlocal spin valves (NLSVs) on substrates.

3.1.1 Photolithography

In photolithography, a specially processed light is used to transfer a geometric pattern from a photomask onto a light-sensitive, chemical “photoresist” on the substrate. A photomask is a soda lime glass that bears patterns composited of chrome. The chrome element stops light from forming shadows, while the non-chrome element lets light pass through for exposure. A series of chemical treatments either engrave the exposure pattern or enable the deposition of a new material into the desired pattern trenches on the bottom layer under the photo resist. The whole process is similar to photography. It can create extremely small patterns (down to a few tens of nanometers in size) and afford exact control over the shape and size of the objects being built. Also, it can create patterns over a large surface cost-effectively. The photoresist is

removed via proper methods after designed patterns of materials have been imprinted on the substrate. [1]

In this dissertation, photolithography was used to pattern external contact pads (scaled from 20 μm to 2 mm). In **Figure 3.1 (g)**, we can see that both the large contact pads and the alignment marks for next-step e-beam lithography are made by photolithography.

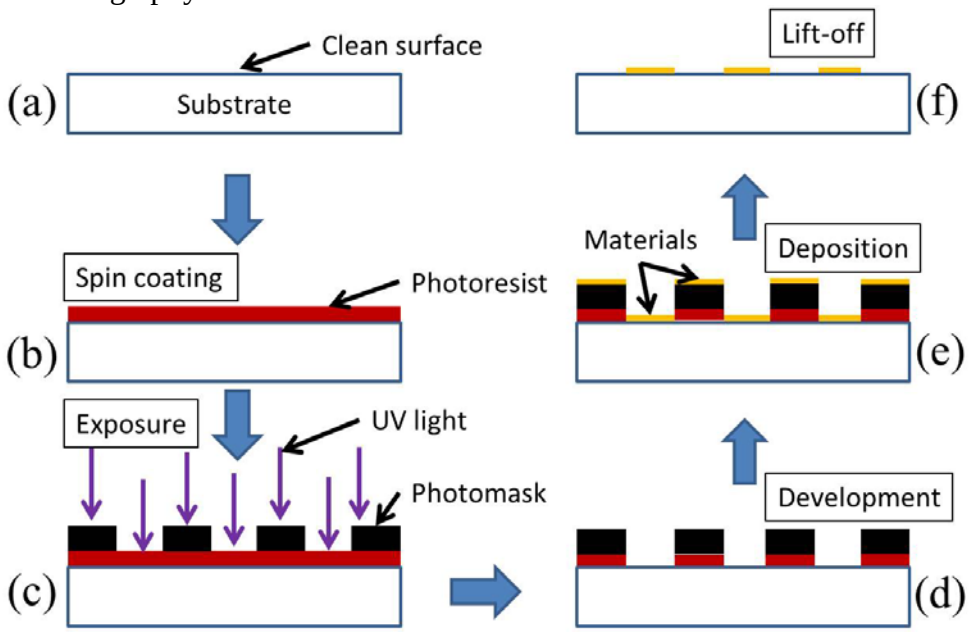

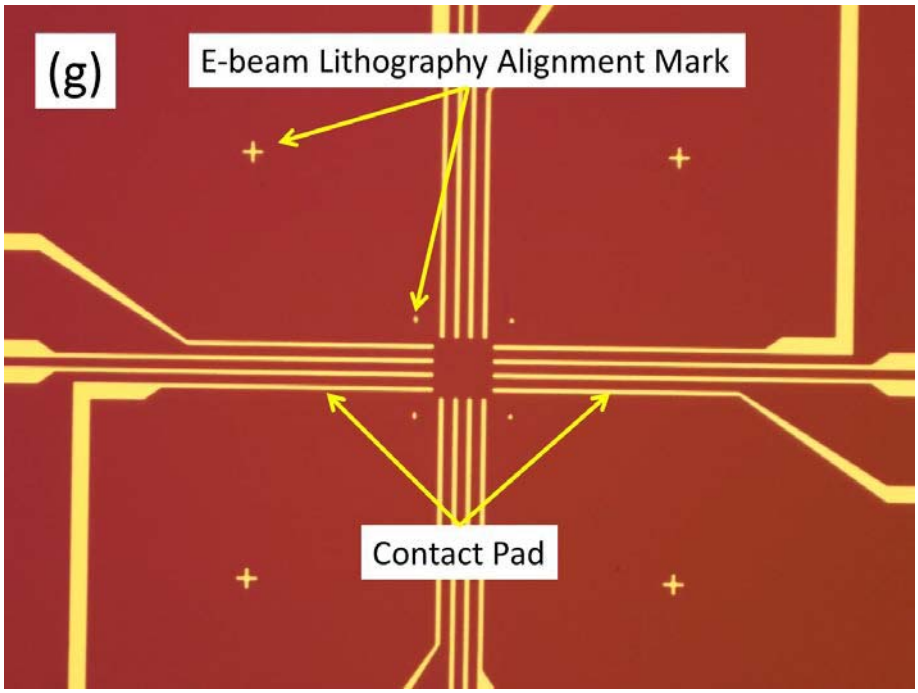

Figure 3.1: (a) Silicon wafer substrate with a clean surface; (b) spin coating for positive photoresist; (c) exposure with photo mask by UV light from photolithography machine; (d) development for exposed photoresist for leaving space for filling in materials; (e) deposition for desired materials; (f) lift-off photoresist residue, leaving only materials on substrate in designed patterns. (g) Photo pattern after lift-off, taken by optical at 100X.

As in semiconductor manufacturing and processing, the silicon wafers that are used in this process need to be cleaned at the very first stage of fabrication. They are dipped into acetone, ethanol, and deionized (DI) water, then into an ultrasonic cleaner for 15 minutes each. The photomask is rinsed by acetone, ethanol, and DI water in order to clean both the front and the back side simultaneously. It is then dried by blowing N_2. Afterward, the photomask is put onto a Laurell spin processor for spin coating. A viscous, liquid solution of photoresist (AZ 1512, AZ Electronic Materials USA Corp) is dispensed onto the wafer while it spins rapidly, producing a uniform,

thick layer due to centripetal force. The rotation is about 4000 rpm for 60 secs. The thickness of the photoresist is about 1.4 μm. The wafer is then pre-baked on a hotplate at 115 C for 60 secs in order to drive off any excess photoresist solvent and moisture. Following this, the substrate with photoresist is exposed on an OAI Model 200 Mask Aligner. The mask and wafer are fixed in corresponding stages by vacuum. After careful alignment, the positive photoresist (with "positive" meaning that the parts exposed by UV light through the patterns will be removed in the next step's developer) is exposed to ultraviolet light with a wavelength of 320~380 nm through a dark field photomask for 6 secs. This exposure changes the chemical properties of the exposed photoresist by transferring it into a soluble matter. Next, the wafer is dipped into the developer (MF 319, AZ Electronic Materials USA Corp) for exposed photoresist removal, leaving trenches and spaces for metal refill deposition. Here, we put 40-50 nm of Au into designed trenches by electron beam evaporation, a process which will be explained in Section 3.2. Following this, the photoresist residue was removed by dipping the wafers into acetone for more than an hour and flushing them with acetone, ethanol, and DI water. Sometimes, the ultrasonic cleaner is again used to lift off any remaining photoresist residue.

3.1.2 Electron-Beam-Lithography

Electron beam lithography uses a focused electron beam to "draw" designed patterns on e-beam resist-covered substrates without a mask. This process is also called "maskless lithography," and its patterns are formed by pre-setting designed paths that are stored digitally for electron guns to follow. Electron beam lithography satisfies many requirements that photolithography does not, such as achieving higher resolution, flexibility, and efficiency in pattern modification (since it is modified via

computer only, with no physical masks) and line-width control, etc. It utilizes e-beam resist as the media for printing designed patterns. In this thesis, we used positive e-beam resist, meaning that the electron beam changed the chemical properties of the exposed parts, destroying the chemical bonds between polymer molecules to make them soluble in the developer. [2]

A typical electron beam lithography system consists of an electron gun, an electron optical column, and a vacuum chamber, which in turn consists of a laser-controlled x/y stage for accurately positioning the substrate during lithography. The electrons are produced by the electron emitter in the electron gun and accelerated by high voltage in the column to form an electron beam. The electron optical column contains a series of beam-controlling components like an electric lens, a magnetic lens, beam blankers, and deflectors. The electron beam is correspondingly modified as it passes through the optical column to have the required current intensity, spot size, and focus on the substrate.

The electron beam lithography in this work was performed on the Raith e-LiNE system at the NanoCenter of the University of Maryland (UMD). [**Fig. 3.2**]

Figure 3.2: A picture shows Raith e-LiNE machine we use in UMD.

There is an SEM installed in this machine that is named LEO 15XX. It is a fully computer-controlled instrument with thermal field emission filament technology. It has two major functions: imaging and e-beam lithography. There is also a camera that can be toggled with in-lens SEM in order to monitor the position of the stage in the chamber. A laser interferometer is employed in order to accurately control all motorized axes of the stage through an optical fiber. Outside of the chamber, control of the stage is accomplished by a dual joystick and by typing parameters onto a computer. This machine is also equipped with a load lock and a hard panel to properly set and adjust important parameters such as magnification and focus, stigmation, and beam alignment. The electron beam current is tuned by selecting the appropriate stage height, acceleration voltage, and aperture. [2]

There are several writing (exposure) schemes in the e-LiNE system: the stationary stage with a divided writing field, the round (Gaussian) beam, the vector scan, and the raster scan. We use the first scheme. Another important element is the write field, in which the writing is finished by deflecting the beam instead of moving the stage. The stage is only moved when the writing is performed outside of it. The write fields can vary from 500 nm to 2 mm; we used 100×100 μm for our wafers. The individual fields are written one at a time by scanning the beam within the field. Large area patterns are divided into small writing fields that are then stitched together.

Electron beam writing procedures include the following steps: sample loading, electron beam alignment, stage adjustment, electron beam optimization, write field alignment, exposure (electron beam writing), and sample unloading. After loading through the load lock and waiting for the vacuum to reach 10^{-9}, the stage is moved to a specific location (the Faraday cup) wherein the beam current is measured. During the electron beam alignment, the accelerating voltage and aperture are chosen. The sample stage is set to a proper working distance, and a clear SEM image is obtained by further adjusting the focus. The purpose of the stage adjustment is to build a relationship between two coordinate systems in e-LiNE: XYZ (the stage) and UVW (the sample). This must be accomplished while paying attention to shift, scale, and rotation in order to perform a permanent coordinate transformation between both systems. Within the e-LiNE software, there are two different transformations. The first one (XYZ) is called a global transformation, and the second one (UVW) is called a local transformation. The first one can be attached to the wafer itself, whereas the second one serves to guide navigation within a chip or a local interest area. The electron beam is then

further optimized by adjusting the focus, aperture and correcting the stigmation with respect to a certain sharp feature.

The write field alignment is the adjustment of the electromagnetic/electrostatic deflections system inside the column to the high precision XYZ stage. It relies on alignment marks deposited by previous photolithography. The stage and the e-beam deflection system are then considered to be in an aligned “correct" position. The write field alignment is needed because the electron beam for high resolution exposure passes through several stages, each having varying degrees of drift. Write field alignment not only reduces these variations, it also reduces the error between adjacent write fields for better “stitching.” We used four $20 \times 20\ \mu m^2$ photolithographic marks for write field alignment, located at the centers of the four write fields and covering the entire e-beam exposure area. During operation, e-LiNE attempted to search for these marks via self-alignment. We then used the manual alignment operation to correct any deviations.

In the exposure step, we set the step size and dose (i.e., the amount of electron charge needed for each unit length or unit area for exposure) and calculated the dwell time according to the beam current that was being measured. Take the area dose as an example. The relationship between the factors of area exposure is given by this formula:

$$D = \frac{I \cdot T}{A}$$

where D is the dose, I is the beam current, T is the time needed to expose the object (dwell time, or the amount of time that the beam waits at each step when exposing a specific area), and A is the area designed to be exposed. [3, 4]

We used both area and line doses for our samples. Area dose was utilized for large contact pads and some non-critical device areas like the spin injector and spin detector. Line dose is often used for features with a critical dimension smaller than 100 nm, such as a nonmagnetic channel. Due to the proximity effect (in which electrons from the exposure of an adjacent region spill over into the exposure of the currently written feature or spread into an area that is not intended to be exposed, effectively enlarging the critical dimension and reducing the contrast), however, some small-scale features do not sustain well or obey the original design. There are several ways to reduce this effect, such as using a thin resist layer or a low-impedance substrate, modifying the dose amount, or redefining the pattern file, etc.

In this work, we used two kinds of e-beam electron resists, Poly-Methyl Methacrylate (PMMA) as the top layer and Poly-Methyl Glutarimide (PMGI) to build up a double-layer shadow mask for angle deposition. After the Au in the contact pads on the wafers was evaporated via e-beam, PMGI was spun on the same spinner for photoresist coating, first as the bottom layer at 3000 rpm for 60 secs, then pre-baked at 210 C for 3 mins. The PMMA was spin-coated on top of this at 5000 rpm for 60 secs, then pre-baked at 190 C for 4 mins. Since PMGI has a higher sensitivity to electron beams than PMMA and a longer post-development period, it forms a structure that is similar to shadow masks. [**Fig. 3.3 (d)]** This technique allowed us to finish the NLSV fabrication without destroying the vacuum and to improve the quality of the interface between the nonmagnetic and magnetic materials. We also increased the speed of the process by skipping the step of pumping the chamber up and down. This also expedited the lift-off process. Further details of this procedure will be explained in Section 3.2.3.

The development of the e-beam resist was completed after a trip to the University of Maryland. For the development of the top layer PMMA, the sample was dipped into MIBK for 1 min 30 secs and rinsed by IPA for 30 secs, followed by 30 secs of DI water rinsing. The bottom layer PMGI was developed in Remover PG for 6 mins and rinsed by DI water for 30 secs. This will provide us with a much wider undercut for the shadow effect of the angle evaporation technique. Also, this shadow mask lets e-beam evaporation form NLSV structures in a single-step deposition without breaking the vacuum. The interfaces remain pristine and the time cost is reduced, since the deposition can be completed in one vacuum cycle. [5] The developed configuration is shown below in **Fig. 3.3 (h-k)**. The "shadow" that is made visually from the suspended mask in (j) can be seen around the edge of the developed area of PMMA in (h).

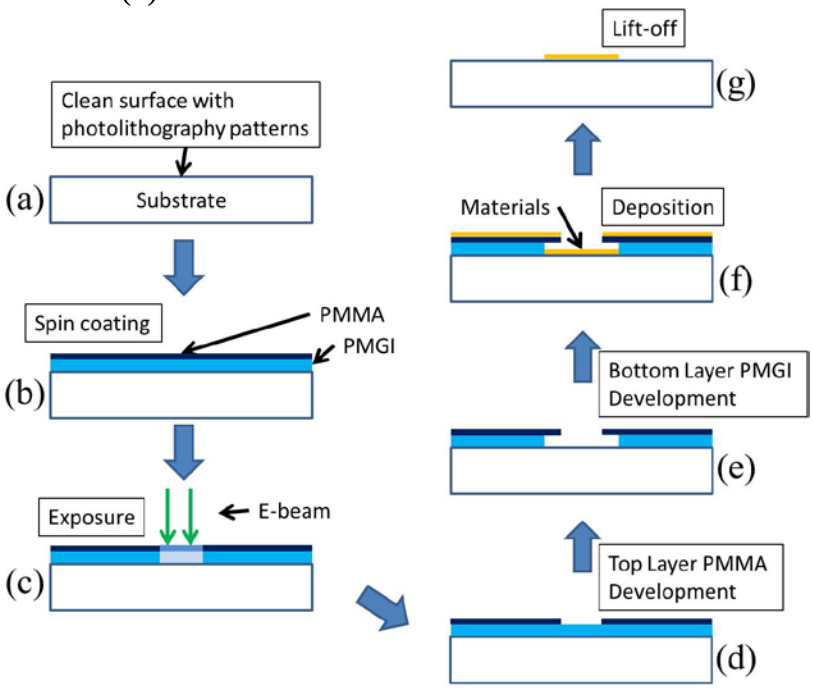

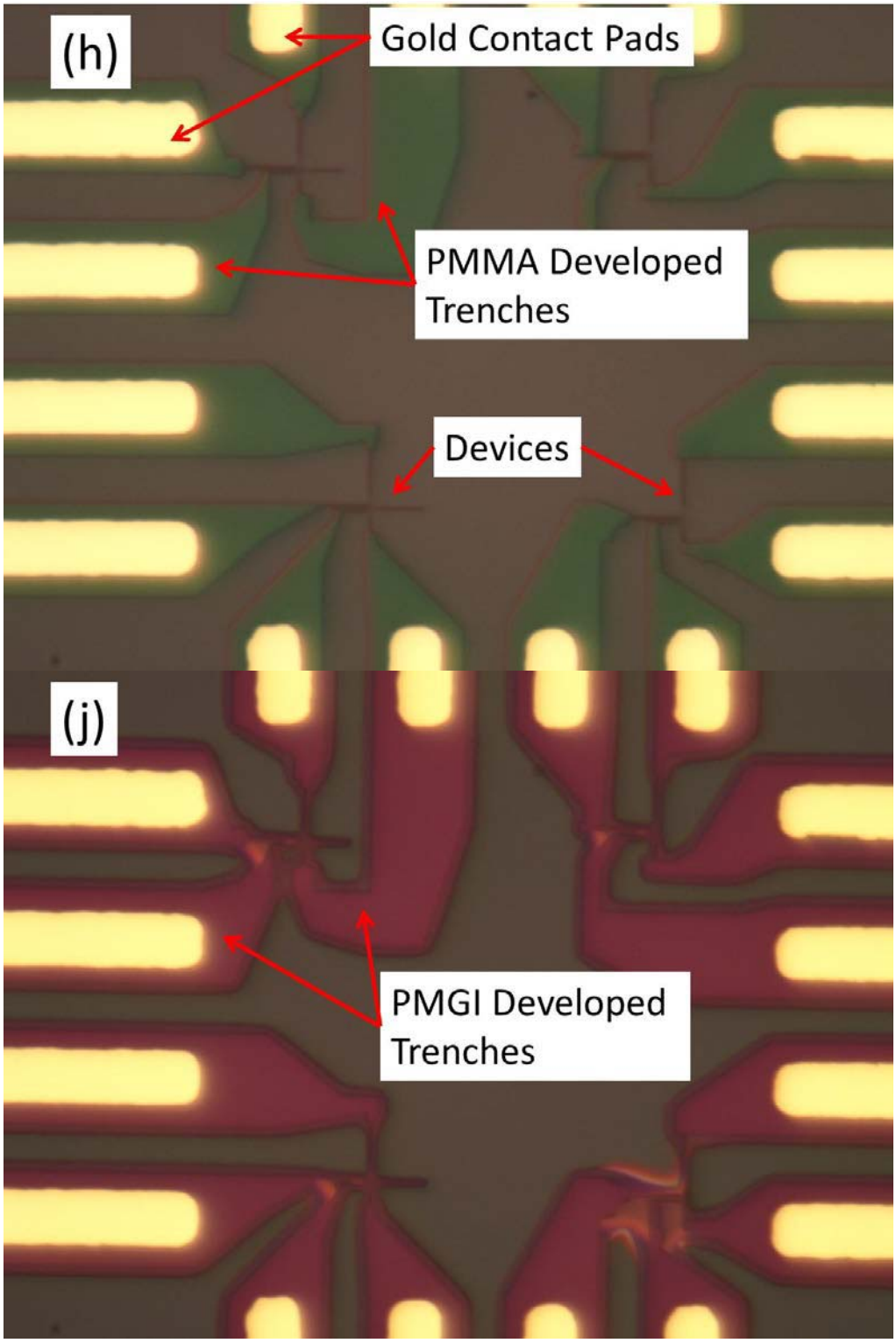
(h)
Gold Contact Pads
PMMA Developed Trenches
Devices
(j)
PMGI Developed Trenches

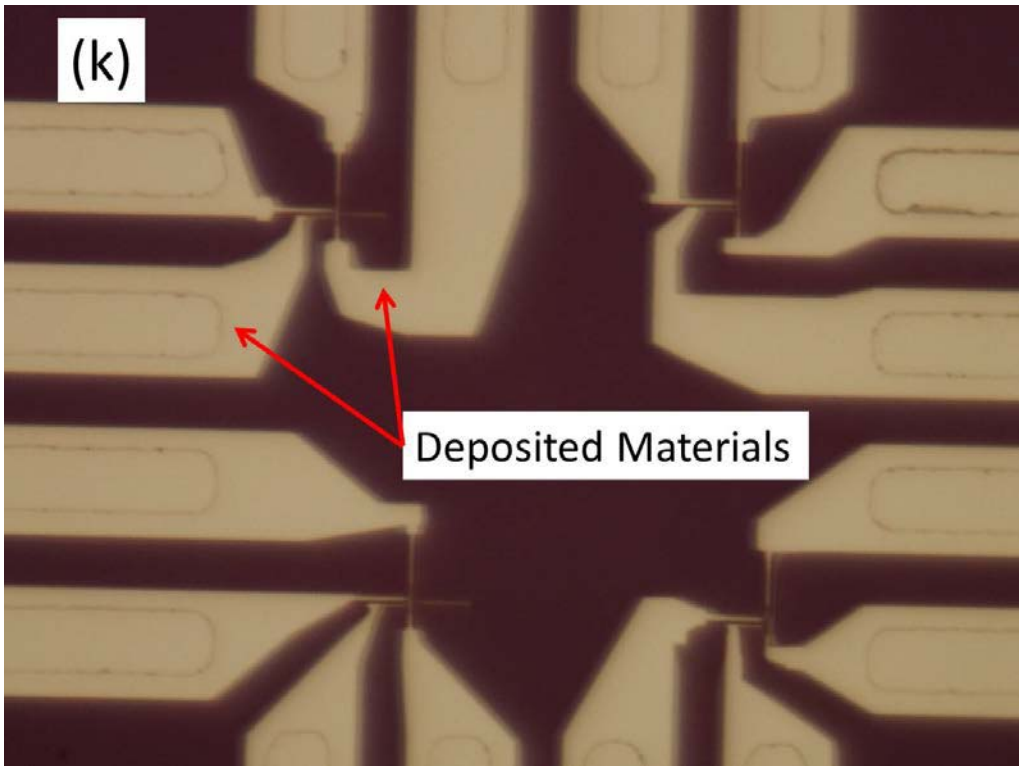

Figure 3.3: (a) Clean substrate with pre-photolithography patterns; (b) spin coating with double layer e-beam resist PMGI and PMMA; (c) Exposure by e-beam lithography; (d) & (e) two-step development for forming space for filling in materials; (f) deposited desired materials; (g) lift-off resist residue leaving only designed patterns; (h-k) show the optical pictures took after PMMA development, PMGI development, e-beam evaporation separately.

3.2 Electron Beam Evaporation

3.2.1 Principle

Electron beam (e-beam) evaporation in an ultrahigh vacuum system was used throughout this research. Magnetic and nonmagnetic thin films were deposited on the patterned substrate. The e-beam evaporation system and associated technical details for the production of the samples will be discussed in this section. The advantages of

e-beam evaporation are: 1) It is suitable for the production of large volumes, 2) it is compatible with a wide range of materials, most of them are metals, 3) its deposition can reach a very high growth rate with competitively thin film quality, and 4) it has good directivity and is suitable for angle evaporation.

3.2.2 High Vacuum Chamber

The self-design and assembly high vacuum chamber is shown in **Figure 3.4**. It can reach a vacuum of ~10^{-8} on the Torr scale. The diaphragm pump, also called the mechanical pump, is connected to the chamber body through a three-way valve to enable the venting of the pump port. The cryogenic pump in the back is used for maintaining a high vacuum condition, usually higher than 2×10^{-8} Torr. Before the chamber is exposed to the ambient pressure, a gate valve between the cryogenic pump and the main chamber is closed to allow the cryogenic pump to work without sucking in overwhelming impurities and contamination from the outside environment. The thickness crystal monitor is placed at the top right part of the chamber and connected to the outside controller through a port on the top plate. The cooling water is also connected to it in order to maintain a relatively low temperature for the chip. The ion gauge and the convection gauge are mounted on the left side of the chamber for monitoring the vacuum's condition during the sample loading/unloading and fabrication processes. The N_2 gas is vented through a three-way valve that is connected on the left side as well. On the front door, there is a viewport made of glass that enables the user to watch the actual evaporation taking place. The glass window is shielded by a rotatable flat panel when the deposition is in process so that no excessive material is deposited onto the glass's surface. The e-beam deposition system is located at the bottom of the chamber. There is also an ion beam emitter at the left bottom of

the chamber for ion milling cleaning. The maker is Kaufman & Robinson. About 600 volts need to be applied to accelerate the Ar+ and bombard the surface of the substrate to clean the deposited material.

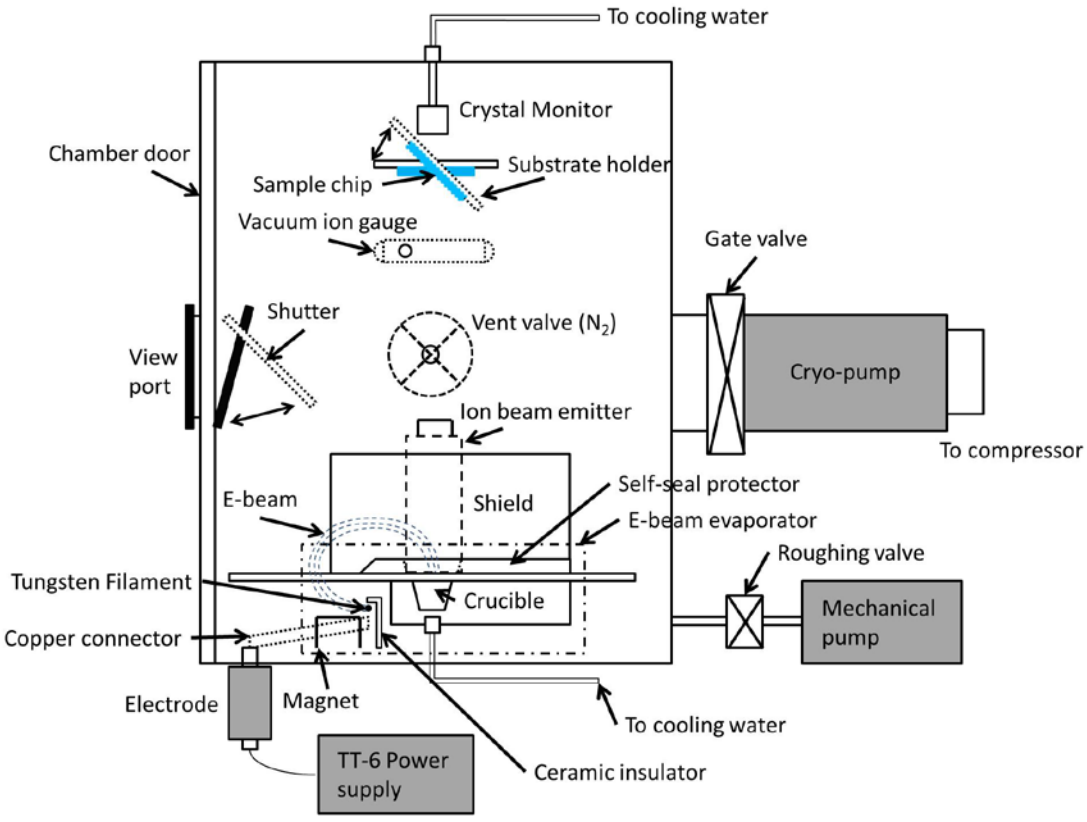

Figure 3.4: A schematic drawing of the vacuum chamber in Ji's group (right side view).

3.2.3 Electron Beam Evaporation System and Deposition Process

The Telemark TT-6 e-beam deposition system is installed at the bottom of the chamber for depositing thin films. The electron beam evaporation system involves the following components: a power supply, a system controller, the filament for emitting

electrons, the confocal electromagnetic system, the hearse with six crucibles for holding the evaporation materials, and the cooling water system. [6]

For every vacuum deposition cycle, samples need to be loaded first. In **Figure 3.4**, the sample chip is attached to the substrate holder (a copper panel mounted to the end of a 360-degree rotary feedthrough) by Kapton tape disks. Initially, the substrate faces upward in the chamber. After filling enough material into the crucibles for one deposition cycle, the door of the chamber must be closed for pumping down. It takes about 8 hours for the vacuum to reach the desirable value before the deposition. First, the mechanical pump pumps down the vacuum to 10^{-2} Torr with the gate valve closed. Next, the three-way roughing valve is closed to isolate the mechanical pump, with the gate valve open for continuous pumping by cryo-pump. After the vacuum is lower than 10^{-6} Torr, the main power supply can be turned on to heat the filament. We used a high voltage DC power supply during the deposition process. Typically, the voltage is in the range of 6.5~7.5 kilovolts. The current through the tungsten filament is adjusted manually from the controller with an increasing step size of 0.01A. When the filament is hot enough, electrons are emitted. These hot electrons form a beam that is deflected and focused toward the target material in the crucible by the external confocal magnetic fields; these have been tuned well before being installed in the chamber. The magnetic fields can shape and redirect the path of these random electrons. When the electrons hit the surface of the target materials, the kinetic energy of motion is converted into thermal energy. The target material is heated up and vaporized inside of the vacuum chamber. Its surface temperature can be as high as thousands of degrees Celsius, melting some materials. The evaporated materials condense on all surfaces in the chamber. A shield is needed around the source to

prevent thin films of materials from being over-coated onto the ion-emitting gun or other setups that sit near the source. The thicknesses of thin films are monitored by the crystal monitor. Since the monitor and the substrate are at different positions, there is a calibration factor between the values read from the monitor and the real thickness of the thin film. The crystal monitor is electrically connected to a thickness controller made by Maxtek that measures the thickness and deposition rates of various materials by adjusting certain parameters (like density and impedance) on the controller. [7] When the evaporation rate reaches a significant value, the substrate holder is flipped down toward the material source, and the shutter of the thickness monitor opens to monitor the thickness simultaneously. When the thickness reaches the desired value, the sample holder is flipped upward quickly, the current is decreased to turn off the filament emission, and the heated material cools down. The target material can be changed like a revolver by turning a chain-driven handle through a feedthrough at the right bottom of the chamber. Subsequent thin films are evaporated in a similar process. After the designed structure forms on the substrate and the entire chamber cools down, N_2 is vented in for opening the chamber.

There are a total of six crucibles for this electron beam evaporation system, and they are capable of holding six different target materials. To reduce the chance of cross-contamination between nonmagnetic and magnetic materials, four crucibles are often used to separate the magnetic and nonmagnetic sources, with the other two acting as barriers between them. As shown in **Figure 3.5**, the crucibles of 4 and 5 store magnetic materials like Co or Py. The crucibles of 1 and 2 contain the nonmagnetic channel materials like Cu or Ag. The crucibles of 3 and 6 either hold aluminum oxide or back up the other materials. In the image, port 3 is filled with Pt. We had two Cu

sources, since we used huge amounts of Cu for nonmagnetic channel deposition because of its high-purity requirement. All of the crucibles also have protective covers in order to avoid cross-contamination due to spitting or other reasons. Because of the heat generated by the electron beam, the crucible holder is water-cooled to prevent it from melting or being damaged.

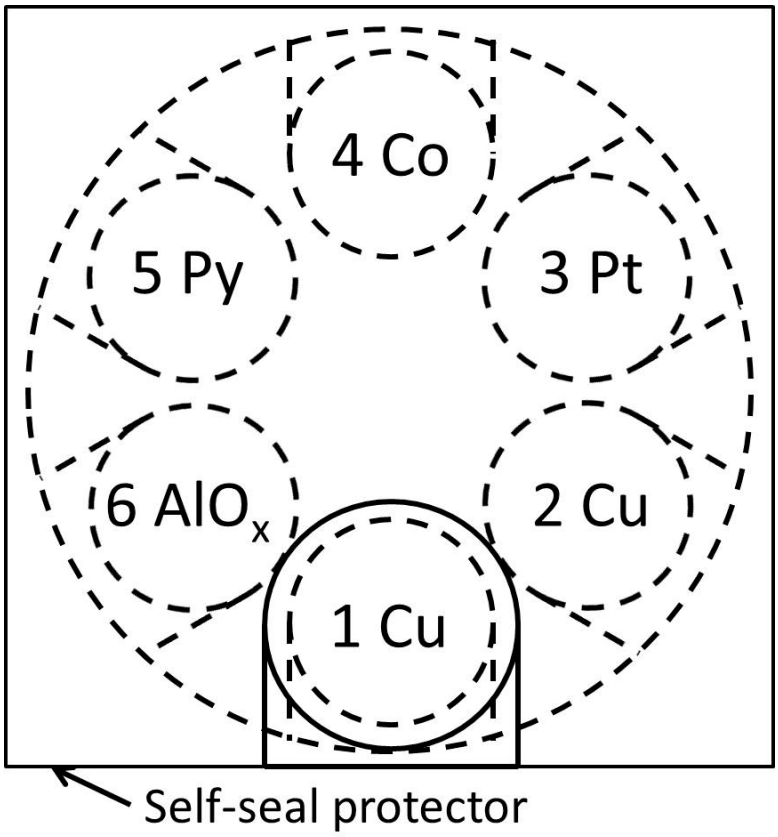

Figure 3.5: A schematic shows the crucible holding evaporation materials and the self-seal protector above it.

An oxide layer will typically be deposited only two minutes after the deposition of magnetic materials is complete. This is because the hot magnetic

materials can be oxidized or contaminated easily, deteriorating their magnetic properties. Some users even put an oxide layer onto the nonmagnetic channel in order to prevent further oxidation after unloading the chamber.

Here, we would like to introduce how we fabricated a nanoscale nonlocal spin valve by angle evaporation. We illustrate one of our samples in **Figure 3.6**.

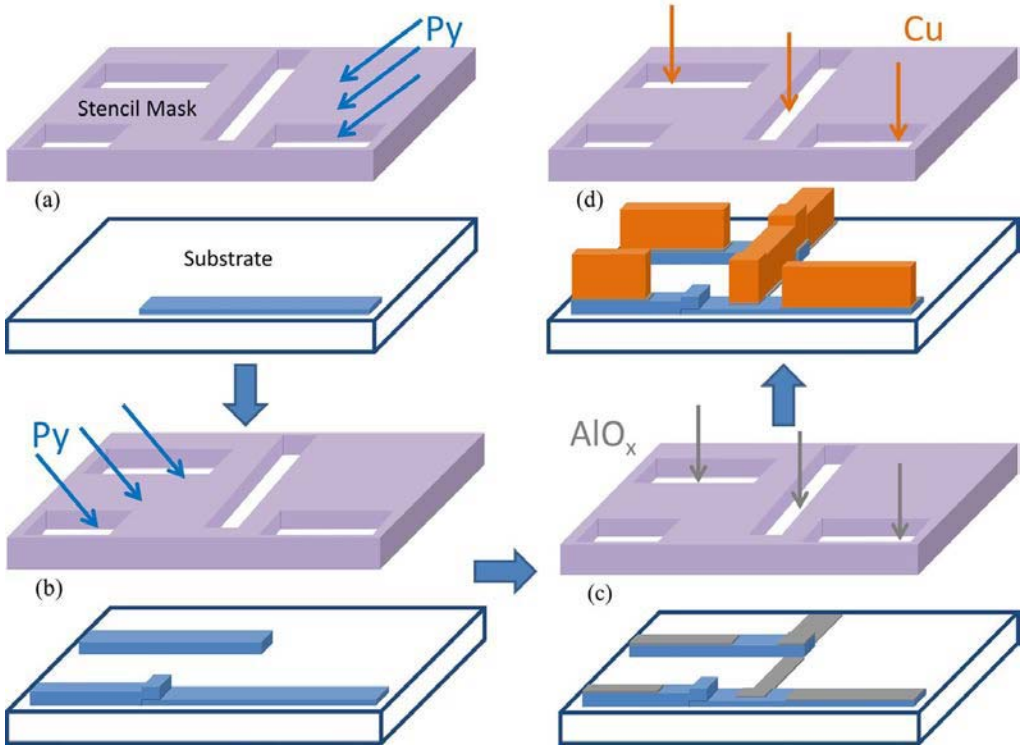

Figure 3.6: A step-step illustration for fabrication of a nanoscale spin valve. (a) and (b): Py is deposited through different large angles from two orientations to ensure connection with NM materials from future deposition; (c) and (d): AlO_x and Cu are deposited through normal direction.

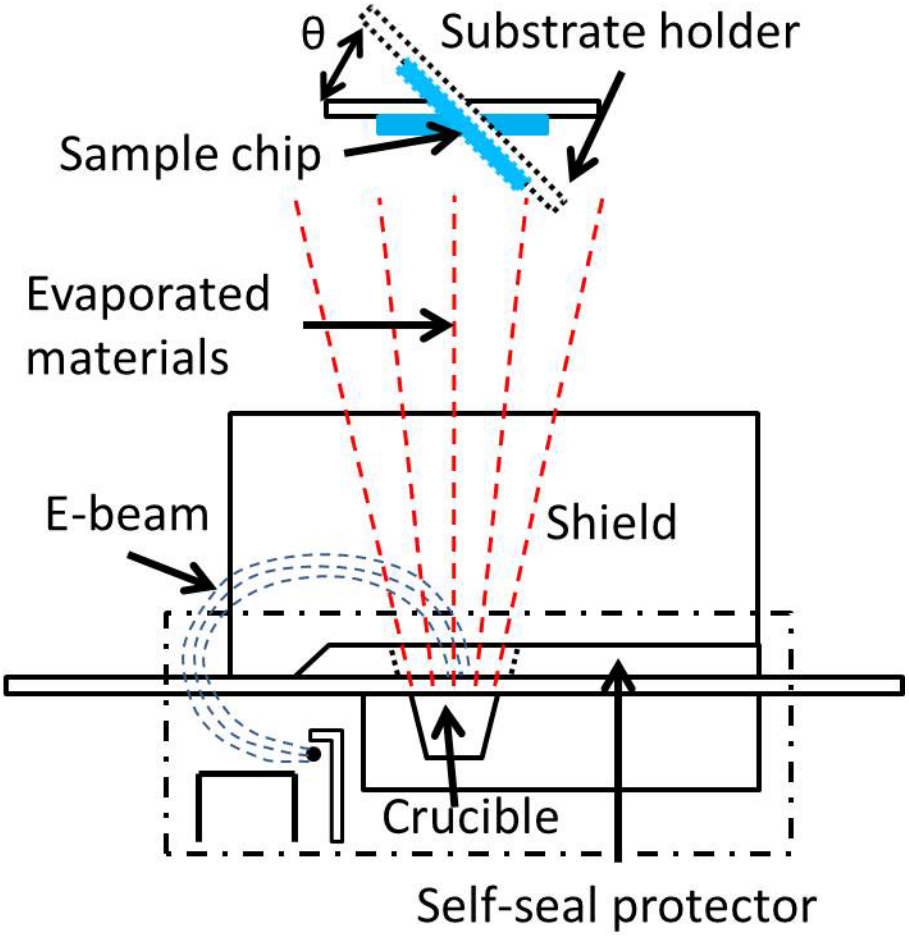

Figure 3.7: A schematic for e-beam angle evaporation for nanoscale structures.

Since the substrate holder is mounted on the end of a 360-degree rotary feedthrough, we can turn it to any angle from the horizontal plane as illustrated in **Figure 3.7**. Initially, the substrate faces upward in the chamber. During the deposition process, the DC voltage is turned on and gradually increases, heating up and vaporizing the target material. Once the deposition rate reaches the desired value and becomes stable, the substrate holder will quickly be rotated to a position in which the

evaporated material hits the substrate either directly or from a pre-calculated angle, depending on mask design. When a desired thickness is reached, the substrate holder is quickly flipped upward again. The DC voltage is then decreased to zero, and the target material cools down. We can then proceed to deposit other materials as planned until our whole structure is built. The relationship between the film thickness on the crystal monitor and the true deposition thickness on the substrate is given by:

$$Film\ thickness = Film\ thickness\ on\ the\ monitor \times \left(\frac{Distance\ from\ target\ to\ monitor}{Distance\ from\ target\ to\ substrate}\right)^2 \times \cos\theta,$$

where θ is the angle at which the evaporated material beam hits the substrate. Another way for obtaining the correct calibration factor is to deposit 10~20 nm of thickness (measured by the thickness monitor) and then calibrate it again by small-angle XRD. The factor can be calculated by taking the ratio of the values of the two thicknesses.

3.3 Measurement Techniques

NLSVs are typically measured by a four-point measurement system as shown in **Figure 3.8**: A DC/AC charge current is injected from the injector, and the voltage is measured across the interface of the detector. The charge current can be in either DC or AC format, and the detector's side needs corresponding voltage-detecting instruments. In this study, the AC current source is the Stanford Research Systems' SR830 DSP Lock-in Amplifier or the Keithley 6221 Precision DC/AC Current Source. The DC current source is the Keithley 6220 Precision DC Current Source. The SR830 DSP Lock-in Amplifier is the AC voltage signal detector itself, and the Keithley 2182A Nanovoltmeter is used as the DC voltmeter. There is also the Keithley 6430 Source Meter; the source meter is often used to measure interface resistance and I-V

curve characterization. It can also be used as a DC current/voltage/resistance precision meter (similar to a digital multimeter). The lowest limits of its current measurement are femto-ampere levels.

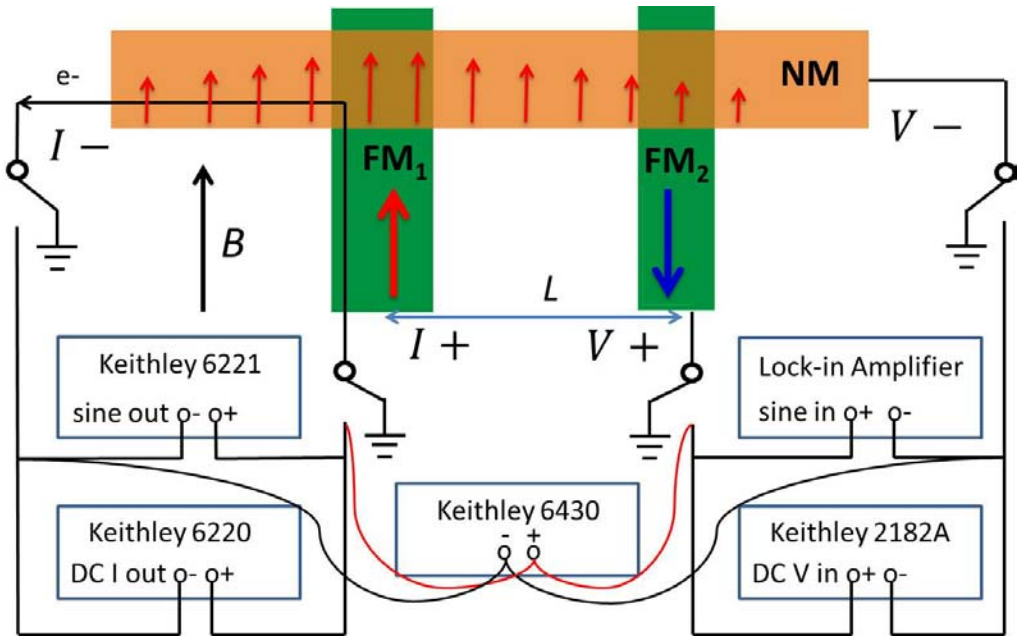

Figure 3.8: General wire configuration for NLSV measurement. The switches stand by the switch box.

All of the samples are made on 2 inch silicon wafers (substrates) with either SiO_x or SiN_x 200 nm coated on their surfaces, which have been polished. The thickness of the wafers is about 270 μm. Their resistivity is about $1\sim10\ \Omega\cdot cm$. The crystal orientation is typically in [100] direction. After performing the e-beam lithography at UMD, we cut the wafers into nine chips that were 1 cm × 1 cm each. After the deposition but before the measurement, the sample chip is put into a gold chip carrier, with GE Varnish (a very sticky glue that has a working temperature range

of 4K to room temperature) used to ensure that it sticks firmly. We used copper line, sharpened Q-tips, and hands-on work to finish wire-bonding the contact pads on the silicon chip to the contact pads on chip carrier, which are then placed onto a stage at the end of a positioner. The sample positioner is a long probe that is suspended within the sample tube (a pulse tube, which will be introduced in following section). Since each chip has four NLSVs and occupies four contact pads, there will be a total of 16 wires connected to a switch box with 16 BNC connectors. All of these can be connected to the measurement meters by BNC cables in correct wire configurations.

During the measurement process, the positioner is inserted into a pulse tube, which is isolated from the outside environment by a vacuum jacket. The vacuum inside of the vacuum jacket can be as strong as 10^{-5} Torr. [**Fig. 3.9]** This pulse tube is connected to a cold head, which is connected to a rotary valve and a compressor by flex lines. All of these constitute a cryogenic measurement system, something that will be explained in Section 3.4. The probe is loaded from the top of the pulse tube. The three-way valve that is installed there opens to pump in the high-purity helium gas, which pushes up the sealing cover at the top of the tube. The positioner probe can be inserted through the top, which is sealed by the cover attached to the positioner itself. Next, the valve is switched to a mechanical pump in order to pump out most of the gas (composed of helium and air residue) in the tube. After pumping in and out several times, the pulse tube will be full of helium and the valve will be closed. It is then safe to start taking measurements.

In a regular measurement, an AC current with an amplitude of 100 μA at 346.5 Hz (and sometimes other frequencies in the hundreds range) is applied through the injector by setting the Keithley 6221 Precision DC/AC Current Source into sine wave

mode (with a phase angle of 0 degrees). The frequency and phase of the applied AC current are locked to the SR830 lock-in amplifier. On the other side, the AC voltage is measured by the lock-in amplifier at an A-B mode. All four components, X, Y, R (which equals $\sqrt{X^2 + Y^2}$), and the phase angle, can be recorded and plotted out simultaneously by the LabVIEW program.

Lock-in amplifiers are used to detect and measure very small AC signals (as low as a few nanovolts). Lock-in amplifiers "lock" the frequency of the tested signals to a certain user-preset reference frequency (a narrow bandwidth) and rule out all other frequencies as noise. Because of this, the precision and accuracy of lock-in is generally very high. The "lock" and "filtered out" function is accomplished by an electronic element called the "phase-sensitive detector." It can multiply the input signal (which might have a wide bandwidth) with the lock-in amplifier internal reference frequency in order to suppress the effects of signals with frequencies that are out of the user-preset bandwidth. Since the signal from our sample is typically in the range of microvolts, it can be captured by lock-in easily when the quality of the sample is good. [8]

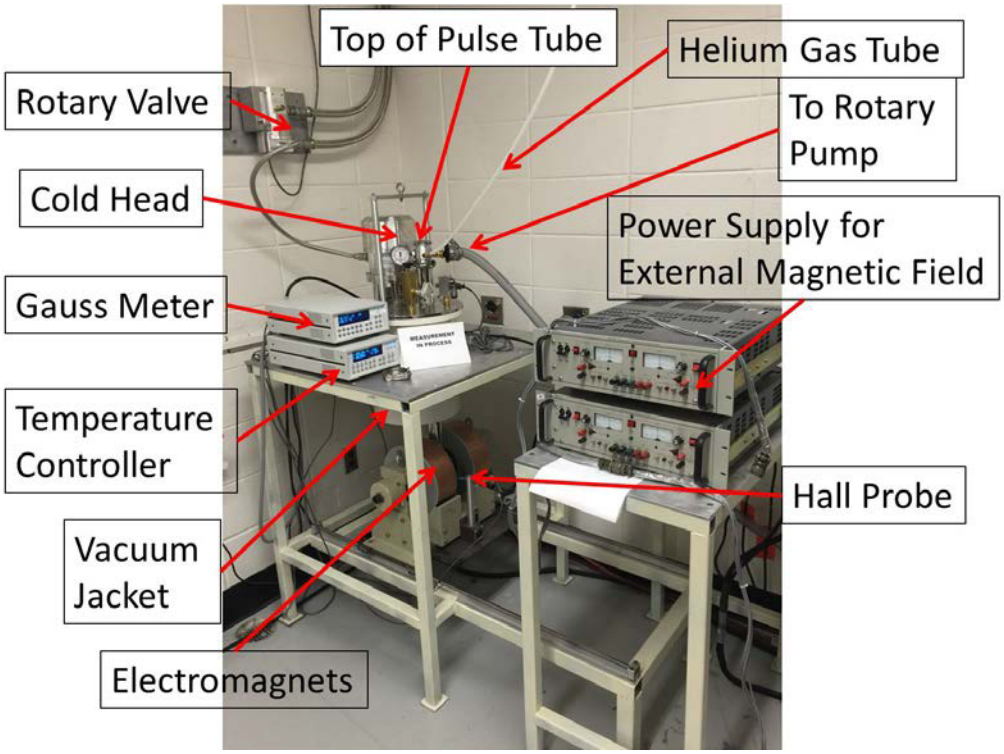

Figure 3.9: A picture for the measurement and cryogenic system in Ji's group.

The magnetic field was applied by two electromagnets made by GMW. The field is actually produced by two large coils with numerous rounds of wires wound around two separated electromagnets as shown in **Figure 3.10**, connecting to two Kepco power supplies. Each one of these can reach up to 20 V/20 A. Cooling water circulates inside of the coils to reduce the potential damage from overheating. Depending on the distance between the two coils, the maximum magnetic field can be adjusted from 0 ~ 1 Tesla. To accommodate our pulse tube size, however, we needed to separate the two coils by a certain distance so that the maximum magnetic field was about 0.5 T. According to the principle of the Helmholtz coil, and considering that our sample chip is very small when compared to the coils, we can assume that the field

applied on the sample chip is uniform and pointing from one pole to another. During the measurement process, we can control the field magnitude and direction by changing the current through LabVIEW. The magnitude and direction of the magnetic field is measured by a Hall probe connected to a Gauss meter Lakeshore 455.

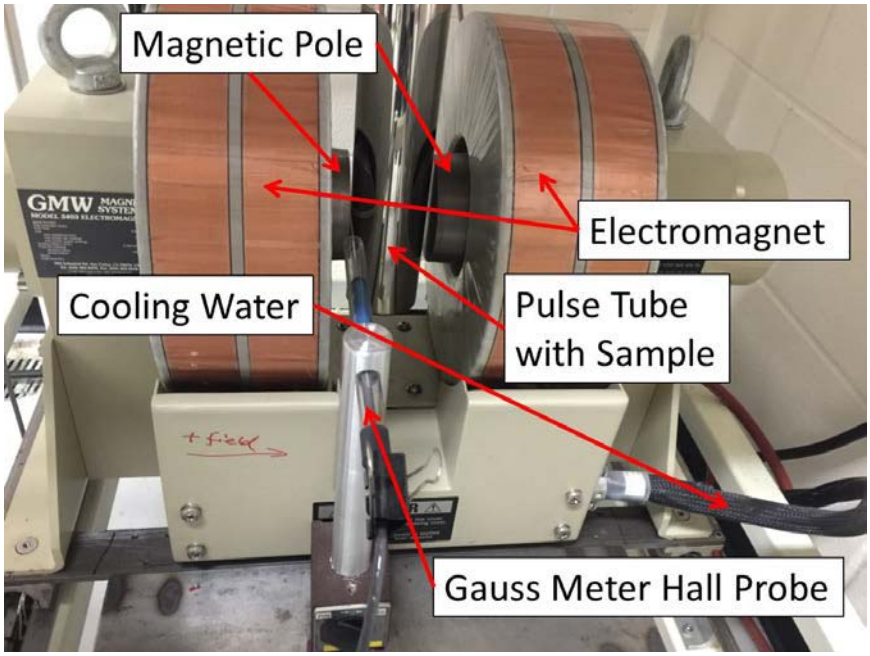

Figure 3.10: A picture showing the electromagnets in Ji's group.

3.4 Cryogenic system

The cryogenic system that was used in this work is the Janis Research PTSHI-950 Refrigerator System, with an operating temperature range of 4.3 K to room temperature. It is a cryogen-free cryostat system with a mechanical pulse tube cooler. The system, made by Sumitomo, consists of a compressor, a cold head, an exchange gas sample tube, a sample positioner, and an automatic temperature controller. [9]

The sample is mounted on a stage at the bottom of the probe. Sixteen pairs of twisted wires connect the stage to the switch box mentioned above. The helium exchange gas inside of the tube transfers heat from the sample to the refrigerator to cool it down. There are two sets of heaters and thermometers inside of the tube, corresponding to two methods of temperature monitoring and controlling. One set is located on the tube in order to vary the temperature of the exchange gas and control the sample temperature indirectly. The advantage of this method is that the temperature measurement is more uniform and accurate. Its disadvantage, however, is that the sample temperature takes longer to stabilize, especially at higher temperatures (>180K). The other heater and thermometer set is installed on the sample positioner (at the back of the chip carrier holder). The sample is directly heated by heat conduction (from a heater) through the Cu sample holder. The temperature control process of this method is fast, but there could be an error because the exchange gas surrounding the sample is at a different temperature, and the thermal contact between the sample and the holder might not be beneficial. The combination of these two methods gives rise to a precisely controlled sample temperature; the actual temperature should be between the other two values measured by those sensors. It takes about 8~10 hours for the temperature to reach 4.3 K. During measurement, the compressor starts to cool down by circulating the helium from the three-way valve throughout the system. As a result of the equilibrium of these two processes, the heater can be turned on and adjusted by the Lakeshore 322 temperature controller to keep the sample at the desired temperature. Lakeshore 322 is also controlled by LabVIEW, which collects and records the temperature for every data point.

REFERENCES

[1] http://en.wikipedia.org/wiki/Photolithography.

[2] http://en.wikipedia.org/wiki/Electron-beam_lithography.

[3] *Raith e-LiNE Software Operational Manual*, Version 4.0.

[4] *Raith e-LiNE Column Operation Manual*, Version 4.0.

[5] G. J. Dolan, Applied Physics Letters, **31**, 337(1977).

[6] http://en.wikipedia.org/wiki/Electron_beam_physical_vapor_deposition.

[7] http://www.vem-co.com/sites/default/files/pdfs/VEM_Thin_Film_Evaporation_Guide.pdf.

[8] *SR830 DSP Lock-In Amplifier User Manual*, Revision 2.3 (12/2006).

[9] Operating Instructions for the Janis Research PTSHI-950 Refrigerator System.

Chapter 4

ABSENCE OF HIGH SURFACE SPIN-FLIP RATE IN MESOSCOPIC SILVER CHANNELS

4.1 Introduction

The pursuit of a long spin diffusion length λ_{sf} in the nonmagnetic channel in nonlocal spin valve (NLSV) [1-3] is pivotal because the spin accumulation exponentially decays as a function of distance in the nonmagnetic channel, and λ_{sf} is the characteristic length scale of the decay. An increase of λ_{sf} could significantly increase the measured spin signals in a NLSV, which will reinforce the future application of spintronic devices. As we mentioned in Chapter 2, the interfacial spin injection/detection polarizations (*P*) are also crucial. In the past decade, the spin signals of mesoscopic NLSV devices with copper channels have increased from <1 to ~30 $m\Omega$ [3-9] due to enhanced λ_s of Cu and optimized *P* of Py/AlO_x or Py/MgO injection/detection interfaces.

A parallel theme of interest in NLSV is the non-monotonic temperature dependence of spin signals, which is related to the spin diffusion length λ_{sf}. This dependence has been observed in silver [10] and copper [8, 11, 12] channels and has been attributed to a high spin-flip rate near the surface of nonmagnetic channels. [8, 10, 11] Our previous work indicates that the origin of the high surface spin-flip rate is the magnetic impurities located near the side surfaces of the nonmagnetic channel. [8, 13, 14] Recently another study [15] suggests a different origin of Kondo effects, which are also interestingly attributed to magnetic impurities in the nonmagnetic channel.

Stimulated by the pursuit of large spin signals and the controversy over the origin of the non-monotonic temperature dependence of spin signals, we explore spin transport in NLSVs with silver channels. Large spin signals up to 38 $m\Omega$ have been achieved in as-deposited devices without any post-deposition annealing. Furthermore, the spin signals increase monotonically as the measurement temperature decreases from 295 to 4.5 K, in contrast to previous non-monotonic temperature dependence studies. We will show that the interesting morphology and growth mechanism of the silver channels affect the spin transport behaviors.

4.2 Fabrication of Silver Channel Based NLSVs

Four NLSV devices, labeled device #1 through #4, are fabricated on the same silicon substrate covered with SiN_x. A scanning electron microscope (SEM) image of device #2 is shown in Figure 4.1 (a). The device consists of an Ag channel, a Py (permalloy or NiFe alloy) spin injector, and a Py spin detector. A 2-nm-thick aluminum oxide (AlO_x) layer is placed between Py and Ag, forming Py/AlO_x/Ag injection/detection interfaces. The center-to-center distance between the injector and detector is defined as *L*. The values of *L*, measured by SEM, are 180, 275, 352, and 503 nm for devices #1 through #4, respectively, as shown in Table I. From Figure 4.1 (a), it is clear that the microstructures of the Ag channel are distinct from films formed in layer-by-layer growth mode, such as Cu. The Ag grains, which are 30–80 nm in size and rough due to the protruding grains, are visible under SEM.

The samples are fabricated through a shadow mask by angle evaporation. We still use e-beam evaporation of Py, AlO_x, and Ag from different angles through a suspended shadow mask to form the structures, as shown in Figure 4.1 (b). The nominal thickness values are 23-nm Py for the injector, 9-nm Py for the detector, 110-

nm Ag, and 2-nm AlO_x. The angle deposition technique allows the NLSV structures to be formed in one-cycle high vacuum with high quality Py/AlO_x/Ag interfaces. More details can be found at [5, 6].

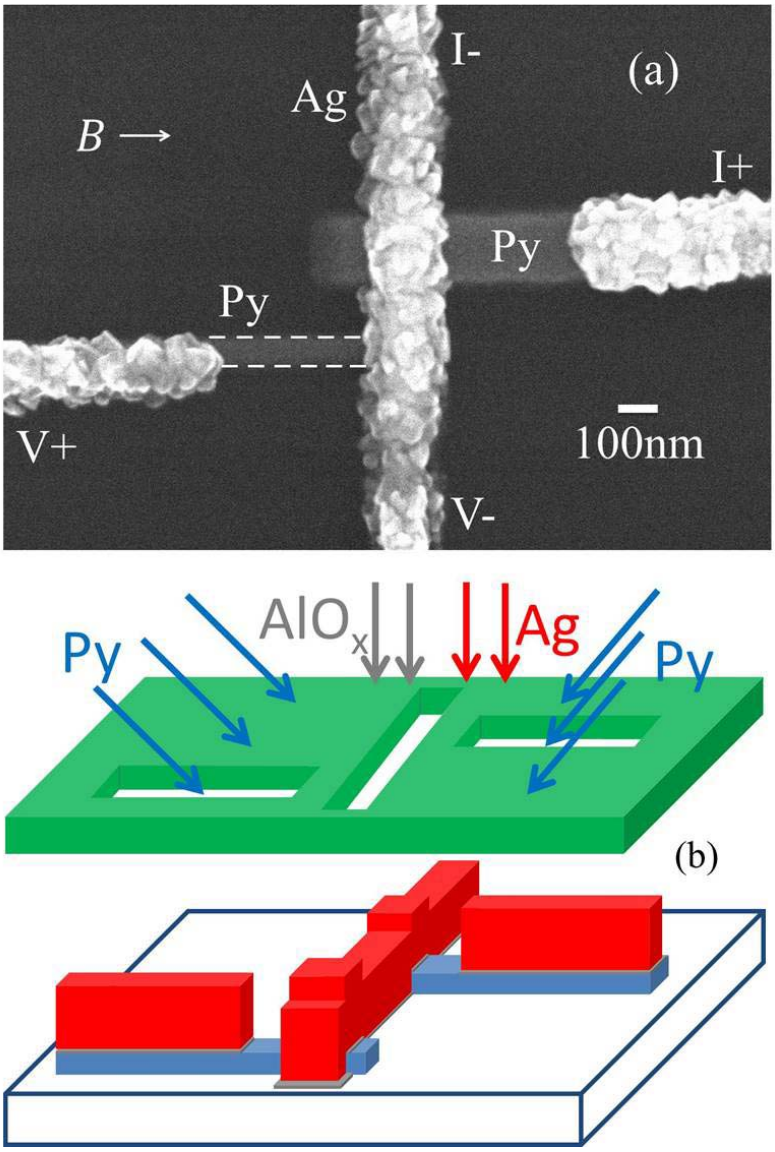

Figure 4.1: (a) SEM image of device #2. The Py spin detector is outlined using dashed lines to guide the eye. (b) Illustration of the angle deposition through a shadow mask made of PMMA/PMGI. (Copyright (2015) The Japan Society of Applied Physics)

We still use nonlocal measurement configuration for these samples. An alternating current (AC) *I* of 0.1 mA at 346.5 Hz is directed from the spin injector into the Ag channel. The nonlocal voltage V_s is detected by the lock-in method between the spin detector and the opposite end of the Ag channel. The nonlocal resistance $R_s = V_s/I$ is recorded as a function of the magnetic field *B*, which is applied parallel to the easy axis of the Py injector/detector. The R_s versus *B* curves for device #2 ($L = 275\ nm$) are shown in Figure 4.2 (a) for 4.5 K and Figure 4.2 (b) for 295 K. Both curves clearly show two-state switching between the parallel (*P*) states and antiparallel (*AP*) states of the injector and detector. The difference in the R_s values between two states is the spin signal ΔR_s. At 4.5 K, $R_s = 38\ m\Omega$, and at 295 K, $R_s = 12\ m\Omega$. These values are lower than those from annealed Py/MgO/Ag NLSV devices. [9] However, these values are clearly larger than those from previously reported un-annealed NLSV devices with Ag [16] or Cu [8, 17] channels.

The temperature dependence of the spin signal for all four devices is shown in Figure 4.2(c). There are two striking features by comparing to previous measurements. First, all spin signals ΔR_s increase monotonically as the temperature decreases. The previously observed unusual decrease of ΔR_s at temperature below ~50 K is absent. Second, the device with the smallest *L* (device #1, $L = 180\ nm$) did not yield the largest spin signal. At 4.5 K, device #1 shows $\Delta R_s = 31\ m\Omega$, which is smaller than the 38-$m\Omega$ spin signal of device #2 ($L = 275\ nm$). Two devices have the same spin signal of 12 $m\Omega$ at 295 K. Device #3 and Device #4 have essentially the same spin signals over the entire temperature range, while the values of *L* are 352 and 503 nm, respectively. In the following analysis, we will show that both features are related to the microstructures of the Ag channel.

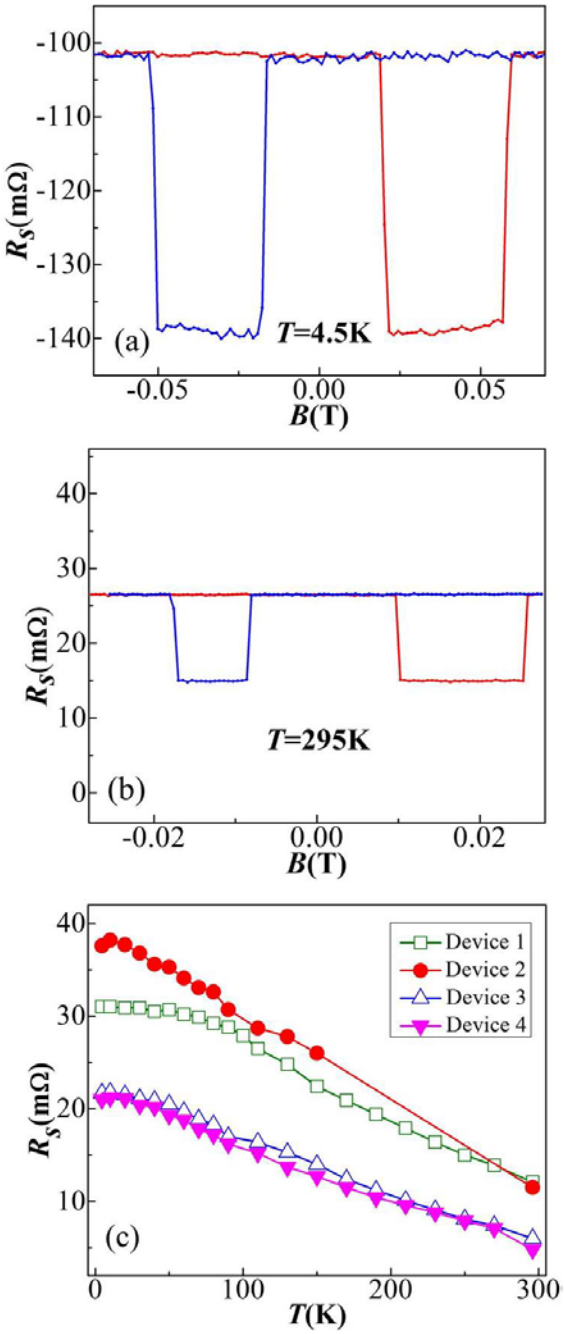

Figure 4.2: (a) The R_s versus B curve for device #2 at 4.5 K showing ΔR_s = 38 mΩ; (b) The R_s versus B curve for device #2 at 295 K showing ΔR_s = 12 mΩ; (c) The ΔR_s versus T for devices #1 through #4. (Copyright (2015) The Japan Society of Applied Physics)

4.3 Results Discussion

Here we would like to calculate the spin polarization and estimate the spin diffusion length first. The spin signals in NLSV with oxide injection/detection interfaces can be described by

$$\Delta R_S = (P_1 P_2 \rho \lambda_s / A) e^{-\frac{L}{\lambda_s}}$$

It is customary to fit ΔR_s as a function of L to extract P and λ_s with the assumption $P_1 = P_2 = P$. However, ΔR_s of the four devices apparently do not follow the exponential decay as a function of L, and thus, a straightforward fitting is not feasible. This behavior is more likely due to variations of spin diffusion length λ_{sf} from device to device. Our previous measured interfacial polarizations [8] with Py/AlO_x spin injectors/detectors indicate $P = 0.21$ at 4.5 K and $P = 0.14$ at 295 K. Using these values and $\rho = 1.9\ \mu\Omega \bullet cm$ at 4.5 K, $\rho = 4.0\ \mu\Omega \bullet cm$ at 295 K, (both measured in-situ from device #4) and $A = 140 \times 110\ nm^2$, the estimated values of λ_s are listed in Table I. The device-to-device variation of λ_s is substantial and is attributed to the irregular micro-structures of the Ag channel. For device #2, $\lambda_s = 920\ nm$ at 4.5 K and $\lambda_s = 440\ nm$ at 295 K are notably higher than the values from other devices.

We propose that the microstructures of the Ag channel, which are the results of Volmer–Weber growth and known as island growth, are highly relevant to the substantial spin signals. Volmer–Weber growth of Ag is common and has been documented in the literature. [18] Generally, island growth occurs when the atoms of the deposited material (Ag) are strongly bound to each other rather than to the substrate (SiO_x or SiN_x). Instead of adhering to the substrate and growing layer-by-layer, three-dimensional isolated islands nucleate on the substrate and grow in size as the deposition progresses until the islands coalesce. The growth process for the Ag

channel is illustrated in Figure 4.3, which shows cross-sectional views of the Ag channel during Ag evaporation. Initially, the Ag islands are isolated on the substrate as shown in Figure 4.3 (a). At a certain point [Figure 4.3(b)], coalescence of the islands takes place and a continuous Ag channel starts to form. Figure 4.3 (c) shows the further growth of the Ag channel and its lateral expansion in the direction of the width after coalescence. The expansion is due to the lack of lateral confinement along the width of the Ag channel. Because of the repulsion between islands, the Ag islands are not strongly bound to the substrate and move outward during the growth.

Table 4.1: Estimated spin diffusion lengths (nm) of the silver channels assuming P = 0.21 at 4.5 K and P = 0.14 at 295 K. (Copyright (2015) The Japan Society of Applied Physics)

	Device #1 L = 180 nm	Device #2 L = 275 nm	Device #3 L = 352 nm	Device #4 L = 503 nm
λ_s at 4.5 K	730 nm	930 nm	670 nm	750 nm
λ_s at 295 K	380 nm	430 nm	335 nm	370 nm

This expansion can be clearly seen from the SEM image in Figure 4.1 (a). It can be verified by comparing the width between Py and Ag strip as following. The edges of the Py detector are marked by dashed lines. On the left portion of the Py detector, an Ag wire section is placed on top of the Py detector as a result of shadow evaporation, and it is clearly wider than Py. As shown in Figure 4.1 (b), Ag and Py are evaporated from different angles through the same slot on the shadow mask. The two sections should have the same width, which is typically seen in Py–Cu NLSV structures. However, the measurement from SEM indicates the width of Py is ~90 nm, on the contrary to the width 170nm of Ag, indicating significant (80 nm) lateral

expansion. Therefore, it is reasonable to expect a similar expansion for the Ag channel. To maintain the same volume, the average thickness of Ag should be reduced due to the width expansion. When assuming an 80-nm expansion of the channel width, the cross-sections are $220 \times 70\ nm^2$ instead of $140 \times 110\ nm^2$ while maintaining the same cross-sectional area. In the following, we propose that the lateral expansion of Ag channel can influence the locations of magnetic impurities and therefore the spin flip rate/spin signal.

The previously observed unusual decrease of spin signal below 50 K has been attributed to a high surface spin-flip rate. [8, 10, 11] As the temperature decreases, the mean free paths of conduction electrons increase and become comparable to the width and/or thickness of the nonmagnetic channel. Then a large fraction of momentum scattering events occur at the surfaces. A higher spin-flip rate from the surfaces will lead to a reduction of spin relaxation time and λ_s. Our previous work indicates that the magnetic impurities embedded near the side surfaces of the nonmagnetic channel are culprits for high surface spin-flip rate. [8, 13, 14] During the deposition of Py from an oblique angle, as shown in Figure 4.1 (b), a substantial amount of Ni and Fe is accumulated on the side walls of the PMMA resist, as shown in Figure 4.3. When nonmagnetic metals such as Cu or Ag are evaporated along the normal direction to the substrate, Cu (Ag) atomic vapor passes through the mask with substantial momentum, and a small amount of Ni and Fe atoms can be knocked out and implanted into the Cu (Ag) channel. The Ni and Fe impurities are located near the side surfaces of the Cu channel and cause a high surface spin-flip rate, due to the layer-by-layer continuous growth mechanism of Cu channel. Over a period of months, the magnetic impurities are gradually segregated toward the Cu surfaces and are oxidized, leading to a

reduction of spin flip rate and an increase of spin signals. [8, 13] This is consistent with a related study, where NLSV structures with Cu channels fabricated by shadow evaporation with thin magnetic injector/detectors show longer spin diffusion length than structures with thicker injector/detectors. [14]

Now comes back to devices with Ag channels, the Ni and Fe impurities are more likely to be located in the bulk due to the motion of Ag islands on the substrate during the expansion. It is well-known that impurities tend to segregate to surfaces and grain boundaries. [19] We hypothesize that the Ni and Fe impurities are embedded in the bulk of the Ag channel and then segregated into the grain boundaries to reduce the free energy. In this scenario, the surface spin-flip rate is not particularly higher than bulk spin-flip rate. Therefore, we see a monotonic increase of ΔR_s as the temperature decreases in Figure 4.2 (c). In the Ag bulk, the bulk momentum scattering of electrons comes from phonons, impurities, and defects including grain boundaries. If the impurities are largely located at grain boundaries, the momentum scattering rate is not necessarily increased for the Ag channel although the grain boundaries are defects and induce momentum scattering. The reason is that since the size of the grains is large, the chance of bulk scattering for conduction electrons decreases. As a result, the spin-flip rate at the grain boundaries may not increase so much due to the presence of magnetic impurities, which may not reduce the spin diffusion length and degrade other magnetic properties as that in Cu channel.

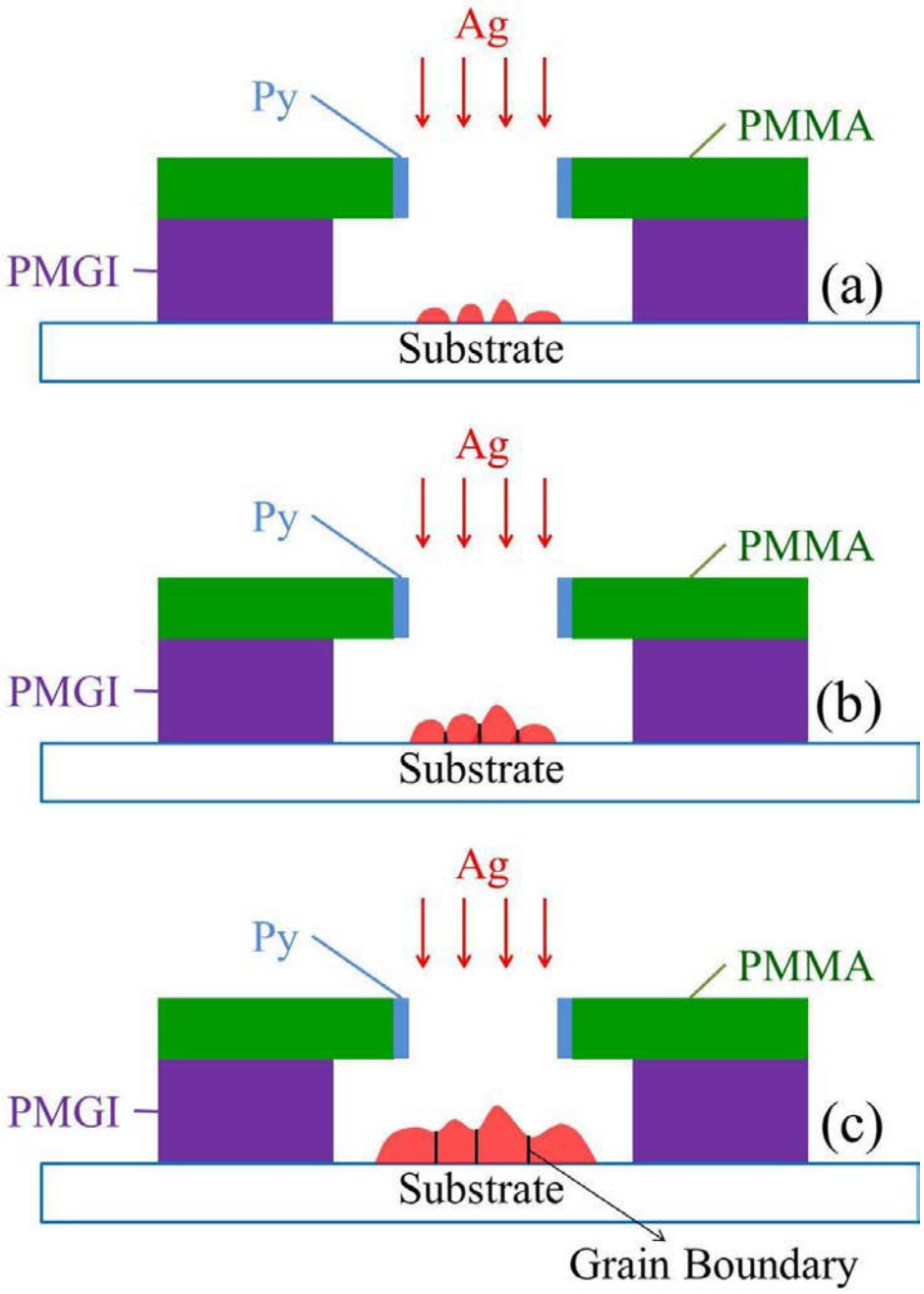

Figure 4.3: Cross-sectional views of the Ag channel during evaporation through the PMMA/PMGI shadow mask. (a) Initial stage of growth with isolated Ag islands; (b) coalescence of the Ag islands; (c) lateral expansion of the Ag channel on the substrate after coalescence. (Copyright (2015) The Japan Society of Applied Physics)

4.4 Conclusion

In a summary, we have demonstrated large spin signals at both room and extremely low temperature in nonlocal spin valves with silver channels without post-annealing. The spin signals monotonically increase as the temperature decreases, different from the previously observed non-monotonic dependence with a peak value of ~50 K due to high surface spin-flip rate that comes from magnetic impurities near the surfaces of the nonmagnetic (Cu or Ag) channels. SEM images indicate that the silver grows in Volmer–Weber mode with coalesced islands. The magnetic impurities are implanted into the bulk of the silver and segregated into the grain boundaries due to the lateral expansion of the silver channel during growth. Therefore, there is no overall increase of the surface spin-flip rate and the temperature dependence is monotonic. This research enriches the understanding of spin transport in nanostructure and spintronic device.

This work has been published on Applied Physics Express. [20]

REFERENCES

[1] M. Johnson and R. H. Silsbee, Physical Review Letters, **55**, 1790 (1985).

[2] F. J. Jedema, H. B. Heersche, A. T. Filip, *et al*., Nature, **416**, 6882 (2002).

[3] F. J. Jedema, A. T. Filip, and B. J. van Wees, Nature, **410**, 6826 (2001).

[4] T. Kimura, J. Hamrle, Y. Otani, *et al*., Applied Physics Letters, **85**, 3501 (2004).

[5] Y. Ji, A. Hoffmann, J. E. Pearson, and S. D. Bader, Applied Physics Letters, **88**, 052509 (2006).

[6] X. J. Wang, H. Zou, L.E. Ocola, and Y. Ji, Applied Physics Letters, **95**, 022519 (2009).

[7] H. Zou and Y. Ji, Journal of Magnetism and Magnetic Materials, **323**, 2448 (2011).

[8] H. Zou and Y. Ji, Applied Physics Letters, **101**, 082401 (2012).

[9] Y. Fukuma, L. Wang, H. Idzuchi, *et al*., Nature Materials, **10**, 527 (2011).

[10] G. Mihajlovic, J. E. Pearson, S. D. Bader, and A. Hoffmann, Physical Review Letters, **104**, 237202 (2010).

[11] T. Kimura, T. Sato, and Y. Otani, Physical Review Letters, **100**, 066602 (2008).

[12] E. Villamor, M. Isasa, L. E. Hueso, and F. Casanova, Physical Review B, **87**, 094417 (2013).

[13] X. J. Wang, H. Zou, and Y. Ji, Journal of Magnetism and Magnetic Materials, **322**, 3572 (2010).

[14] H. Zou, X. J. Wang, and Y. Ji, Journal of Vacuum Science and Technology B, **28**, 1314 (2010).

[15] L. O'Brien, M. J. Erickson, D. Spivak, *et al*., Nature Communications, **5**, 3927 (2014).

[16] Y. Fukuma, L. Wang, H. Idzuchi, and Y. Otani, Applied Physics Letters, **97**, 012507 (2010).

[17] T. Wakamura, K. Ohnishi, Y. Niimi, and Y. Otani, Applied Physics Express, **4**, 063002 (2011).

[18] C. Polop, C. Rosiepen, S. Bleikamp, *et al*., New Journal of Physics, **9**, 74 (2007).

[19] D. McLean, *Grain Boundaries in Metals*, 1957: Oxford University Press, London.

[20] S. Chen, H. Zou, C. Qin, and Y. Ji, Applied Physics Express, **7**, 11 (2014).

Chapter 5

ASYMMETRIC SPIN ABSORPTION ACROSS A LOW-RESISTANCE OXIDE BARRIER

5.1 Introduction

The physical origin of the nonlocal spin signal [1-6] can be viewed as a spin absorption process. A fraction of the pure spin current in the non-magnetic channel is absorbed into the F_2 across the N/F_2 interface. It decays into the bulk of F_2 on the scale of the spin diffusion length of F_2. An electric potential difference (*i.e.* the nonlocal voltage) is created between F_2 and N owing to the conductivity difference between the spin-up and spin-down electrons. This potential difference, equivalent to an electromotive force (emf), changes sign when the relative alignment between the F_2 magnetization and the spin accumulation in the N channel switches between parallel and antiparallel states. The amount of the absorbed spin current depends on the spin resistance values of the F_2, the interface, and the N channel. [7]

Here we explore an unconventional approach for nonlocal spin detection by probing the nonlocal voltage between the two ends of the ferromagnetic spin detector F_2, instead of the nonlocal voltage between the F_2 and the N channel. Clear nonlocal signals are detected at room temperature and attributed to a spatially non-uniform spin absorption process across the low-resistance oxide interface. Similar signals are observed and can be explained by a reciprocal process of asymmetric spin injection when the current injection terminals and voltage detection terminals are switched. This method provides an alternative way of probing nonlocal spin accumulation, and offers

flexibility in designing lateral spin transport structures. In addition, since the voltage detection terminals do not involve the N channel, the N channel can be terminated near the spin detector F_2 and thereby enhancing the spin accumulation by a factor of 2.

Previous works by Torres *et al.* [8] and Kimura *et al.* [9] reported nonlocal spin detection using a similar measurement configuration. Torres *et al.* utilizes a trapped domain wall in the spin detector underneath the Cu channel to inject a spin current. Kimura *et al.* measures the voltage across an extended spin detector underneath a wide Cu channel. As a comparison, our structures do not require a trapped domain wall or a wider-than-usual Cu channel and are therefore easier to fabricate and more flexible to use.

5.2 Fabrication of Unconventional Samples

Figure 5.1 (a) shows a scanning electron microscope picture for our unconventional NLSV structure. The ferromagnetic spin injector F_1 and spin detector F_2 are made of Py and the N channel is made of Cu. The F_1 and F_2 electrodes are outlined by dash for clarity. The F_1 and F_2 electrodes are 250 nm and 150 nm in widths, respectively, and both are 10 nm in thickness. The Cu channel is ~ 150 nm wide and 110 nm thick. There is a nominally 3 nm thick AlO_x layer between F_1 (or F_2) and Cu channel. The center-to-center distance between F_1 and F_2 is about 500 nm. Two types of devices with different overlap sizes between Cu and the F_2 electrode are intentionally made. In the “small-overlap” structures, as shown in Figure 5.2 (a), the lower tip of the Cu channel covers ~ 50 nm of the F_2 width. In the “full-overlap” structures, as shown in Figure 5.2 (b), the lower end of the Cu channel covers the full width (150 nm) of F_2.

The device is fabricated by angle evaporation through a double-layer resist shadow mask as illustrated in Figure 5.1 (b). As a result the Py/AlO_x/Cu interfaces are formed without breaking vacuum and pristine interfacial condition is maintained for spin transport. More details about fabrication are described elsewhere. [10-12] The Py/AlO_x/Cu interface has been shown previously to mitigate the spin resistance mismatch between Py and Cu and provide more substantial injection and detection spin polarizations in NLSV than those without oxide barrier. [11, 13-15] The spin signals in Py/AlO_x/Cu NLSV structures reach > 20 mΩ at 5 K and ~ 8 mΩ at 295 K, [14] which are substantially higher than those from NLSV structures with ohmic Py/Cu interfaces. [16-18] Note that the resistance of the AlO_x is still much lower than that of typical oxide tunnel junctions. The resistance-area (RA) product of our Py/AlO_x/Cu junctions has been estimated to be $0.005\ \Omega\bullet\mu m^2 < RA < 0.05\ \Omega\bullet\mu m^2$ by using four probe method on a cross-junction with four terminals. Previously large spin signals in MgO barriers based NLSVs with comparably low *RA* have also been reported. [19] The resistivity of mesoscopic Py stripes with 200 nm width and 12 nm thickness has also been measured to be $\rho = 324\ \mu\Omega\bullet cm$, a factor of ~ 10 larger than that of extended films. The larger resistivity value is likely due to the reduced lateral dimension. The values of interfacial resistance and Py resistivity are important in understanding the measurement results described in Section 5.3.

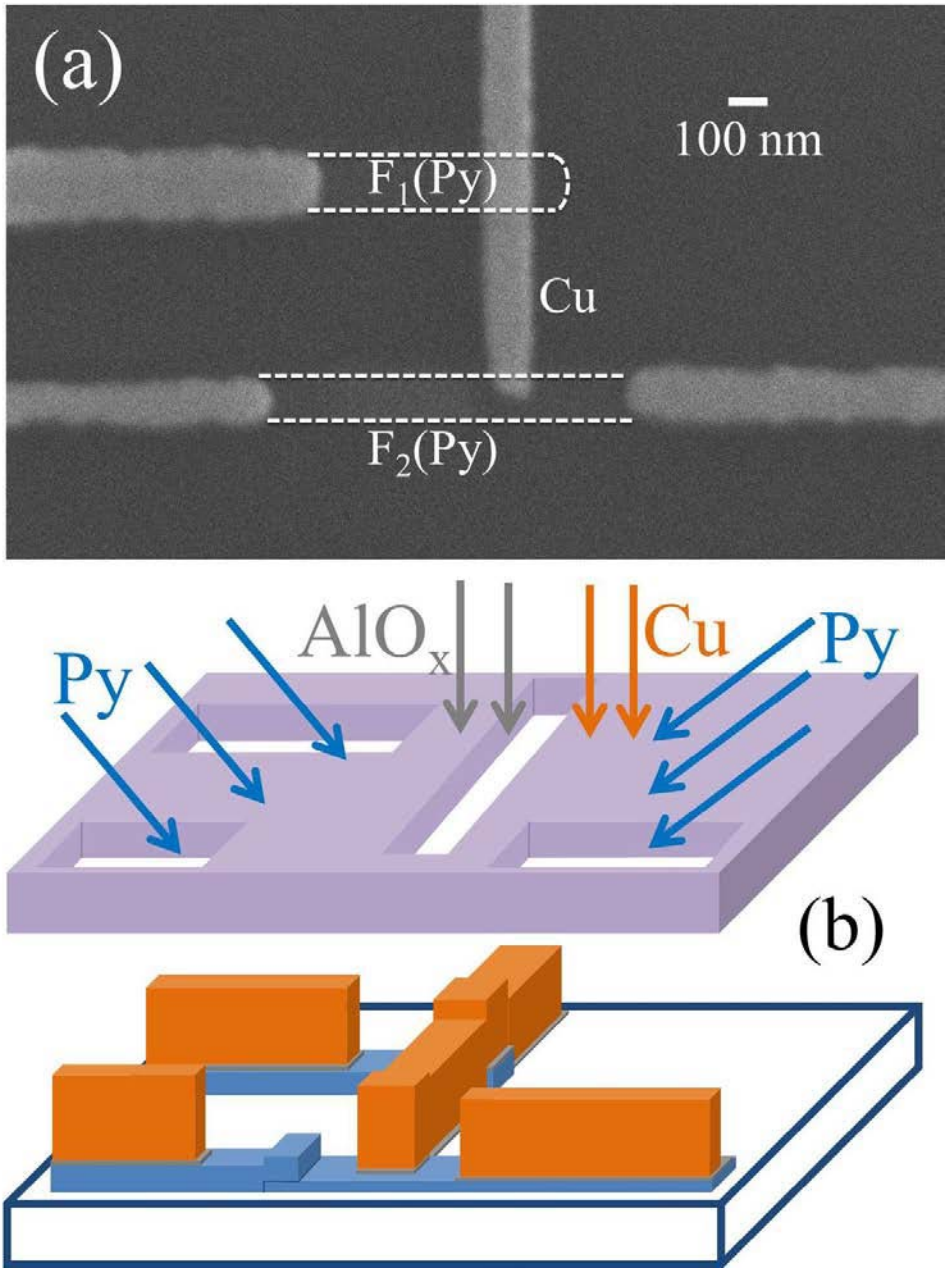

Figure 5.1: (a) SEM picture for our NLSV device. (b) Angle evaporation through a suspended resist mask.

5.3 Measurement and Discussion

5.3.1 Measurement Results

Figure 5.2 (a) and (b) illustrate primary measurement configuration, in which an injection current is directed between F_1 and the upper end of the Cu channel and the nonlocal voltage is detected between the two ends of the extended F_2 electrode. This differs from the standard nonlocal detection, in which the voltage is measured between F_2 and the Cu channel. An alternating current (*a.c.*) of I_e = 0.1 mA with a frequency < 1000 Hz is used and the nonlocal *a.c.* voltage V_{nl} is detected by a lock-in amplifier. The nonlocal resistance, $R_s = V_{nl}/I_e$, is recorded as a function of the magnetic field *B* which is applied parallel to the Py electrodes.

Clear nonlocal signals at room temperature have been observed in both the small-overlap structure (Figure 5.2 (a)) and full-overlap structure (Figure 5.2(b)) but the features are different. For the small-overlap structure, shown in Figure 5.2 (c), the R_s values switch between two states: a low-value state at high magnetic fields (parallel state for two FM electrodes) and a high-value state at intermediate fields (anti-parallel state of two FMs). The difference ΔR_s between two states is 0.25 mΩ for the forward branch (field ramping up) and 0.5 mΩ for the backward branch (field ramping down). These values are well reproducible in repeated measurements. The difference might result from the proximity of the two switching fields. The state with high R_s value may not be well developed in the forward branch due to a less perfect antiparallel state between F_1 and F_2.

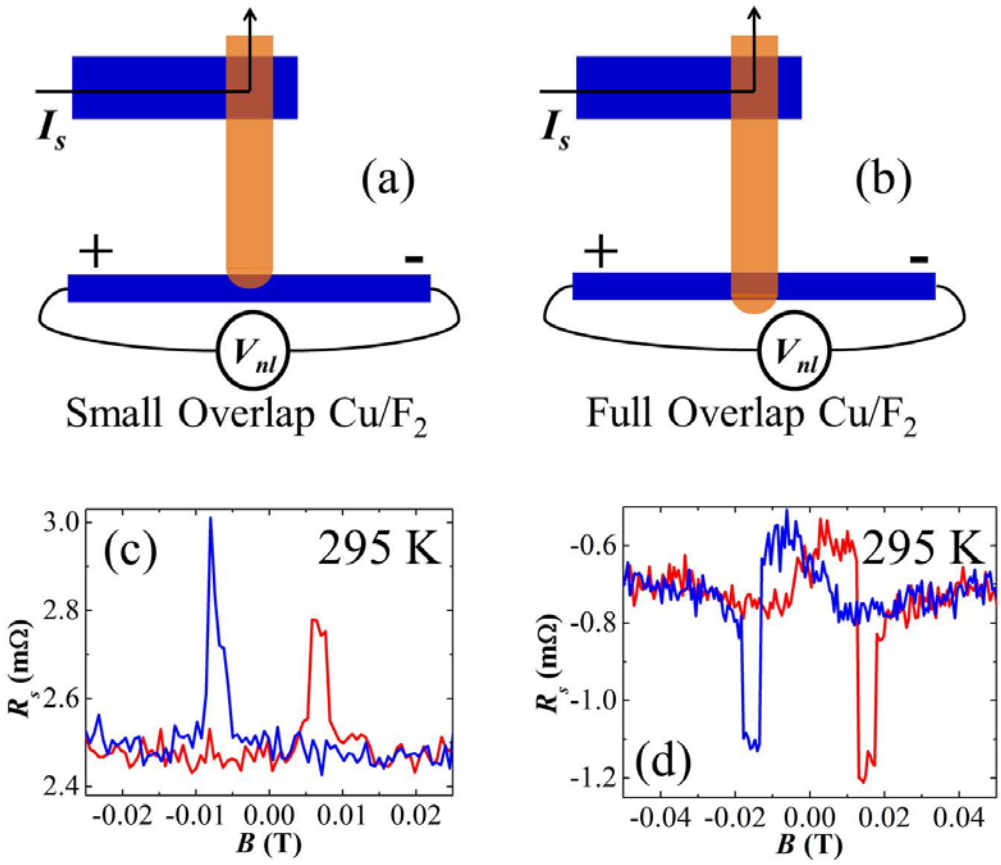

Figure 5.2: Cartoon illustrations of (a) the "small-overlap" structure and (b) the "full-overlap" structure and the measurement configuration. Plot of the R_s versus B curves for the (c) small-overlap structure and the (d) full-overlap structure.

For the full-overlap structure in Figure 5.2 (d), the R_s values switch between three different states. The difference of R_s values between the highest state and the lowest state is ~ 0.6 mΩ. The intermediate state is 0.2 mΩ below the highest state. As a comparison, the spin signals from our regular Py/AlO_x/Cu NLSV structures with an injector-to-detector distance of 500 nm are typically in the range of 1 – 3 mΩ at 295 K. [15, 20] For both the small-overlap and full-overlap structures, the baseline value of the R_s is low and the percentage changes of the signals are substantial, affirming the

nonlocal nature of the measurements. However, from the standard understanding of nonlocal spin valves, signals in the R_s versus B curves are not expected since the nonlocal voltage is measured on the F_2 spin detector alone, should not be measured across a single metallic F_2 electrode.

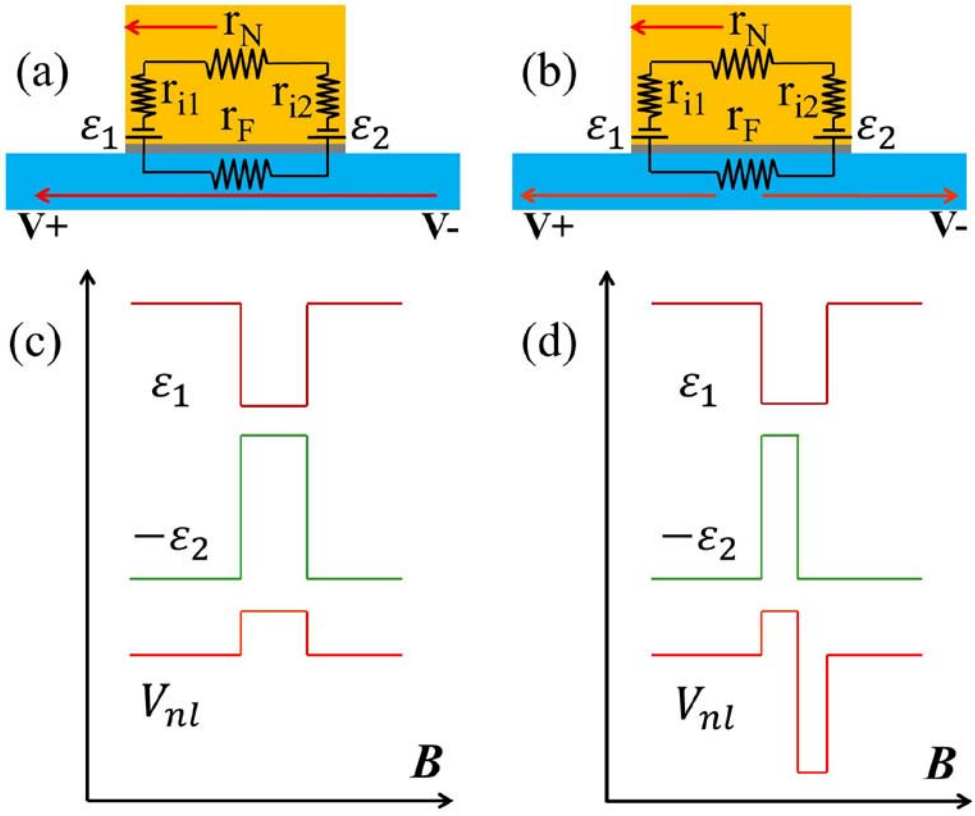

Figure 5.3: (a) A simple model which illustrates the asymmetric spin absorption across the $Cu/AlO_x/F_2$ interface. For the small-overlap structure, the magnetization under the interface behaves as a single domain. (b) For the full-overlap structure, it is possible that the two sections of the junction have different reversal fields and therefore a domain wall can be trapped underneath the junction between two reversal fields. The constructed curves of ε_1, $-\varepsilon_2$, and $V_{nl} \propto (\varepsilon_1 - \varepsilon_2)$ as functions of magnetic field B for (c) the small-overlap structure and (d) the full-overlap structure.

5.3.2 Asymmetric Spin Absorption

We believe that the unexpected signals in the R_s versus B curves can be understood by assuming spatially non-uniform absorption of spin current into the F_2 across the low-resistance AlO_x barrier. Figure 5.3 (a) and (b) illustrate the cross section views of Cu/AlO_x/F_2 interface, for the small-overlap and full-overlap, respectively. We consider the junction as being made up of two sections, one on the left side and the other on the right side, as a simplistic representation of the spatially non-uniform spin absorption at the interface. The spin absorption through the left section and the right section generates nonlocal voltages ε_1 and ε_2, respectively. The values of ε_1 and ε_2 should be presumably different owing to the spatially non-uniform spin absorption across the AlO_x barrier. Each section of the interface also contributes a resistance, r_{i1} and r_{i2}. The resistance of the Cu channel and the Py electrode (F_2) are r_N and r_F, respectively. Therefore a closed loop circuit is formed involving ε_1, ε_2, r_{i1}, r_{i2}, r_F, and r_N, as shown in Figure 5.3 (a) and (b).

The nonlocal voltage V_{nl} between two ends of F_2 is the voltage on r_F and can be expressed by a simple formula based on the voltage divider rule:

$$V_{nl} = \frac{r_F}{r_F + r_{i1} + r_{i2} + r_N}(\varepsilon_1 - \varepsilon_2). \qquad (1)$$

To capture nontrivial signals in the R_s versus B curve, two conditions have to be satisfied. First, the magnitude of r_F should not be much smaller than $r_{i1} + r_{i2} + r_N$, otherwise the V_{nl} becomes negligibly small. In our samples, this is satisfied because the AlO_x interfacial resistance is low and the Py resistivity is high. It is estimated that $r_{i1} \sim r_{i1} \sim$ 1-10 Ω based on the RA measurement of AlO_x junctions. The resistance of Py under the junction is estimated to be $r_F \sim 300$ Ω, based on the measured Py resistivity. The value of r_N is negligibly small due to the high Cu conductivity. Therefore the value of $\frac{r_F}{r_F + r_{i1} + r_{i2} + r_N}$ is close to 1. The second condition requires that

certain asymmetry exist between ε_1 and ε_2 in order to achieve signals in R_s versus B. Otherwise, if ε_1 and ε_2 share the same value and the same switching fields, $(\varepsilon_1 - \varepsilon_2) = 0$ is always true and no feature should be expected in the R_s versus B curve. In conclusion, either the magnitudes have to be different: $\varepsilon_1 \neq \varepsilon_2$, or the switching fields of ε_1, ε_2 have to be different.

Based on this simple model, we try to reconstruct the R_s versus B curves and compare to the experiments. Figure 5.3 (a) and (c) illustrates the situation for the small-overlap structure in which the magnitudes of emf voltages are different $\varepsilon_1 \neq \varepsilon_2$ but the switching fields are the same for the left section and right section of F_2. It is reasonable to assume there is a single domain trapped underneath the Cu tip. In other words, the switching field will be the same for the left and right sections. Figure 5.3 (c) shows the ε_1, $-\varepsilon_2$, and the superposition $V_{nl} \propto (\varepsilon_1 - \varepsilon_2)$, as functions of the magnetic field B. The field is ramped toward the positive B axis and therefore the curves evolve from the left to the right in Figure 5.3 (c). There are two switching fields for ε_1 (or ε_2) as the field is ramped up. The first one is associated with the reversal of the spin accumulation in Cu and thereby the magnetization reversal of the spin injector F_1. This switching field should be the same for ε_1 and ε_2, because both sections of interface are in contact with the same spin accumulation in Cu.

The second switching field is associated with the reversal of magnetization of the left section (for ε_1) or the right section (for ε_2) of the F_2 underneath the junction. Here we simply assume that the two sections of the interface switch at the same field again based on the single domain structure assumption. It is also assumed that $|\varepsilon_1| < |\varepsilon_2|$, and therefore nontrivial signals arise in $V_{nl} \propto (\varepsilon_1 - \varepsilon_2)$ versus B, shown at the bottom of Figure 5.3 (c). The constructed reversal spin voltage V_{nl} versus B curve

is qualitatively the same as the R_s versus B curve for the small-overlap structure shown in Figure 5.2 (c).

Figure 5.3 (b) and (d) illustrates the situation for the full-overlap structure in which the F_2 switching fields are different for ε_1 and ε_2 in addition to the difference in the magnitudes of ε_1 and ε_2. Suppose right section (ε_2) switches first and then the left section (ε_1) switches as the B field is ramped toward positive axis. Between these two events, it is reasonable to assume a domain wall is trapped underneath the junction as shown in Figure 5.3 (b). The constructed curves of ε_1, $-\varepsilon_2$, and the superposition $V_{nl} \propto (\varepsilon_1 - \varepsilon_2)$ versus B are shown in Figure 5.3(d). The first switching fields are still the same for ε_1 and ε_2 because it is associated with the reversal of F_1. The second reversal field of ε_2 is lower than that of ε_1. As a result, the superposition exhibits three states for V_{nl} values. This is consistent with the experimental R_s versus B curve for the full-overlap structure as shown in Figure 5.2 (d).

Therefore the main difference between the small-overlap structure and the full-overlap structure results from the switching behavior of the F_2 near the $Cu/AlO_x/F_2$ junction. It is reasonable that a larger junction has a higher chance to form domains and develop separate reversal fields in different sections. While in a smaller junction, it is very likely that the magnetization underneath the entire junction switches at the same field. The origin of asymmetric spin absorption, which gives rise to different values of ε_1 and ε_2, is attributed to the non-uniformity of the AlO_x layer. The AlO_x layer is formed by direct electron beam evaporation from AlO_x pellets without post-annealing. The roughness of the oxide layer is substantial and pin holes through the layer are highly possible existing. The current voltage (I-V) curve of the interface is nearly linear and the resistance of the interface is low (0.5 - 5 Ω).

We also consider the side contact effect to the charge/spin transport between the edge of the Py film (F_2) and the Cu channel. This region (150×7 nm^2) is not covered by AlO_x and could be potentially conductive. However, we found that the interface resistance values for the small-overlap structures are substantially larger than those for the full-overlap structures, though the areas of side contact regions are approximately the same for these two types. Therefore the electrical conductions are predominantly through the non-uniform AlO_x layers instead of the side contacts. In addition, spin transfer switching of a magnetic domain in F_2 has been realized in Py/AlO_x/Cu NLSV structures. [13, 15] This would not be possible if the absorbed spin current flows primarily through the side contact.

The switching between three R_s states for the full-overlap structure in Figure 5.2 (d) and Figure 5.3(d) relies on a domain wall underneath the contact. Artificially engineered structures can be used to ensure the trapping of a domain wall. Torres *et al.* [8] used a patterned notch in the spin detector to trap a domain wall. The difference between the experiments of Torres *et al.* and ours is that presumably $\varepsilon_1 = \varepsilon_2$ for Torres *et al.* while $\varepsilon_1 \neq \varepsilon_2$ for this work. Therefore Torres *et al.* observed switching between two states while we observed switching between three states in the full-overlap structure. We also need to point out that the asymmetry ($\varepsilon_1 \neq \varepsilon_2$) gives rise to a clear spin signal without a trapped domain wall in the small-overlap structure as shown in Figure 5.2 (c) and Figure 5.3 (c). Therefore our structures are more universal in detecting spin accumulation using this unconventional configuration.

5.3.3 Reciprocal Measurements for Asymmetric Spin Injection

The reciprocal measurements are performed on both structures by exchanging the current terminals and the voltage terminals, as shown in Figure 5.4 (a). The results

are summarized in Figure 5.4 (c) and (d) for the small-overlap and full-overlap structures, respectively. Although the noise is higher than that of the primary measurements, the essential features and magnitudes in the reciprocal measurements are quite similar to those in the primary measurements. The R_s values switch between two states for the small-overlap structure and three states for the full-overlap structure.

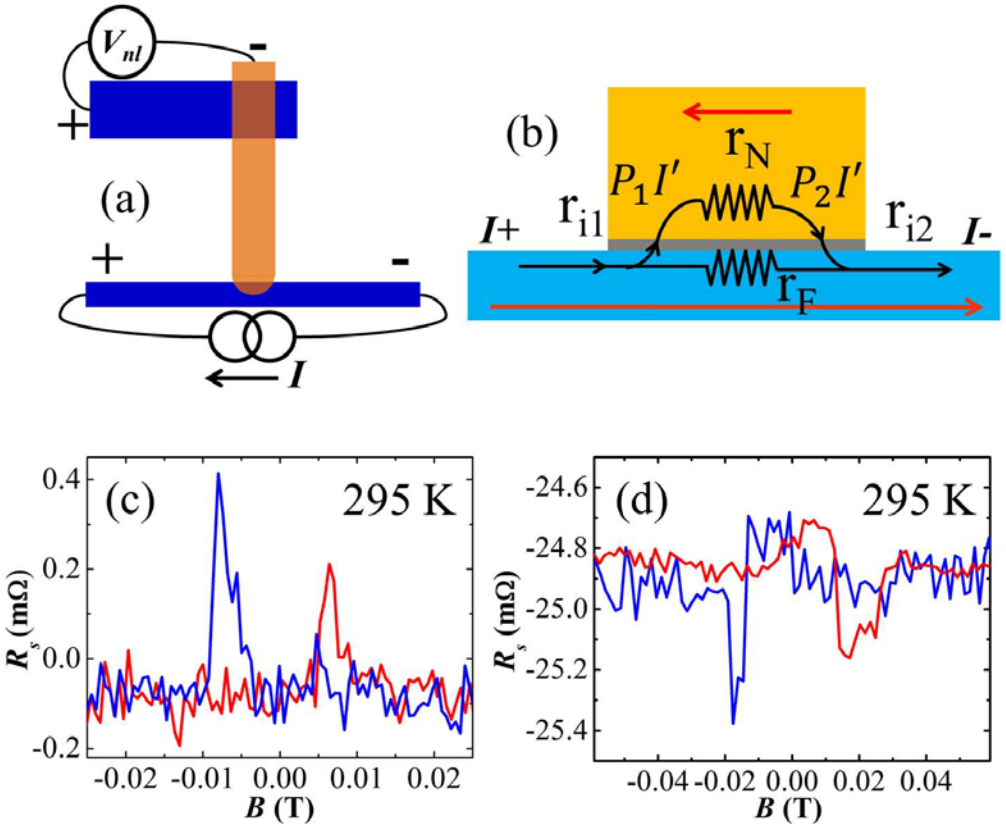

Figure 5.4: (a) The probe configuration of the reciprocal measurement. (b) A simple model that takes into account of the shunting effect of the Cu channel and the asymmetric spin injection. Plot of R_s versus B curve in the reciprocal measurement for (c) the small-overlap structure and (d) the full-overlap structure.

The reciprocal measurements can be understood as an asymmetric spin injection process, as shown in Figure 5.4 (b). Considering the non-uniform, low resistance of the AlO_x interface and the large Py resistivity, a large portion of the charge current will be shunted by the Cu. The shunted current passes through the left section of the interface first, then through the Cu, and eventually flows out of the right section of the interface. The spin current I_s carried into the Cu channel can be described by:

$$I_s = \frac{r_F}{r_F + r_{i1} + r_{i2} + r_N} I_e (P_1 - P_2). \qquad (2)$$

The factor $(\frac{r_F}{r_F + r_{i1} + r_{i2} + r_N})$ indicates the fraction of injection current being shunted by the Cu. The value of P_1 (P_2) is the effective spin polarization of the left section (right section) of the junction. Owing to the spatial non-uniformity of the AlO_x layer, the values of P_1 and P_2 are not necessarily the same. Eq 2 is quite similar to Eq 1. The only difference is that $I_e P_1$ and $I_e P_2$ replaces ε_1 and ε_2, respectively. The sign of the polarization P_1 (P_2) changes when magnetization of the left section (right section) of the F_2 electrode switches, in a way similar to ε_1 and ε_2. Therefore it is natural to expect similar outcomes in the measurements.

5.4 Conclusion

A nonconventional method of nonlocal spin detection is demonstrated in lateral spin valves at room temperature. The nonlocal voltage is detected between two ends of an extended ferromagnetic spin detector. The clear nonlocal signals can be understood by a simple effective circuit model near the interface, taking into account the spatially non-uniform spin absorption process across the interface. Similar results are achieved and can be understood as an asymmetric spin injection across the low-resistance oxide interface in the reciprocal measurements. This method provides an

alternative way for nonlocal spin detection with simplified geometry and enhanced spin accumulation.

REFERENCES

[1] M. Johnson and R. H. Silsbee, Physical Review Letters, **55**, 1790 (1985).

[2] F. J. Jedema, A. T. Filip and B. J. van Wees, Nature, **410**, 345 (2001).

[3] F. J. Jedema, H. B. Heersche, A. T. Filip, *et al*., Nature, **416**, 713 (2002).

[4] T. Kimura, J. Hamrle, Y. Otani, *et al*., Applied Physics Letters, **85**, 3501 (2004).

[5] S. O. Valenzuela and M. Tinkham, Applied Physics Letters, **85**, 5914 (2004).

[6] Y. Ji, A. Hoffmann, J. S. Jiang and S. D. Bader, Applied Physics Letters, **85**, 6218 (2004).

[7] T. Kimura, J. Hamrle and Y. Otani, Physical Review B, **72**, 014461 (2005).

[8] W. S. Torres, P. Laczkowski, V. D. Nguyen, *et al*, Nano Letter, **14**, 4016 (2014).

[9] T. Kimura, J. Hamrle and Y. Otani, Journal of Applied Physics, **97**, 076102 (2005).

[10] Y. Ji, A. Hoffmann, J. E. Pearson and S. D. Bader, Applied Physics Letters, **88**, 052509 (2006).

[11] X. J. Wang, H. Zou, L. E. Ocola and Y. Ji, Applied Physics Letters, **95**, 022519 (2009).

[12] H. Zou, X. J. Wang and Y. Ji, Journal of Vacuum Science and Technology B, **28**, 1314 (2010).

[13] H. Zou and Y. Ji, Journal of Magnetism and Magnetic Materials, **323**, 2448 (2011).

[14] H. Zou and Y. Ji, Applied Physics Letters, **101**, 082401 (2012).

[15] H. Zou, S. H. Chen and Y. Ji, Applied Physics Letters, **100**, 012404 (2012).

[16] T. Kimura, T. Sato and Y. Otani, Physical Review Letters, **100**, 066602 (2008).

[17] E. Villamor, M. Isasa, L. E. Hueso and F. Casanova, Physical Review B, **87**, 094417 (2013).

[18] O'Brien, M. J. Erickson, D. Spivak, *et al*, Nature Communications, **5**, 3927 (2014).

[19] Y. Fukuma, L. Wang, H. Idzuchi, *et al*, Nature Materials, **10**, 527 (2011).

[20] S. H. Chen, C. Qin and Y. Ji, Applied Physical Letters, **105**, 082402 (2014).

Chapter 6

LARGE SPIN ACCUMULATION NEAR A RESISTIVE INTERFACE DUE TO SPIN-CHARGE COUPLING

6.1 Introduction

Spin and charge are inherently coupled in the field of spintronics since both are intrinsic properties of electrons. [1, 2] This enables rich physics involving both charge currents and spin currents, such as spin transfer torque, [3] spin Hall effects, [4] and spin Seebeck effects. [5] Nonlocal spin valves (NLSVs) have been used for above mentioned fundamental physics research, plus spin injection experiments in both metals [6–13] and semiconductors. [14, 15] For NLSVs, it has also been a long story since people pursuing a higher signal, or higher SNR (signal-to-noise ratio). Since the spin signal relies on spin polarization, spin diffusion length and resistivity in nonmagnetic materials, people have put much effort into optimization for these aspects to improve the efficiency of spin injection as well as increasing the value of spin diffusion length.

In this chapter, we describe a direct coupling between a charge accumulation and a spin accumulation in a ferromagnet near a highly resistive interface: a break-junction. The coupling originates from the fact that the conductivities and diffusion constants for spin-up and spin down electrons are different in a ferromagnet. As a result, a large spin accumulation is induced in the ferromagnet by a large charge accumulation near the break-junction and drives a substantial spin current across the resistive interface.

In the literature, [16-18] the influence of charge accumulation on the spin accumulation and the spin current is usually neglected. A spin current is considered to be driven by a spin accumulation instead of a charge accumulation. Generally, this view is legitimate because the charge accumulation is negligible in bulk metal. However in some special cases, the charge accumulation can be substantial near a highly resistive interface and thereby inducing a large spin accumulation through the spin-charge coupling. The large spin accumulation is associated with a large chemical potential split between the spin up and the spin down bands, which provides conduction channels for a substantial interfacial spin current. We demonstrate this effect by investigating the large spin signals observed in a nonlocal spin valve (NLSV) with a highly resistive break-junction tunnel barrier between the ferromagnetic spin detector and the nonmagnetic channel. Compared to our previous work, [19] the new contributions here are the following: (i) both inverted and non-inverted large spin signals are demonstrated in break-junction nonlocal spin valves; (ii) experiments have been carried out to demonstrate the nonlocal nature of the measurements and rule out spurious effects; (iii) profiles of spin dependent electrochemical potentials across the interface are calculated and discussed; (iv) we demonstrate theoretically that both inverted and non-inverted of spin signals are possible depending on the values of conductivities, diffusion constants, and density of states around the break-junction.

6.2 Experiments

6.2.1 Regular nonlocal spin signal

A cartoon illustration and a scanning electron microscope (SEM) picture of a NLSV structure are shown in Figure 6.1(a) and 6.1(b), respectively. The F_1 injector

and F_2 detector are made of Co or Py and the N channel is made of Cu. The scale bar in the SEM picture represents 200 nm. The widths of the F_1 and F_2 range from 80 nm to 200 nm and the widths of the Cu channels range from 100 nm to 200 nm. The center-to-center distance between F_1 and F_2 varies from 200 nm to 600 nm. The thickness values are 8 nm-20 nm for magnetic electrodes (F_1 and F_2) and 70 nm-100 nm for Cu channels. A layer (2 nm) of AlO_x is placed at the F_1/N and F_2/N interfaces to enhance the interfacial spin polarizations. The resistances of the F_1/N and F_2/N interfaces are between 200 Ω and 2000 Ω.

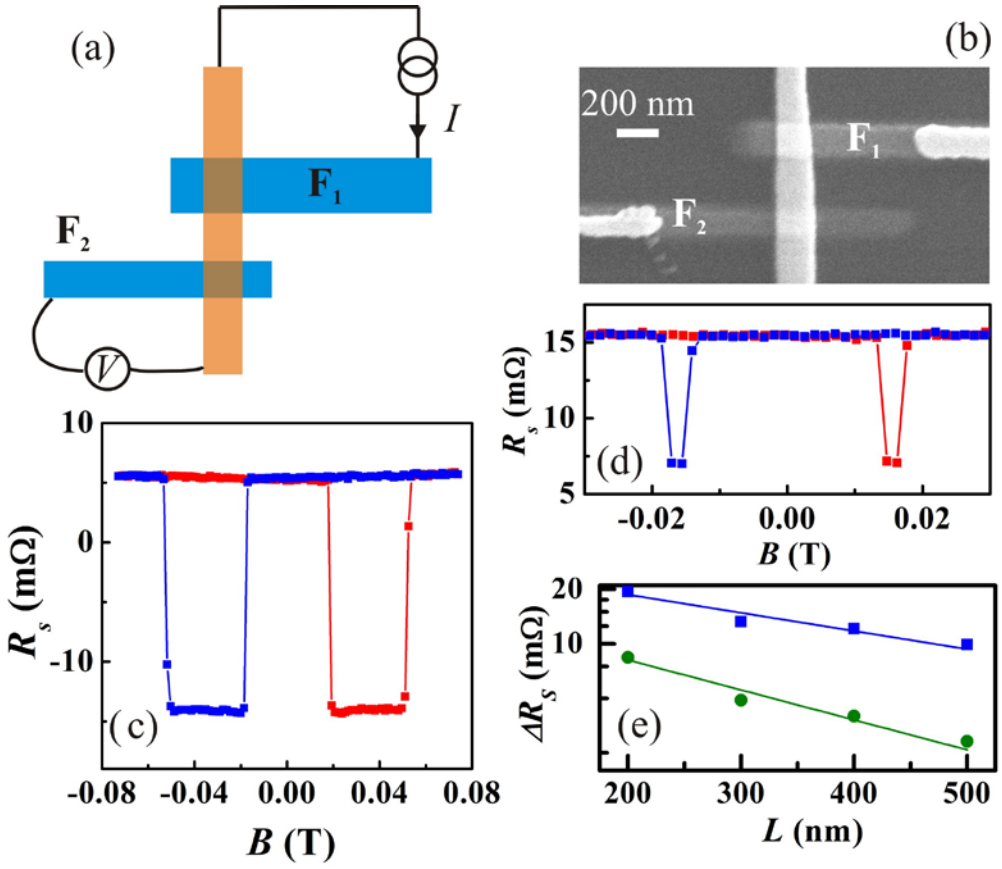

Figure 6.1: (a) Cartoon illustration of a nonlocal spin valve. (b) SEM picture of a nonlocal spin valve. The scale bar represents 200 nm. (c) Nonlocal resistance R_s versus magnetic field B curve at 4.2 K. (d) R_s versus B curve at 295 K. (e) ΔR_s versus L curves on semi-log scale at 4.2 K (squares) and 295 K (circles) and fits (straight lines).

The fabrication of the structures is achieved by electron-beam lithography followed by a shadow evaporation technique. [20-22] The injector and detector interfaces (F_1/N and F_2/N) are formed in pristine condition and suitable for spin-transport. More details of the fabrication method can be found from other literatures. [20, 21]

The measurement scheme is shown in Figure 6.1(a): an electric current I_s is injected from F_1 into N and the nonlocal voltage V_s is detected between F_2 and opposite end of N. The ac injection current I_s is 0.1 mA at a low frequency ranging from 100 Hz to 2000 Hz and the ac nonlocal voltage V_s is measured using a lock-in amplifier. The nonlocal resistance, $R_s = V_s/I_s$, is recorded as a function of magnetic field H. The R_s versus H curves for a NLSV structure at 4.2 K and 295 K are shown in Figure 6.1(c) and (d), respectively. The high value of R_s corresponds to the parallel (P) magnetizations of F_1 and F_2 and the low value of R_s corresponds to the antiparallel (AP) state. The nonlocal spin signal ΔR_s is defined as the difference between the P and AP states. The magnitudes of ΔR_s are ~20 mΩ (Figure 6.1(c)) at 4.2 K and ~8 mΩ (Figure 6.1(d)) at 295 K. The nonlocal spin signal is often described as following equation: [8]

$$\Delta R_s = \frac{P_1 P_2 \rho \lambda_s}{A} e^{-\frac{L}{l_s}} \qquad (6.1)$$

where P_1, P_2 are the interfacial spin polarizations for F_1/N and F_2/N, respectively, and l_s represents the spin diffusion length of the nonmagnetic metal (Cu in this case).

Parameter ρ stands for the resistivity of the nonmagnetic channel, A is the cross section area of the Cu channel, and L is the center to center distance between F_1 and F_2. For the structure in Figure 6.1(c) and 6.1(d): $L = 200\ nm$, $\rho = 1.4\ \mu\Omega \bullet cm$, and $A = 100 \times 72\ nm^2$.

To determine the values of P_1, P_2 and l_s, three additional structures with different injector-to-detector distances (L = 300 nm, 400 nm and 500 nm) but otherwise identical dimensions are fabricated in the same batch and measured at both 4.2 K and 295 K. Figure 6.1(e) demonstrates nonlocal spin signal ΔR_s as a function of distance L. The solid line is the fitting using Eq. 6.1 (assuming $P_1 = P_2$) since the two junctions are fabricated under identical conditions. The fitting yields that $P_1 = P_2 = 21\%$ and $l_s = 460$ nm at 4.5 K, $P_1 = P_2 = 14\%$ and $l_s = 290$ nm at 295 K.

In Figure 6.1 (c) and (d), the R_s value of P state is higher than the R_s value of AP state and this is the case for most spin signals in nonlocal spin valves. We consider them "non-inverted" spin signals in contrast to the "inverted" spin signals which will be discussed later. An "inverted" spin signal, where the R_s value of P state is lower than the R_s of AP state, is possible if the spin polarizations P_1 and P_1 have opposite signs. Since positive polarizations are far more common than negative polarizations for ferromagnetic metals, most nonlocal spin valves show non-inverted spin signals instead of inverted spin signals. In few cases [14, 23] an inverted spin signals, due to a negative polarization from one magnetic electrode, are observed when a large bias voltage is applied to the injector interface. However, those previous results have completely different origins comparing to the break-junction we discovered here.

6.2.2 Break-junction nonlocal spin valves

A vacuum break-junction is formed between spin detector F_2 and the Cu channel. The break-junction at the F_2/N interface is formed by electro-migration from static charge or a voltage spike. The fabrication procedure and sample dimensions are the same as those of the regular NLSV structures described earlier. We observed both inverted and non-inverted spin signals with magnitudes significantly larger than the spin signals in regular NLSV structures. Neither the magnitudes can be described by the simple formula of Eq. 6.1 nor the inverted spin signals can be understood by simply assuming opposite signs of P_1 and P_2. A more comprehensive understanding of the spin-charge coupling effects across the break-junction is necessary to account for the signs and the magnitudes.

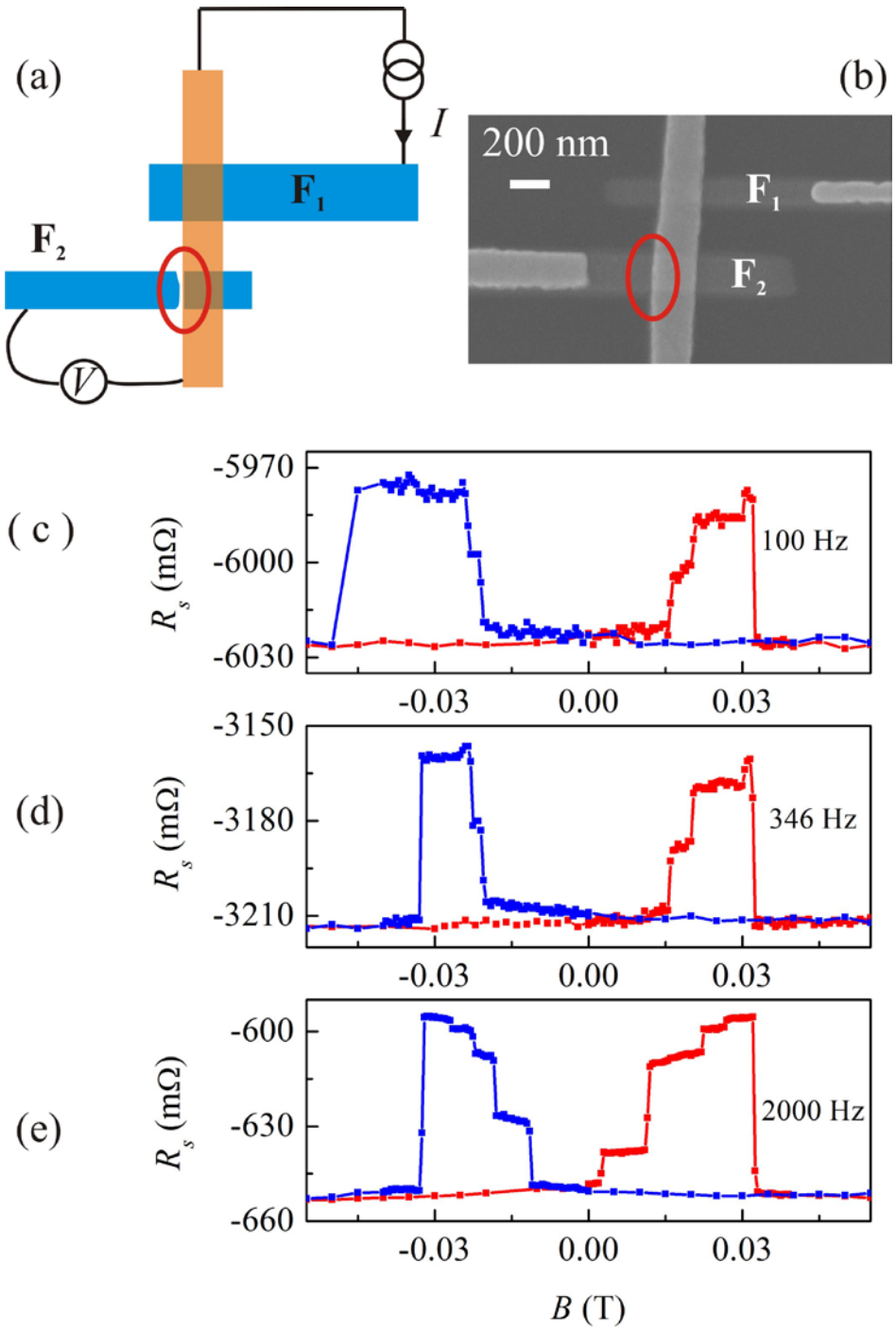

Figure 6.2: (a) Illustration of a break-junction NLSV structure. (b) SEM picture of a break-junction NLSV structure. The scale bar represents 200 nm. (c) R_s versus B curve of a Py/Cu break-junction NLSV measured at 100 Hz, (d) 346 Hz, and (e) 2000 Hz.

6.2.2.1 Break-junction: inverted spin signals from Py-Cu NLSVs

The break-junction is essentially a vacuum tunneling gap for spin polarized electrons between F_2 and the Cu channel, as indicated by the red circle in the cartoon illustration of structure in Figure 6.2 (a). The size of the vacuum gap should be no more than several nanometers. The experimental evidence of such a nanometer sized gap is the following. First, the resistances of the F_2/N junctions, measured by applying a small d.c. voltage and detecting the d.c. currents, are at least in the MΩ range. As a comparison, the resistances of as-fabricated F_1/AlO_x/Cu and F_2/AlO_x/Cu junctions are orders of magnitude smaller in the range of 5 Ω - 2000 Ω. Second, in the SEM images of the break-junction structures, no apparent gap at the F_2/N junctions can be resolved. An example of such SEM image is shown in Figure 6.2 (b). The red circle indicates the location of the gap, which is smaller than the resolution of SEM. Third, the large spin signal of a break-junction NLSV possesses a high percentage value comparing to the baseline of the signal and disappears when a trivial break is formed between F_2 and N channel. This indicates that the large spin signal is due to truly nonlocal measurement nature across a small gap at F_2/N interface rather than a trivial break in the circuit. More details for the third point will be discussed later involving Figure 6.4.

The break-junction gap is formed by electromigration. Electromigration induced by a feedback-controlled voltage has been shown by previous works to be effective in generating a nanometer-sized gap between nanoscale electrodes. [24-26] In this work, the electromigration is caused by a static-discharge or a voltage-spike that occurs accidentally through the NLSV structure. Electrostatic discharge and voltage spikes are common in electrical measurements. A static discharge occurs when the NLSV structure is in contact with a conductive object with a different potential, such as a human body or measurement equipment. A voltage spike occurs when there

is a sudden change of load in the power line and can be passed onto the NLSV structure through the measurement equipment. Dramatic discharge and voltage spikes can damage a delicate structure such as a NLSV. A modest static discharge, however, can induce electromigration and generate a nanometer-sized gap: a break-junction.

Measures such as proper grounding and surge protector can reduce dramatic occurrences of static discharge or voltage spikes to protect NLSV. But due to the sophisticated nature of the fabrication procedure and the long measurement time, modest discharge or voltage spikes can still occur at various situations. It is our goal to eventually fabricate break-junction based NLSV structures using controllable eletromigration. But at this stage, the break-junction based NLSV structures are achieved by an accidental occurrence of electro-static discharge or voltage spikes. The break-junctions are more likely to be found on the thin magnetic electrode, which is more resistive and susceptible to the electromigration. In measurements, we always use the break-junction electrode as the detector (F_2) and the other one as the injector (F_1) since it is difficult to inject a current through the highly resistive break-junction.

Figure 6.2 (c) – (e) show the R_s versus H curves of a Py-Cu break-junction NLSV structure measured at 4.2 K with different a.c. frequencies (100 Hz, 346 Hz, and 2000 Hz). The purpose of varying frequency is to demonstrate the nonlocal nature of the spin signal and rule out the possibility of spurious local effects. The baseline (average R_s value of the P state and AP sate) of the R_s versus H curves varies with the frequency from -6000 mΩ at 100 Hz to -630 mΩ at 2000 Hz. But the spin signals ΔR_s essentially remain the same (50 mΩ – 60 mΩ). The percentage values of the signal (the ratio of ΔR_s to the baseline) are ~1% at 100 Hz, ~2% at 346 Hz, and ~10% at

2000 Hz. The consistent ΔR_s values at all frequencies and the large percentage value (10%) at a certain frequency affirm the nonlocal nature of the signal.

In principle, the baseline should be zero for a nonlocal measurement. But in experiments it is never strictly zero and can be relatively large at times. The baseline also depends on the frequency of the a.c. modulation currents and the bias d.c. currents. The origin of the non-zero, bias-dependent, and frequency-dependent baseline is not clearly described in literature but could arise from several factors: the three-dimensional current distribution, [27] capacitive and inductive coupling in the measurement circuits, thermoelectric effects, and charge accumulation near the interface. However, the absolute magnitude of the spin signal ΔR_s for a truly nonlocal measurement should be an intrinsic value of the structure and independent of the frequencies, as shown in Figure 6.2 (c) - (e). On the contrary, for local magnetoresistive effects, the percentage value $\Delta R/R$ is a more consistent value. For example, the percentage value of anisotropic magnetoresistance (AMR) is typically < 3% and should not change when the frequency of injected currents varies. As shown in Figure 6.2 (e), the percentage value of the signal reaches 10% at 2000 Hz, which is clearly higher than the trivial local effects such as AMR.

The magnitude of spin signals is 50 – 60 mΩ, which is larger than the spin signals in any regular metallic NLSV structures we have measured to date. The dimensions of the structure are measured to be that $A = 100 \times 72\ nm^2$ and $L = 480\ nm$. If we used the values of P_1, P_2 and l_s extracted from Figure 6.1 for calculation, a spin signal of 14 mΩ is expected in a regular NLSV with the same dimensions. Another important feature in Figure 6.2 (c) to (e) is that the spin signals are inverted with low R_s values in the P states (in high magnetic fields) and high R_s

values in the AP states (in intermediate magnetic fields) of F_1 and F_2, opposite to the regular NLSV spin signals described in Figure 6.1.

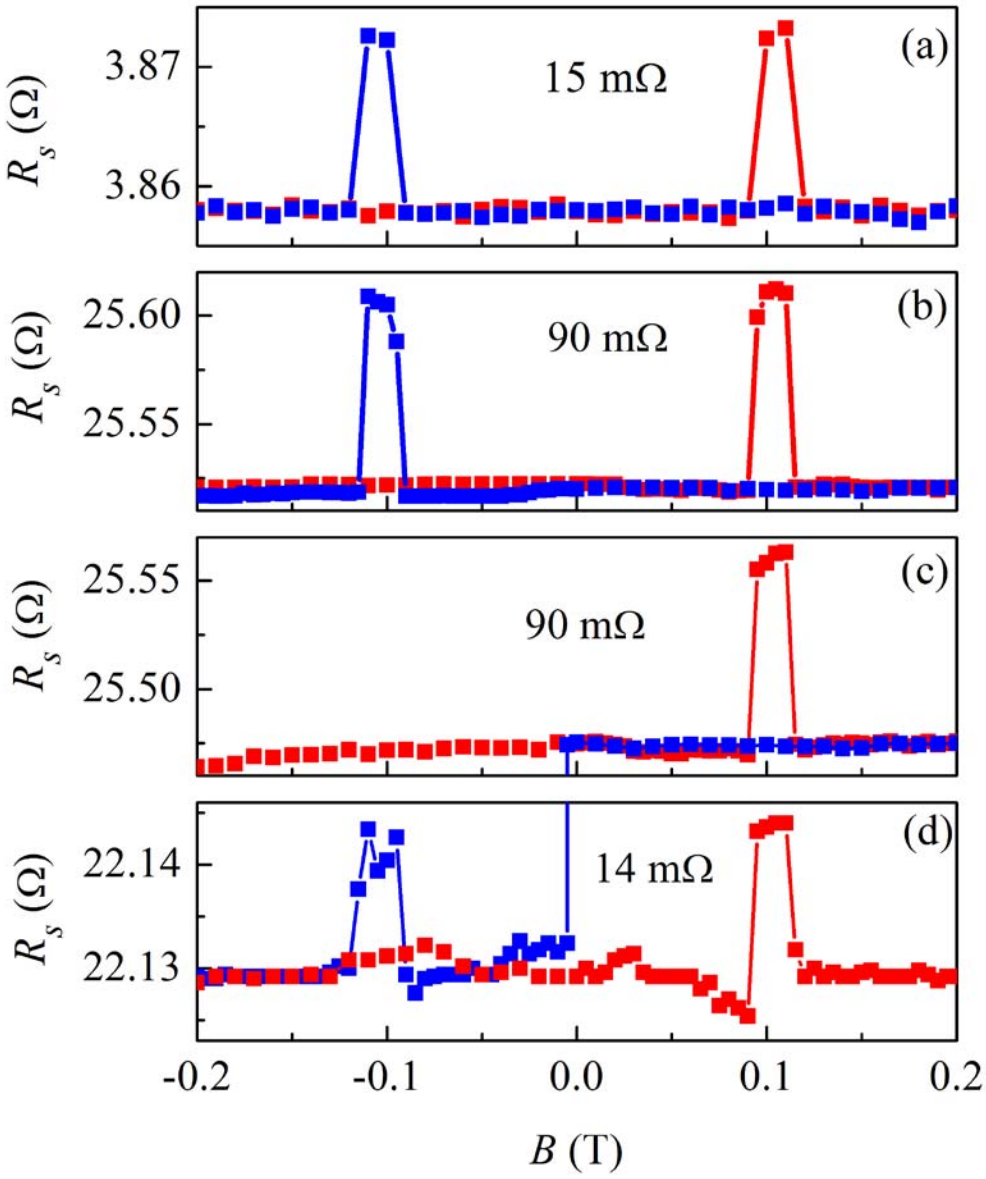

Figure 6.3: Evolution of R_s versus B curves for a Co-Cu break-junction NLSV structure at 4.2 K. (a) through (d) are arranged in temporal order.

6.2.2.2 Break-junction: inverted spin signals from Co-Cu NLSVs

The inverted large spin signals have also been observed in a Co-Cu break-junction NLSV structure, shown in Figure 6.3. The measurement, carried out at 4.2 K, continues for a 20-hour period until the F_1 electrode is ultimately damaged by a dramatic static discharge or voltage spike. The magnitude of the spin signal changes twice during the measurement and the changes are attributed to modest static discharge or voltage spikes that modify the configuration of the break-junction at F_2/N interface. This evolution of the spin signal demonstrates delicate nature of the break-junction in the device.

Initially an inverted spin signal of 15 mΩ with a baseline of 3.8 Ω is observed, as shown in Figure 6.3 (a), and it is well reproducible during continuous field sweeps. Afterwards, the wiring configuration of the measurement circuit is rearranged to measure the resistances at F_1/Cu and F_2/Cu interfaces, while the device is immersed in the cryostat. Then the R_s versus H curve is measured again at 4.2 K and the inverted spin signal is increased to 90 mΩ and the baseline is increased to 25 Ω, as shown in Figure 6.3 (b). The R_s versus H curve with the 90 mΩ spin signal are stable for several hours, but suddenly changed to a spin signal of 14 mΩ with a baseline of 22 Ω, as shown in Figure 6.3 (c) and (d). An evolution of this nature is not expected from a spurious effect such as AMR. The higher baseline (3.8 Ω – 25 Ω) is due to a large charge accumulation across the interface, which will be discussed in Section 6.3.4.

The dimensions of the Co-Cu break-junction NLSV are measured to be that $A = 130 \times 100\ nm^2$ and $L = 190\ nm$. Using $P_1 = P_2 = 14\%$ [28] and $l_s = 460\ nm$ for a regular Co-Cu NLSV of the same dimension, the expected spin signal is ~ 7 mΩ, much smaller than the 90 mΩ observed here. A quantitative description using Eq. 6.1 is no longer appropriate. The spin accumulation in F_2 is higher than the spin

accumulation in the Cu channel due to the spin-charge coupling. Details will be discussed later in the theory section.

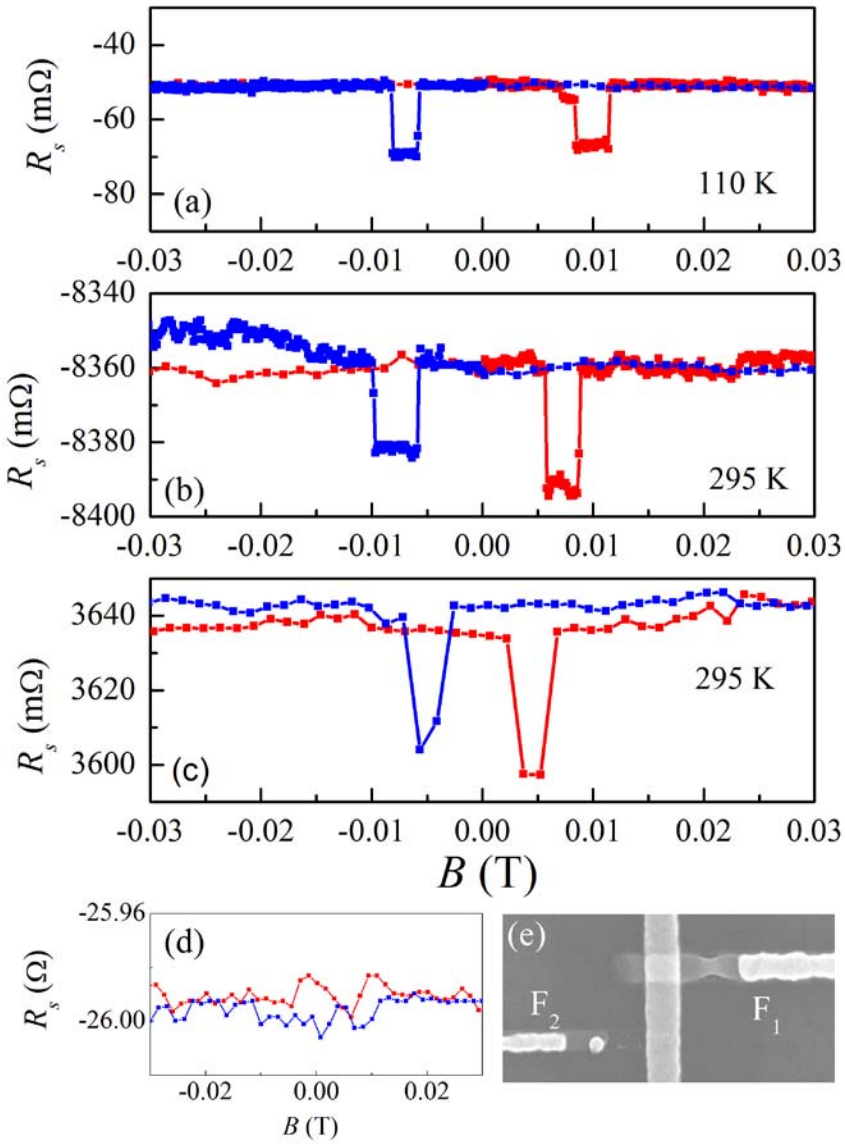

Figure 6.4: Several non-inverted spin signals from Py-Cu break-junction NLSV structures. (a) Non-inverted 19 mΩ at 110 K; (b) non-inverted 30 mΩ at 295 K; (c) non-inverted 40 mΩ at 295; (d) After a catastrophic break is formed in the device used for the data in (c), no spin signal is detected; (e) SEM picture showing the catastrophic break between F_2 and Cu.

6.2.2.3 Break-junction: non-inverted spin signals from Py-Cu NLSVs

Non-inverted spin signals have been observed in Py-Cu break-junction NLSV structures as well. The R_s versus B curves of these measurements are shown in Figure 6.4 (a) – (c). The R_s value is high for the P states and low for the AP states. In Figure 6.4 (a), ΔR_s = 19 mΩ at 110 K and the baseline is – 62 mΩ and therefore percentage value is ~ 30%, which clearly rules out trivial local effects. In Figure 6.4 (b) ΔR_s = 30 mΩ at 295 K and the baseline is - 8.4 Ω. In Figure 6.4 (c) ΔR_s = 40 mΩ at 295 K and the baseline is 3.6 Ω.

The break-junction NLSV structure described in Figure 6.4 (c) was suddenly altered by a static discharge or voltage spike during measurement. Afterwards, the baseline changed and the spin signal disappeared as shown in Figure 6.4 (d). The SEM picture in Figure 6.4 (e), which was taken after the measurement, shows that a catastrophic gap (~ 200 nm) is formed between F_2 and Cu channel, completely separating F_2 and Cu channel. This illustrates that the spin signal only arises from a tiny nanometer-size tunneling gap instead of a catastrophic break in the structure.

We will continue to describe the theoretical description of the spin-charge coupling, which accounts for both the large magnitudes and the signs of the spin signals in break-junction structures in the following structure. We will show that the spin accumulation across the break-junction is amplified along the direction of the spin current, yielding a large spin signal.

6.3 Theory

6.3.1 Basic Assumptions and Equations

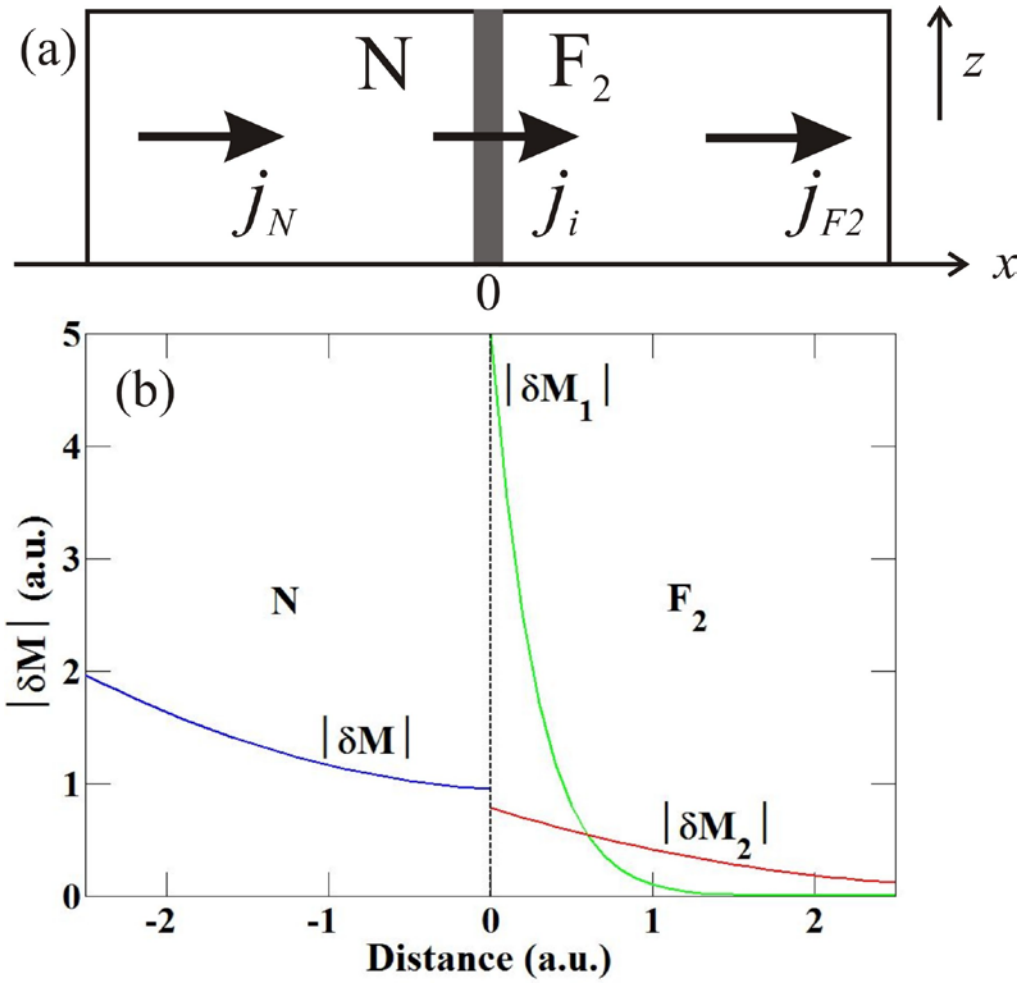

Figure 6.5: (a) Basic assumptions of the one dimensional theoretical model. Nonmagnetic metal (N) is located in the region where $x < 0$, and F_2 is located in the region where $x > 0$. A tunneling barrier is formed at $x = 0$. The spin current is continuous across the barrier. (b) The spin accumulations across the N/F_2 interface.

The essential physics of spin-charge coupling occurs at the F_2 side of the N/F_2 interface. We consider the problem in a simple one-dimensional system involving a nonmagnetic metal N, a tunnel barrier, and a ferromagnet F_2, as shown in Figure 6.5 (a). A z-direction polarized spin accumulation is present in N and drives a spin current along the *x* direction. The spin accumulation in N is induced by the spin injection at the F_1/N interface. We assume the spin accumulation in the N channel ($x < 0$) as a function of *x* is known. The pure spin current density in the N channel ($x < 0$) is a gradient of the spin accumulation and therefore is known as well. (There is no back-flow because N does not end in F_2 and extends beyond the F_2 electrode). The spin-charge coupling influences the spin accumulation in the F_2 side ($x > 0$) and this will be the focus of the following discussion.

We also assume the continuity of the spin current density and the charge current density at the interface. The charge current density should be zero everywhere since this is the nonlocal region where only the spin current is present. The spin current at $x = 0^-$ (in N), the spin current across the tunnel barrier, and the spin current at $x = 0^+$ (in F_2) are all equal: $j_s|_{x=0^-} = j_{si} = j_s|_{x=0^+}$. The spin current decays to zero as *x* approaches $+\infty$. These are the basic assumptions of the theory. This simplifies the problem into a one-dimensional system without altering the essential physics.

The spin-charge coupling [29, 30] originates from the difference between spin-up and spin-down values of conductivities ($\sigma_\uparrow$ for spin-up and $\sigma_\downarrow$ for spin-down) and diffusion constants ($D_\uparrow$ for spin-up and $D_\downarrow$ for spin-down). The current density of spin-up electrons can be described by $\overrightarrow{j_\uparrow} = -\sigma_\uparrow \nabla V + D_\uparrow \nabla \delta n_\uparrow$ and the current density of spin-down electrons can be described by $\overrightarrow{j_\downarrow} = -\sigma_\downarrow \nabla V + D_\downarrow \nabla \delta n_\downarrow$, where $\delta n_\uparrow$ ($\delta n_\downarrow$) is the deviation of population density from the equilibrium for spin-up (spin-down). We

have used units so that the Bohr magneton and the electric charge is 1. The electric potential *V* includes the potential due to the external electric field and the local electric potential due to charge accumulation. The charge accumulation is given by $\delta n = \delta n_\uparrow + \delta n_\downarrow$, and the spin accumulation is given by $\delta M = \delta n_\uparrow - \delta n_\downarrow$. The charge current is defined by $\overrightarrow{J_c} = \overrightarrow{J_\uparrow} + \overrightarrow{J_\downarrow}$, and the spin current is defined by $\overrightarrow{J_s} = \overrightarrow{J_\uparrow} - \overrightarrow{J_\downarrow}$.

It follows from the above that both $\overrightarrow{J_c}$ and $\overrightarrow{J_s}$ are related to the spin accumulation δM and the charge accumulation δn:

$$\overrightarrow{J_c} = -\sigma \nabla V + D\nabla(\delta n) + D'\nabla(\delta M) \qquad (6.2)$$

$$\overrightarrow{J_s} = -\sigma' \nabla V + D\nabla(\delta M) + D'\nabla(\delta n) \qquad (6.3)$$

where $\sigma = \sigma_\uparrow + \sigma_\downarrow$, $\sigma' = \sigma_\uparrow - \sigma_\downarrow$, $D = (D_\uparrow + D_\downarrow)/2$ and $D' = (D_\uparrow - D_\downarrow)/2$. The coupling between δn and δM is manifested by the terms involving *D'* and σ'. The charge (spin) current not only depends on the charge (spin) accumulation but also depends on the spin (charge) accumulation.

In addition, charge conservation requires that the divergence of charge current vanishes in steady states:

$$\nabla \cdot \overrightarrow{J_c} = \frac{\partial \delta n}{\partial t} = 0 \qquad (6.4).$$

The magnetization satisfies the modified Landau-Gilbert equation with a source term proportional to the divergence of the magnetization. In the steady state with a longitudinal spin accumulation, we have

$$\nabla \cdot \overrightarrow{J_s} = \frac{\delta M}{\tau} \qquad (6.5),$$

where τ is the spin relaxation time. The solutions of Eq. 6.2-6.5 can be expressed by

$$\delta n = \delta n_{10} e^{-x/\lambda} + \delta n_{20} e^{-x/l} \qquad (6.6)$$

$$\delta M = \delta M_{10} e^{-x/\lambda} + \delta M_{20} e^{-x/l} \qquad (6.7),$$

where λ is the renormalized charge screening length and l is the renormalized spin diffusion length. Typically λ is in the order of 0.1 nm and l is in the order of 10 nm in ferromagnets and therefore $l >> \lambda$. There are two terms for either δn or δM due to the spin-charge coupling: a fast decaying term on the scale of λ and a slowly decaying term on the scale of l. The spatial dependence of δM across the interface is illustrated in Figure 6.5 (b) with $\delta M_1 = \delta M_{10} e^{-x/\lambda}$ and $\delta M_2 = \delta M_{20} e^{-x/l}$.

Substituting Eq. 6.6 and 6.7 into Eq. 6.2 and 6.3, and then into Eq. 6.4 and 6.5 will lead to two equations with terms involving both $e^{-x/\lambda}$ and $e^{-x/l}$. In each equation, let the coefficients for each type of terms vanishes. Thereby one can obtain four equations, from which four quantities (λ, $\frac{\delta n_{10}}{\delta M_{10}}$, l, and $\frac{\delta n_{20}}{\delta M_{20}}$) can be derived. Coulomb's law $\nabla^2 V = 4\pi\delta n$ is used in eliminating the variable of electric potential V. Terms related to $e^{-x/\lambda}$ in Eq. 6.5 can be simplified into $\nabla \cdot \overrightarrow{J_{s1}} \approx 0$ by taking into account the fact that $\frac{1}{\lambda^2} \gg \frac{1}{l^2} \sim \frac{1}{\tau D}$. The quantity $\overrightarrow{J_{s1}}$ is the spin current due to the $e^{-x/\lambda}$ terms. The results are,

$$\frac{\delta n_{10}}{\delta M_{10}} = \frac{\sigma_\uparrow D_\downarrow + \sigma_\downarrow D_\uparrow}{\sigma_\uparrow D_\downarrow - \sigma_\downarrow D_\uparrow}. \tag{6.8}$$

$$\lambda^2 = \frac{D_\uparrow D_\downarrow}{4\pi(\sigma_\uparrow D_\uparrow + \sigma_\downarrow D_\downarrow)} \tag{6.9}$$

$$l^2 = \frac{\left[8\pi(\sigma_\uparrow D_\downarrow + \sigma_\downarrow D_\uparrow) + \frac{D_\uparrow + D_\downarrow}{\tau}\right] + \sqrt{\left[8\pi(\sigma_\uparrow D_\downarrow + \sigma_\downarrow D_\uparrow) + \frac{D_\uparrow + D_\downarrow}{\tau}\right]^2 - \frac{64\pi}{\tau}(\sigma_\uparrow + \sigma_\downarrow) D_\uparrow D_\downarrow}}{\frac{16\pi}{\tau}(\sigma_\uparrow + \sigma_\downarrow)} \tag{6.10}$$

$$\frac{\delta n_{20}}{\delta M_{20}} = \frac{D_\uparrow - D_\downarrow}{8\pi l^2(\sigma_\uparrow + \sigma_\downarrow) - (D_\uparrow + D_\downarrow)} \tag{6.11}.$$

The quantity λ is the renormalized charge screening length and the l is the renormalized spin diffusion length. In the trivial case of a nonmagnetic metal, where $D_\uparrow = D_\downarrow = D$ and $\sigma_\uparrow = \sigma_\downarrow = \frac{\sigma}{2}$, Eq. 6.9 and 6.10 are reduced to that $\lambda^2 = \frac{D}{4\pi\sigma}$ and $l^2 = \tau D$. With the boundary conditions that the spin current density and the charge current density across the N/F_2 interface is continuous, the values of δn_{10}, δM_{10}, δn_{20}, and δM_{20}, can be determined.

The fast decaying terms $\delta n_{10} e^{-\frac{x}{\lambda}}$ and $\delta M_{10} e^{-\frac{x}{\lambda}}$ on the scale of λ (~ 0.1 nm) and the slowly decaying terms $\delta n_{20} e^{-\frac{x}{l}}$ and $\delta M_{20} e^{-\frac{x}{l}}$ on the scale *l* (~ 10 nm) have distinct roles in spin transport. The role of the slowly decaying terms $\delta M_{20} e^{-\frac{x}{l}}$ and $\delta n_{20} e^{-\frac{x}{l}}$ is similar to that of the conventional spin accumulation in a ferromagnet without taking into account of the spin-charge coupling. These terms slowly decay over the spin diffusion length *l* and drive a spin current in the bulk of the ferromagnet. It is associated with a split between spin-up and spin-down electro-chemical potentials on the scale of *l* near the interface. The fast decaying terms $\delta n_{10} e^{-\frac{x}{\lambda}}$ and $\delta M_{10} e^{-\frac{x}{\lambda}}$ do not drive a spin current in the bulk of a ferromagnet (F_2). Substituting Eq. 6.8 and 6.9 into Eq. 6.3 we find that the charge and magnetization driven currents proportional to $e^{-\frac{x}{\lambda}}$ cancel out yielding zero spin current: $j_{s1}(x) = 0$.

We next address the boundary conditions across the interface. The primary role of the fast decaying terms $\delta M_{10}(\delta n_{10}) e^{-x/\lambda}$ is to provide a large chemical potential split between the spin-up and spin-down electro-chemical potentials near the interface ($x = 0^+$) to accommodate an interfacial spin current. The current density for each spin state across the interface is determined by the electro-chemical potential change across the interface for that spin state and the spin-dependent resistance of the N/F_2 interface. More specifically

$$j_{i\uparrow} = -\left(\mu_{ecp\uparrow}\big|_{x=0^-} - \mu_{ecp\uparrow}\big|_{x=0^+}\right) \cdot \frac{1}{R_{i\uparrow} \cdot A} \qquad (6.12),$$

$$j_{i\downarrow} = -\left(\mu_{ecp\downarrow}\big|_{x=0^-} - \mu_{ecp\downarrow}\big|_{x=0^+}\right) \cdot \frac{1}{R_{i\downarrow} \cdot A} \qquad (6.13),$$

where $R_{i\uparrow}$ and $R_{i\downarrow}$ are the resistance of the N/F_2 interface for spin-up and spin-down, respectively, and *A* is the area of the junction. The values of $\mu_{ecp\uparrow}$ and $\mu_{ecp\downarrow}$ are electrochemical potentials for spin-up and spin-down electrons. The electrochemical

potential is the sum of chemical potential and the electric potential: $\mu_{ecp1\uparrow} = \delta\mu_{1\uparrow} - V$ and $\mu_{ecp1\downarrow} = \delta\mu_{1\downarrow} - V$. We next evaluate the chemical potentials.

Assume $\delta\mu_{10\uparrow}$ and $\delta\mu_{10\downarrow}$ are the deviations of chemical potentials from equilibrium for spin-up and spin-down at $x = 0^+$. By using Eq. 6.8 and the relations $\delta n_{10\uparrow} = N_\uparrow \delta\mu_{10\uparrow}$, $\delta n_{10\downarrow} = N_\downarrow \delta\mu_{10\downarrow}$, $\delta M_{10} = \delta n_{10\uparrow} - \delta n_{10\downarrow}$, and $\delta n_{10} = \delta n_{10\uparrow} + \delta n_{10\downarrow}$, we obtain

$$\frac{\delta\mu_{10\uparrow}}{\delta\mu_{10\downarrow}} = \left(\frac{\sigma_\uparrow}{N_\uparrow D_\uparrow}\right) \Big/ \left(\frac{\sigma_\downarrow}{N_\downarrow D_\downarrow}\right) \qquad (6.14).$$

This gives a direct relationship between the spin-up and spin-down chemical potentials.

In the special case of $\sigma_\uparrow = N_\uparrow D_\uparrow$ and $\sigma_\downarrow = N_\downarrow D_\downarrow$, Eq. 6.14 is reduced to $\delta\mu_{10\uparrow} = \delta\mu_{10\downarrow}$, which is a trivial case without a split of chemical potentials. The spin accumulation $\delta M_{10} = \frac{(N_\uparrow - N_\downarrow)}{(N_\uparrow + N_\downarrow)}\delta n_{10}$ is a trivial consequence of the difference in the spin-up and spin-down density of states. The relations $\sigma_\uparrow = N_\uparrow D_\uparrow$ and $\sigma_\downarrow = N_\downarrow D_\downarrow$ are known as the Einstein relation and often assumed in the spin-transport discussion in the literature. [17, 18] However, in the full quantum mechanical description, this relationship is not satisfied exactly for each spin channel. In addition, the situation is further complicated by a population density far away from equilibrium within a short length scale (charge screening length $\lambda \sim 0.1$ nm). If we assume deviations from a precise 1 for the values of $\frac{\sigma_\uparrow}{N_\uparrow D_\uparrow}$ and $\frac{\sigma_\downarrow}{N_\downarrow D_\downarrow}$, then a non-trivial chemical potential split arises as described by

$$\delta\mu_{10\uparrow} - \delta\mu_{10\downarrow} = \mu_{ecp1\uparrow}\big|_{x=0^+} - \mu_{ecp1\downarrow}\big|_{x=0^+} = \Delta\mu_{ecp10} = \delta n_{10} \frac{\frac{\sigma_\uparrow}{N_\uparrow D_\uparrow} - \frac{\sigma_\downarrow}{N_\downarrow D_\downarrow}}{\left(\frac{\sigma_\uparrow}{D_\uparrow} + \frac{\sigma_\downarrow}{D_\downarrow}\right)}$$

(6.15).

This expression also gives the electro-chemical potential split $\Delta\mu_{ecp10}$ at $x = 0^+$ in F_2.

6.3.2 Profiles of Electrochemical Potentials

We next address the electrochemical potential $\mu_{ecp1\uparrow}(x)$ and $\mu_{ecp1\downarrow}(x)$ in F_2 (x > 0). An electric potential V has to be taken into account to derive expressions for electro-chemical potentials. Due to the charge accumulation near the N/F_2 interface, a local screening field is present and generates an electric potential V that shifts the entire energy band on the energy scale. For the fast decaying spin and charge accumulations in F_2, as we previously discussed, the bulk spin current vanishes: $j_{s1} = j_{\uparrow 1} - j_{\downarrow 1} = 0$. Since the F_2/N interface is the nonlocal region, the charge current also vanishes: $j_{c1} = j_{\uparrow 1} + j_{\downarrow 1} = 0$. Thus $j_{\uparrow 1} = j_{\downarrow 1} = 0$, which means the current of each spin species vanishes. Employing the basic expressions for $j_\uparrow$ and $j_\downarrow$ given in the beginning of the theory section, and taking into account the relation $\delta n_{1\uparrow} = N_\uparrow \delta\mu_{1\uparrow}$ and $\delta n_{1\downarrow} = N_\downarrow \delta\mu_{1\downarrow}$, we have $j_{\uparrow 1} = -\sigma_\uparrow \frac{dV}{dx} + D_\uparrow N_\uparrow \frac{d\delta\mu_{1\uparrow}}{dx} = 0$. For a similar expression for the spin-down electrons, one can simply change the subscript from up to down. Simple manipulation yields $\frac{d}{dx}(\delta\mu_{1\uparrow} - V) + \left(\frac{D_\uparrow N_\uparrow}{\sigma_\uparrow} - 1\right)\frac{d}{dx}\delta\mu_{1\uparrow} = 0$. Using electrochemical potential $\mu_{ecp1\uparrow} = \delta\mu_{1\uparrow} - V$, this relation becomes $\frac{d}{dx}\mu_{ecp1\uparrow} = \left(1 - \frac{D_\uparrow N_\uparrow}{\sigma_\uparrow}\right)\frac{d}{dx}\delta\mu_{1\uparrow}$. Therefore, we have $\mu_{ecp1\uparrow} = \left(1 - \frac{D_\uparrow N_\uparrow}{\sigma_\uparrow}\right)\delta\mu_{1\uparrow} + C$, where C is a constant. Combined with Eq. 6.14 and 6.15, this relation can be expressed as

$$\mu_{ecp1\uparrow} = \frac{\frac{\sigma_\uparrow}{N_\uparrow D_\uparrow} - 1}{\frac{\sigma_\uparrow}{D_\uparrow} + \frac{\sigma_\downarrow}{D_\downarrow}}\delta n_1 + C = \frac{\frac{\sigma_\uparrow}{N_\uparrow D_\uparrow} - 1}{\frac{\sigma_\uparrow}{D_\uparrow} + \frac{\sigma_\downarrow}{D_\downarrow}}\delta n_{10} e^{-\frac{x}{\bar{\lambda}}} + C \qquad (6.16).$$

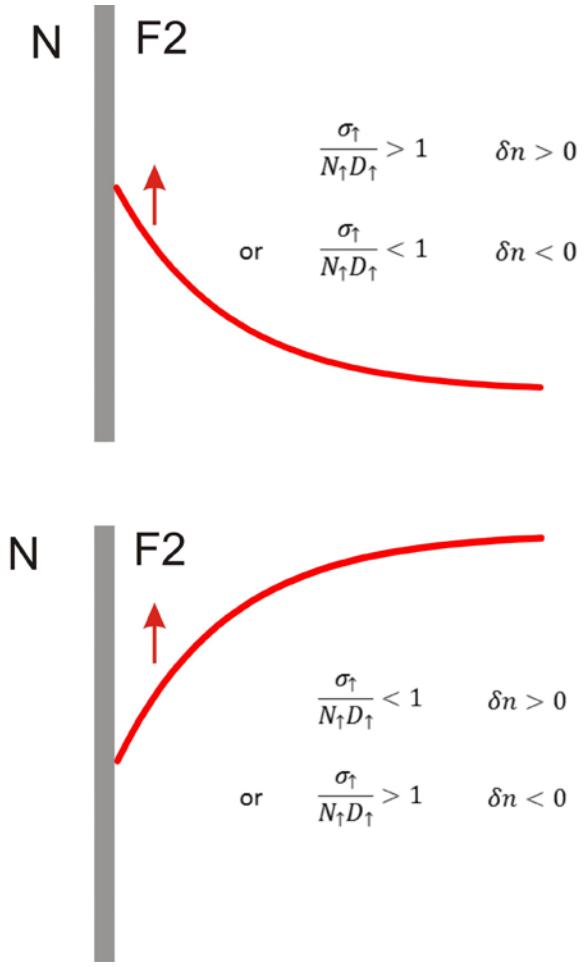

Figure 6.6: The spatial dependence of $\boldsymbol{u_{ecp1\uparrow}}$ for different values of $\frac{\sigma}{ND}$ and δn_{10}.

The spatial dependence of $\mu_{ecp1\uparrow}(x)$ on the F_2 side (x > 0) of the N/F_2 interface is illustrated in Figure 6.6. The value of $\mu_{ecp1\uparrow}(x)$ bends over on the scale of the charge screening length λ. From this figure we can see that the value either decreases or increases as x increases, depending on signs of $\left(\frac{\sigma_\uparrow}{N_\uparrow D_\uparrow} - 1\right)$ and δn_{10}. If $\frac{\sigma_\uparrow}{N_\uparrow D_\uparrow} > 1$ and $\delta n_{10} > 0$, or $\frac{\sigma_\uparrow}{N_\uparrow D_\uparrow} < 1$ and $\delta n_{10} < 0$, the value of $\mu_{ecp1\uparrow}(x)$ decreases as x increases, as shown in the upper panel of Figure 6.6. If $\frac{\sigma_\uparrow}{N_\uparrow D_\uparrow} < 1$ and $\delta n_{10} > 0$, or $\frac{\sigma_\uparrow}{N_\uparrow D_\uparrow} > 1$ and $\delta n_{10} < 0$, the value of $\mu_{ecp1\uparrow}(x)$ increases as x increases, as shown in

the lower panel of Figure 6.6. The vertical offset is given by a constant C, which is the final electro-chemical potential of F_2 at x = ∞, and it is ultimately determined by the boundary conditions. Similarly we can have the expression for $\mu_{ecp1\downarrow}$:

$$\mu_{ecp1\downarrow} = \frac{\frac{\sigma_\downarrow}{N_\downarrow D_\downarrow}-1}{\frac{\sigma_\uparrow}{D_\uparrow}+\frac{\sigma_\downarrow}{D_\downarrow}}\delta n_1 + C \qquad (6.17).$$

The constant C is the same for $\mu_{ecp1\uparrow}(x)$ and $\mu_{ecp1\downarrow}(x)$, because the electro-chemical potentials for spin-up and spin-down converges to the same value at x = ∞.

In addition to Eq. 6.12 and 6.13, the following boundary conditions should also be satisfied across the N/F_2 interface:

$$j_c = 0 \qquad (6.18),$$

$$j_s|_{x=0^-} = j_{si} = j_s|_{x=0^+} \qquad (6.19).$$

Eq. 6.18 is from the fact that the total charge current should stay zero because we are considering a nonlocal region with no charge current. Eq. 6.19 is from the continuity of the spin current: The spin current in N equals the interfacial spin current across N/F_2 and the spin current in F_2. Then it follows that $|j_{i\uparrow}| = |j_{i\downarrow}| = \frac{1}{2} j_s|_{x=0^-}$. As stated earlier, in this theoretical model we assume a well-defined fixed value for $j_s|_{x=0^-}$.Therefore $|j_{\uparrow i}|$ and $|j_{\downarrow i}|$ across the interface also have fixed values. The chemical potential difference $\left|\mu_{ecp\uparrow}\right|_{x=0^-} - \mu_{ecp\uparrow}\left|_{x=0^+}\right|$ or $\left|\mu_{ecp\downarrow}\right|_{x=0^-} - \mu_{ecp\downarrow}\left|_{x=0^+}\right|$ is proportional to the interfacial resistance $R_{i\uparrow}$ or $R_{i\downarrow}$ according to Eq. 6.12 and 6.13. For a break-junction interface at x = 0, resistance values $R_{i\uparrow}$ or $R_{i\downarrow}$ are large and thus large chemical potential differences are necessary. This will naturally lead to a large chemical potential split between spin-up and spin-down, $\left(\mu_{ecp\uparrow}\left|_{x=0^+} - \mu_{ecp\downarrow}\right|_{x=0^+}\right)$, at x = 0+. In the following, we argue that this large split can only come from the fast decaying spin accumulation.

The electro-chemical potential split in N, $\mu_{ecp\uparrow}\big|_{x<0} - \mu_{ecp\downarrow}\big|_{x<0}$, related to δMN, is proportional to the bulk spin current density in N, the resistivity of N, and the spin diffusion length of N, all of which are assumed to have fixed and modest values. Therefore the chemical potential split $\mu_{ecp\uparrow}\big|_{x=0^-} - \mu_{ecp\downarrow}\big|_{x=0^-}$ is a well-defined modest value. In F_2, the slowly decaying spin and charge accumulations (δM2 and δn2) yields a chemical potential split $\mu_{ecp2\uparrow}\big|_{x>0} - \mu_{ecp2\downarrow}\big|_{x>0}$, which is proportional to the bulk spin current density in F_2, the resistivity of F_2 and the spin diffusion length of F_2, all of which are also of fixed modest values. Therefore $\mu_{ecp2\uparrow}\big|_{x=0^+} - \mu_{ecp2\downarrow}\big|_{x=0^+}$ is a well-defined modest value. The large chemical potential split at x = 0+, as required by a substantial spin current across a resistive interface, can only come from the fast decaying spin and charge accumulations δM1 and δn1 and it is described in Eq. 6.15 as $\mu_{ecp1\uparrow}\big|_{x=0^+} - \mu_{ecp1\downarrow}\big|_{x=0^+}$.

Precisely speaking, the chemical potential in F_2 should be the sum of μ_{ecp1} and μ_{ecp2}. But for an interface with large resistance Ri, the magnitude of $\mu_{ecp1\uparrow}\big|_{x=0^+} - \mu_{ecp1\downarrow}\big|_{x=0^+}$ is much larger than $\mu_{ecp2\uparrow}\big|_{x=0^+} - \mu_{ecp2\downarrow}\big|_{x=0^+}$, and therefore the effect of the later will be ignored in the following discussion. The sign and the magnitude of the large chemical potential split at x = 0+ are directly related to the sign and the magnitude of the charge accumulation δn10, as indicated by Eq. 6.15. The vertical shift of the chemical potentials can be adjusted by constant C, as indicated by Eq. 6.16 and 5.17. The magnitude and sign of δn10 and C are chosen in such a way that the electrochemical potentials at x = 0+ satisfy the boundary conditions Eq. 6.12, Eq. 6.13, Eq. 6.18 and 6.19. Next we discuss how these boundary conditions affect the electrochemical potentials at x = 0+ using Figure 6.7.

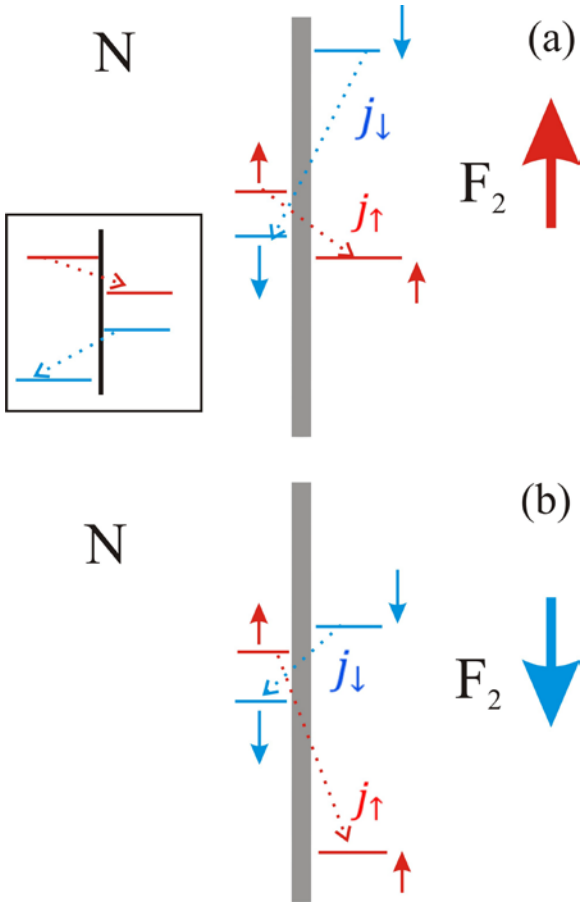

Figure 6.7: The electro chemical potentials at $x = 0^-$ and $x = 0^+$ for the magnetization of F_2 oriented (a) up and (b) down. The inset of (a) shows a configuration which violates the boundary conditions.

Figure 6.7 shows the necessary configurations of electro-chemical potentials at x = 0- and x = 0+ for the magnetization of F_2 pointing up (a) or down (b). In both cases the electrochemical potentials at x = 0+ has to be inverted ($\mu_{ecp1\uparrow}\big|_{x=0^+} < \mu_{ecp1\downarrow}\big|_{x=0^+}$) for a highly resistive interface. This is the only way to accommodate a large chemical potential split at x = 0+ and satisfy the boundary conditions (Eq. 6.18 and 6.19). Eq. 6.18 requires that the net charge current be zero and therefore $j_{i\uparrow}$ and $j_{i\downarrow}$ have to move in opposite directions. Eq. 6.19 requires that the net spin current j_s

across the interface should move to the right, because the spin current at x = 0- moves to the right. In Figure 6.7 (a) and (b), the spin-up current moves to the right and spin-down current moves to the left and therefore the conditions set by Eq. 6.18 and 6.19 are satisfied.

One situation with non-inverted chemical potentials is illustrated in the inset of Figure 6.7 (a). Though the spin current flows to the right, the changes in the electrochemical potentials across the barrier are less than the difference between the spin up and the spin down chemical potentials in N. The resulting spin current across the break-junction barrier is too small and cannot be equal to the incoming spin current, therefore violating the boundary condition Eq. 6.19.

When the magnetization of F_2 points up (Figure 6.7 (a)), spin-up is the majority spin and spin-down is the minority spin in F_2. Usually the majority spin band has a higher density of states and thus a higher interfacial conductance. We assume that this is true and thus the interfacial tunneling resistance for spin-up is lower than that for spin-down: $R_{i\uparrow} < R_{i\downarrow}$. Because the net charge current is zero, we have equal magnitudes for spin-up and spin-down currents: $|j_{i\uparrow}| = |j_{i\downarrow}|$. Since $R_{i\uparrow} < R_{i\downarrow}$, $\left(\mu_{ecp\uparrow}\big|_{x=0^-} - \mu_{ecp\uparrow}\big|_{x=0^+}\right) < \left(\mu_{ecp\downarrow}\big|_{x=0^+} - \mu_{ecp\downarrow}\big|_{x=0^-}\right)$ according to Eq. 6.12 and 6.13. A smaller electrochemical potential change is needed to drive the spin-up current because the interfacial resistance for spin-up is smaller. When the magnetization of F_2 points down (Figure 6.7 (b)), the spin-down is the majority spin and spin-up is the minority spin in F_2. The interfacial tunneling resistance for spin-up is higher than that for spin down: $R_{i\uparrow} > R_{i\downarrow}$. Therefore the electrochemical potentials across the interface satisfy $\left(\mu_{ecp\uparrow}\big|_{x=0^-} - \mu_{ecp\uparrow}\big|_{x=0^+}\right) > \left(\mu_{ecp\downarrow}\big|_{x=0^+} - \mu_{ecp\downarrow}\big|_{x=0^-}\right)$.

Though seemingly counter-intuitive, the inverted chemical potential split is physically possible as can be seen in Eq. 6.15. The sign of $\Delta\mu_{ecp10} = \mu_{ecp1\uparrow}\big|_{x=0^+} - \mu_{ecp1\downarrow}\big|_{x=0^+}$ depends on both $\left(\frac{\sigma_\uparrow}{N_\uparrow D_\uparrow} - \frac{\sigma_\downarrow}{N_\downarrow D_\downarrow}\right)$ and δn_{10}. If $\left(\frac{\sigma_\uparrow}{N_\uparrow D_\uparrow} - \frac{\sigma_\downarrow}{N_\downarrow D_\downarrow}\right) > 0$, a negative charge accumulation $\delta n_{10} < 0$ will produce the inverted chemical potential split $\Delta\mu_{ecp1} < 0$. If $\left(\frac{\sigma_\uparrow}{N_\uparrow D_\uparrow} - \frac{\sigma_\downarrow}{N_\downarrow D_\downarrow}\right) < 0$, a positive charge accumulation $\delta n_{10} > 0$ will produce the inverted split.

Essentially the charge accumulation provides an extra degree of freedom in the system to adjust the chemical potential split. The required chemical potential split can be achieved by choosing the sign and the magnitude of the charge accumulation properly. The large chemical potential split provides conduction channels to drive a substantial spin current across the N/F_2 interface. It is also noteworthy that the chemical potential split at x = 0+ in F_2 can be much larger than the chemical potential split at x = 0- in N, if the resistance of the barrier (x = 0) is large enough. This is a rare case of amplification of spin accumulation along the direction of the spin current. Normally in spin transport systems, the spin accumulation decays along the direction of the spin current.

From their values at x = 0+, the electrochemical potentials $\mu_{ecp1\uparrow}$ and $\mu_{ecp1\downarrow}$ converges to a common value C on the scale of charge screening length λ in F_2 (x > 0). The values of $\frac{\sigma_\uparrow}{N_\uparrow D_\uparrow}$ (or $\frac{\sigma_\downarrow}{N_\downarrow D_\downarrow}$) and δn_{10} determine whether $\mu_{ecp\uparrow}(x)$ (or $\mu_{ecp\downarrow}(x)$) increases or decreases as x (> 0) increases and eventually determines the signs and the magnitudes of the spin signals. Instead of a thorough discussion of all possible situations, we show that both inverted and non-inverted spin signals are possible with different choices of $\frac{\sigma_\uparrow}{N_\uparrow D_\uparrow}$ and $\frac{\sigma_\downarrow}{N_\downarrow D_\downarrow}$, and the magnitudes of the spin signals are of the order of magnitude of the chemical potential split.

6.3.3 Specific Examples of Non-inverted and Inverted Large Spin Signals

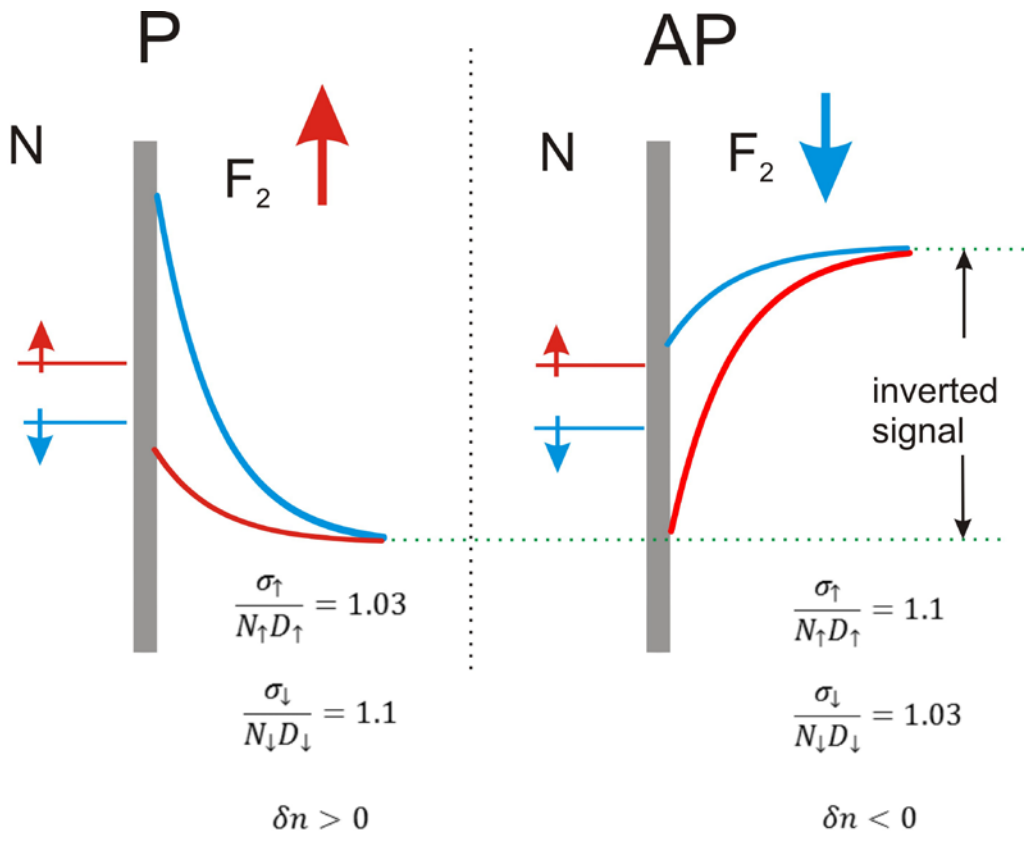

Figure 6.8: The profiles of $\boldsymbol{u_{ecp1\uparrow}}$ (red) and $\boldsymbol{u_{ecp1\downarrow}}$ (blue) in F_2 for an inverted large spin signal.

Figure 6.8 shows a situation where $\frac{\sigma}{ND} = 1.03$ for the majority spin and $\frac{\sigma}{ND} = 1.1$ for the minority spin. The left panel of Figure 6.8 shows the profile of electro-chemical potentials when the magnetization of F_2 points up. In this case the spin-up is majority spin and spin-down is minority spin. Therefore $\frac{\sigma_\uparrow}{N_\uparrow D_\uparrow} = 1.03$ and $\frac{\sigma_\downarrow}{N_\downarrow D_\downarrow} = 1.1$. From Eq. 6.15, a positive charge accumulation $\delta n_{10} > 0$ is necessary in order to maintain the inverted chemical potential split $\Delta\mu_{ecp1} < 0$. From Eq. 6.16 and 6.17, $\mu_{ecp\uparrow}(x)$ and $\mu_{ecp\downarrow}(x)$ both decrease as x increases in the region where $x > 0$ and

converges to a common value *C* on the scale of charge screening length. This value represents the electric potential of the F_2 electrode in spin-up state (P state between F_1 and F_2).

The right panel of Figure 6.8 shows the profile of electro-chemical potentials when the magnetization of F_2 points down. In this case spin-down is the majority spin and spin-up is the minority spin. Therefore $\frac{\sigma_\uparrow}{N_\uparrow D_\uparrow} = 1.1$ and $\frac{\sigma_\downarrow}{N_\downarrow D_\downarrow} = 1.03$. From Eq. 6.15, a negative charge accumulation $\delta n_{10} < 0$ is necessary in order to achieve inverted chemical potential split $\Delta\mu_{ecp1} < 0$. In other words, the charge accumulation changes the sign compared to the situation in the left panel, where F_2 is aligned spin-up. As mentioned earlier, the charge accumulation δn_{10} is an additional degree of freedom to achieve the necessary chemical potential split that satisfies boundary conditions Eq. 6.18 and 6.19. Since $\delta n_{10} < 0$, $\mu_{ecp\uparrow}(x)$ and $\mu_{ecp\downarrow}(x)$ both increase as *x* increases in the region where $x > 0$, as indicated by Eq. 6.16 and 6.17. On the scale of the charge screening length, $\mu_{ecp\uparrow}(x)$ and $\mu_{ecp\downarrow}(x)$ converges to a common value C', which represents the electric potential of F_2 in the spin-down state (AP state between F_1 and F_2). The spin signal is the difference between the potentials of F_2 for spin-up and spin-down states: C' – C. In this case the spin signal has a negative value, and therefore it is an inverted spin signal. From Figure 6.8 and Eq. 6.15 – 6.17, it is obvious that the magnitude of this spin signal is of the order of the magnitude of the large chemical potential split at $x = 0^+$.

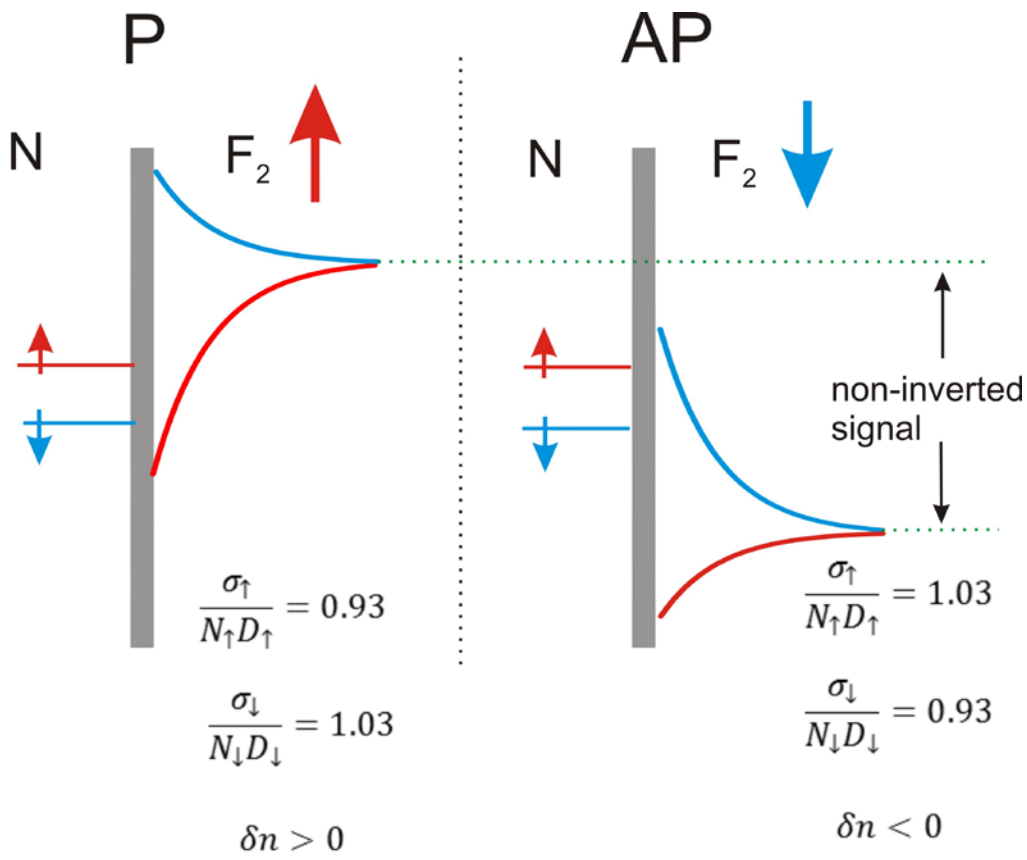

Figure 6.9: The profiles of $\boldsymbol{u_{ecp1\uparrow}}$ (red) and $\boldsymbol{u_{ecp1\downarrow}}$ (blue) for a non-inverted large spin signal.

Figure 6.9 shows a situation where a non-inverted spin signal is the consequence of the spin-charge coupling. Here $\frac{\sigma}{ND} = 0.93$ for majority spins and $\frac{\sigma}{ND} = 1.03$ for minority spins. The left panel of Figure 6.9 shows the profile of electro-chemical potentials when the magnetization of F_2 points up (P state between F_1 and F_2). In this case the spin-up is majority spin and spin-down is minority spin. Therefore $\frac{\sigma_\uparrow}{N_\uparrow D_\uparrow} = 0.93$ and $\frac{\sigma_\downarrow}{N_\downarrow D_\downarrow} = 1.03$. From Eq. 6.15, a positive charge accumulation $\delta n_{10} > 0$ is necessary in order to maintain the inverted chemical potential split $\Delta\mu_{ecp1} < 0$. From Eq. 6.16 and 6.17, $\mu_{ecp\uparrow}(x)$ increases and $\mu_{ecp\downarrow}(x)$ decreases as x increases in

the region where $x > 0$ and converges to a common value C on the scale of charge screening length.

The right panel of Figure 6.9 shows the profile of electro-chemical potentials when the magnetization of F_2 points down (AP sate between F_1 and F_2). In this case spin-down is the majority spin and spin-up is the minority spin. Therefore $\frac{\sigma_\uparrow}{N_\uparrow D_\uparrow} = 1.03$ and $\frac{\sigma_\downarrow}{N_\downarrow D_\downarrow} = 0.93$. From Eq. 6.15, a negative charge accumulation $\delta n_{10} < 0$ is necessary in order to achieve inverted chemical potential split $\Delta\mu_{ecp1} < 0$. Since $\delta n_{10} < 0$, $\mu_{ecp\uparrow}(x)$ increases and $\mu_{ecp\downarrow}(x)$ decreases as x increases in the region where $x > 0$, as indicated by Eq. 6.16 and 6.17 and shown in the right panel of Figure 6.9. On the scale of the charge screening length, $\mu_{ecp\uparrow}(x)$ and $\mu_{ecp\downarrow}(x)$ converges to a common value C'. The spin signal is C' – C and in this case it is a positive value. Therefore the spin signal is non-inverted. The magnitude of the spin signal is of the order of the magnitude of the chemical potential split at $x = 0^+$.

The signs and the exact magnitudes of the spin signals depend on the following quantities: $\left(\frac{\sigma_\uparrow}{N_\uparrow D_\uparrow} - 1\right)$, $\left(\frac{\sigma_\downarrow}{N_\downarrow D_\downarrow} - 1\right)$, $\left(\frac{\sigma_\uparrow}{N_\uparrow D_\uparrow} - \frac{\sigma_\downarrow}{N_\downarrow D_\downarrow}\right)$, $R_{i\uparrow}$ and $R_{i\downarrow}$. Different combinations of these quantities result in both non-inverted and inverted spin signals. It would be tedious to list all the possibilities for different combinations of theses quantities. We only try to illustrate that both non-inverted and inverted spin signals are possible and the magnitude of the spin signals is large for a highly resistive N/F_2 barrier.

In Figure 6.9, the average of the electrochemical potentials for P and AP states at $x = +\infty$ is different from the electrochemical potential at $x = -\infty$. This implies a non-zero baseline for the spin signals due to the charge accumulation. Furthermore, the curving of electrochemical potentials over the charge screening length ($\lambda \sim 0.1$ nm)

could also occur in the N metal if $\frac{\sigma}{ND}$ (not spin-dependent) differs from 1 in N near the interface. This introduces an additional large baseline voltage.

6.4 Conclusion

A large spin accumulation signal across a highly resistive break-junction has been demonstrated in a nonlocal spin valve. The magnitude of spin signal is substantially larger than those in regular nonlocal spin valves. The signs of the spin signal can be either inverted or non-inverted. Experimental efforts are made to rule out the possibility of spurious effects. A theoretical model of spin-charge coupling is used to account for the large magnitudes and signs. Due to the coupling of spin accumulation and charge accumulation, a large chemical potential split is present near the break-junction interface resulting in a large spin signal. The signs of the spin signal depend on the spin-dependent values of conductivity, diffusion constant, and density of states. In the future, we will set up a LabVIEW program for forming the break-junction from itinerate method by electro-migration. This will produce the break-junction automatically, which will increase the productivity and allow more systematically research on it.

REFERENCES

[1] S. A. Wolf, D. D. Awschalom, R. A. Buhrman, *et al*., Science, **294**, 1488 (2001).

[2] I. Zutic, J. Fabian, and S. Das Sarma, Review of Modern Physics, **76**, 323 (2004).

[3] D. C. Ralph and M. D. Stiles, Journal of Magnetism and Magnetic Materials, **320**, 1190 (2008).

[4] T. Jungwirth, J. Wunderlich, and K. Olejnik, Nature Materials, **11**, 382 (2012).

[5] G. E. W. Bauer, E. Saitoh, and B. J. van Wees, Nature Materials, **11**, 391 (2012).

[6] M. Johnson and R. H. Silsbee, Physical Review Letters, **55**, 1790 (1985).

[7] M. Johnson, Physical Review Letters, **70**, 2142 (1993).

[8] F. J. Jedema, H. B. Heersche, A. T. Filip *et al*., Nature, **416**, 713 (2002).

[9] T. Kimura, J. Hamrle, Y. Otani, *et al*., Applied Physics Letters, **85**, 3501 (2004).

[10] S. O. Valenzuela and M. Tinkham, Applied Physics Letters, **85**, 5914 (2004).

[11] Y. Ji, A. Hoffmann, J. S. Jiang, and S. D. Bader, Applied Physics Letters, **85**, 6218 (2004).

[12] S. Garzon, I. Zutic, and R. A. Webb, Physical Review Letters, **94**, 176601 (2005).

[13] R. Godfrey and M. Johnson, Physical Review Letters, **96**, 136601 (2006).

[14] X. H. Lou, C. Adelmann, S. A. Crooker, *et al*., Nature Physics, **3**, 197 (2007).

[15] O. M. J. van't Erve, A. T. Hanbicki, M. Holub, *et al*., Applied Physics Letters, **91**, 212109 (2007).

[16] M. Johnson and R. H. Silsbee, Physical Review B, **37**, 5312 (1988).

[17] F. J. Jedema, M. S. Nijboer, A. T. Filip, and B. J. Van Wees, Physical Review B, **67**, 085319 (2003).

[18] S. Takahashi and S. Maekawa, Physical Review B, **67**, 052409 (2003).

[19] H. Zou, S. T. Chui, X. J.Wang, and Y. Ji, Physical Review B, **83**, 094402 (2011).

[20] Y. Ji, A. Hoffmann, J. E. Pearson, and S. D. Bader, Applied Physics Letters, **88**, 052509 (2006).

[21] X. J. Wang, H. Zou, L. E. Ocola, and Y. Ji, Applied Physics Letters, **95**, 022519 (2009).

[22] Y. Ji, A. Hoffmann, J. S. Jiang, J. E. Pearson, *et al*., Journal of Physics D: Applied Physics, **40**, 1280 (2007).

[23] S. O. Valenzuela, D. J. Monsma, C. M. Marcus, *et al*., Physical Review Letters, **94**, 196601 (2005).

[24] H. Park, A. K. L. Lim, A. P. Alivisatos, *et al*., Applied Physics Letters, **75**, 301 (1999).

[25] D. R. Strachan, D. E. Smith, D. E. Johnston, *et al*., Applied Physics Letters, **86**, 043109 (2005).

[26] K. I. Bolotin, F. Kuemmeth, A. N. Pasupathy, and D. C. Ralph, Nano Letters, **6**, 123 (2006).

[27] M. Johnson and R. H. Silsbee, Physical Review B, **76**, 153107 (2007).

[28] X. J. Wang, H. Zou, and Y. Ji, Physical Review B, **81**, 104409 (2010).

[29] S. T. Chui and Z. F. Lin, Physical Review B, **77**, 094432 (2008).

[30] S. T. Chui, "*Multiple magnetic tunnel junctions*", U.S. patent 5757056, May 26, 1998.

Chapter 7

EFFICIENT ROOM TEMPERATURE SPIN-HALL INJECTION ACROSS AN OXIDE BARRIER

7.1 Introduction

For the past several decades, spin injection requires a ferromagnetic material which polarizes an electric current. Recently, spin Hall effect (SHE) [1-5] has drawn great attention since a spin polarized current can be generated by spin-orbit coupling in heavy nonmagnetic materials such as platinum without any ferromagnetic materials. By spin torque, the spin current due to SHE in metals can be as large as to switch the magnetization of an adjacent ferromagnetic layer. [6, 7]

Electrical measurements of SHE and its reciprocal process, inverse spin Hall effect (ISHE), have been demonstrated in mesoscopic metallic nonlocal structures. [5, 8-10] Macroscopic bilayer thin films of a heavy nonmagnetic metal and a magnetic metal have also been used for a variety of experiments related to SHE/ISHE. These include microwave pumping of spin currents and ISHE, [11, 12] ferromagnetic resonance induced by SHE, [13, 14] and magnetization reversal due to spin Hall torques. [6, 7, 15] It is widely acknowledged that the nonlocal structure avoids direct contact between the magnetic material and the heavy metal, eliminating possible proximity effects [16], current shunting and other unknown physical phenomena even the bilayer structure is simple, robust and efficient. In addition, probing SHE/ISHE on mesoscopic dimensions reduce the non-uniformity of the effects over a large area.

In previous works, the spin current generated in the heavy nonmagnetic metal is delivered into the adjacent layer (either a magnetic layer or a nonmagnetic channel) across an ohmic interface. The rationale is that an interface with lower resistance accommodates a higher spin current for a fixed amount of spin accumulation difference across the interface. In this chapter, we show that the spin injection by the SHE across a thin AlO_x barrier can also be efficient in nonlocal spin valves (NLSVs). The nonlocal spin signal due to the SHE injection is substantial and comparable to that of the conventional electrical spin injection from a ferromagnet, thereby enabling an efficient scheme of spin Hall injection across oxide barriers. Since oxide layers are widely used as tunnel barriers in spintronics, this feasibility expands the potentials of SHE and enables the integration of SHE materials into existing spintronic technologies.

The estimates of the spin Hall angle, a characteristic parameter for the SHE, are not without controversy from previous works. [17] Here we develop a systematic method to quantify the spin Hall angle in the SHE/ISHE structure by using standard NLSV [18-23] fabricated under identical conditions in the same batch. The spin polarization of the Py/AlO_x/Cu interfaces, the spin diffusion length of Cu, and spin absorption coefficient of Cu/AlO_x/Pt interfaces can be determined from NLSV structures and then used to extract the spin Hall angle in the SHE/ISHE structure. All measurements have been carried out at room temperature. This method can be popularized as a universe method for quantifying spin Hall angle and spin absorption rate.

7.2 Experiments and Measurements

7.2.1 Sample Fabrication and Regular NLSV Measurements

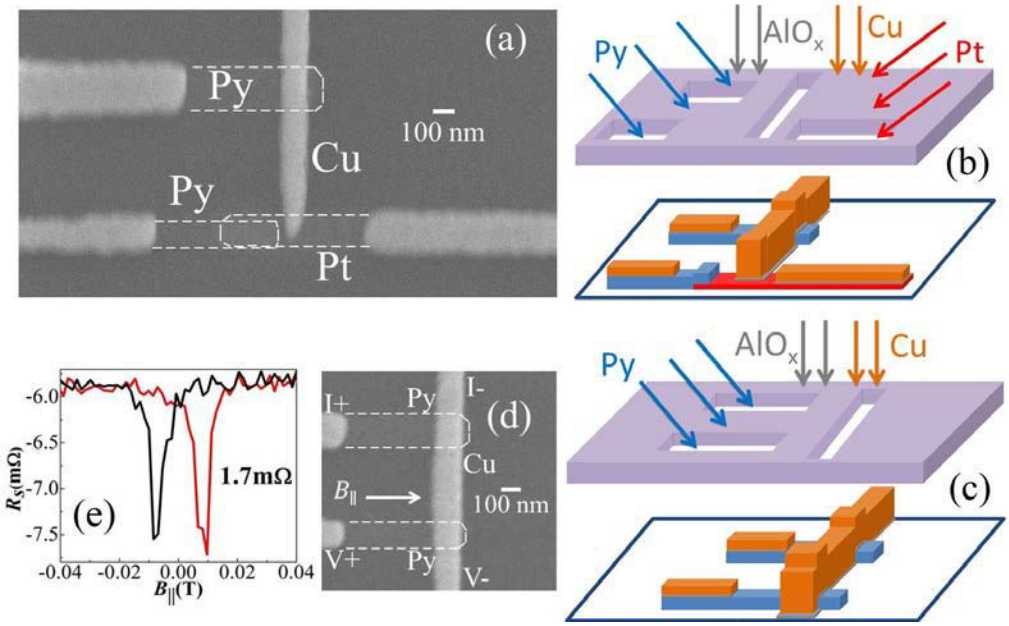

Figure 7.1: (a) SEM picture of a mesoscopic SHE/ISHE structure; (b) angle evaporation of the SHE/SHE structure through a shadow mask; (c) angle evaporation of a NLSV structure through a shadow mask; (d) SEM picture of a NLSV structure; (e) R_s versus B curve for the NLSV.

We fabricated both SHE/ISHE devices and regular NLSVs under the identical conditions, with same procedures on the same substrate. Figure 7.1 (a) is a scanning electron microscope (SEM) picture of the SHE/ISHE structure. The Py and Pt wires are relatively thin and the outlines are marked by the dashed lines for clarity. The upper Py wire in Figure 7.1 (a) is used as a spin injector for the ISHE and as a spin detector for the SHE. The lower Py wire in Figure 7.1 (a) simply serves an electrical contact to the Pt wire, which extends underneath the Cu channel and generates the SHE/ISHE.

The structure is fabricated by evaporation of several materials through a nanoscale shadow mask from different angles, [24, 25] as illustrated in Figure 7.1 (b). The mask is produced by electron beam lithography on two layers of resists with different sensitivities to electron beam dosage. [24] As shown in Figure 7.1 (b), 6 nm Pt, 15 nm Py, 3 nm AlO_x and 110nm Cu are deposited in this sequence through the shadow mask from different angles to form the structure without breaking the vacuum.

For quantitative analysis of the SHE/ISHE structure, a standard NLSV is deposited simultaneously with the SHE/ISHE structure through an additional shadow mask on the same substrate, as shown in Figure 7.1 (c). Therefore the materials and interfaces of the two structures are formed under identical conditions. Figure 7.1 (d) shows the SEM picture of the NLSV, which consists of a Cu (110 nm) channel, a Py (15 nm) spin injector, a Py (15 nm) spin detector, and AlO_x (3 nm) barriers at both Py/Cu interfaces.

Here we discuss the measurement of the regular NLSV first. It is measured by a standard nonlocal measurement configuration as we discussed before [22, 24]. The nonlocal spin resistance $R_s = V/I$ versus the magnetic field B is shown in Figure 7.1(e). The spin signal ΔR_s, the difference of R_s between the parallel (P) and antiparallel (AP) states of injector and detector is 1.7 mΩ. The ΔR_s is described as $\Delta R_s = (P_1 P_2 \rho_{cu} \lambda_{cu}/A) e^{-\frac{L}{\lambda_{cu}}}$, [26] where P_1 and P_2 are the spin polarizations of the two Py/AlO_x/Cu interfaces, λ_{cu} is the spin diffusion length of the Cu channel, ρ_{cu} is the resistivity of the Cu, L is the distance between the injector and the detector, and A is the cross-sectional area of the Cu channel. For this NLSV, L = 500 nm, A = 150 × 110 nm^2, and ρ = 3.7 μΩ•cm. We typically assume that $P_1 = P_2 = P$ since the two Py/AlO_x/Cu interfaces have comparable dimensions and fabricated under same

conditions. From our previous work, [25, 27] 260 nm < λ_{cu} < 300 nm is a reasonable range for Cu. Restrained by ΔR_s = 1.7 mΩ, either λ_{cu} = 260 nm and P = 14.1% or λ_{cu} = 300 nm and P = 11.5% are valid estimates. These two sets of parameters give similar spin Hall angle estimates for Pt in the SHE/ISHE structure as we will show later.

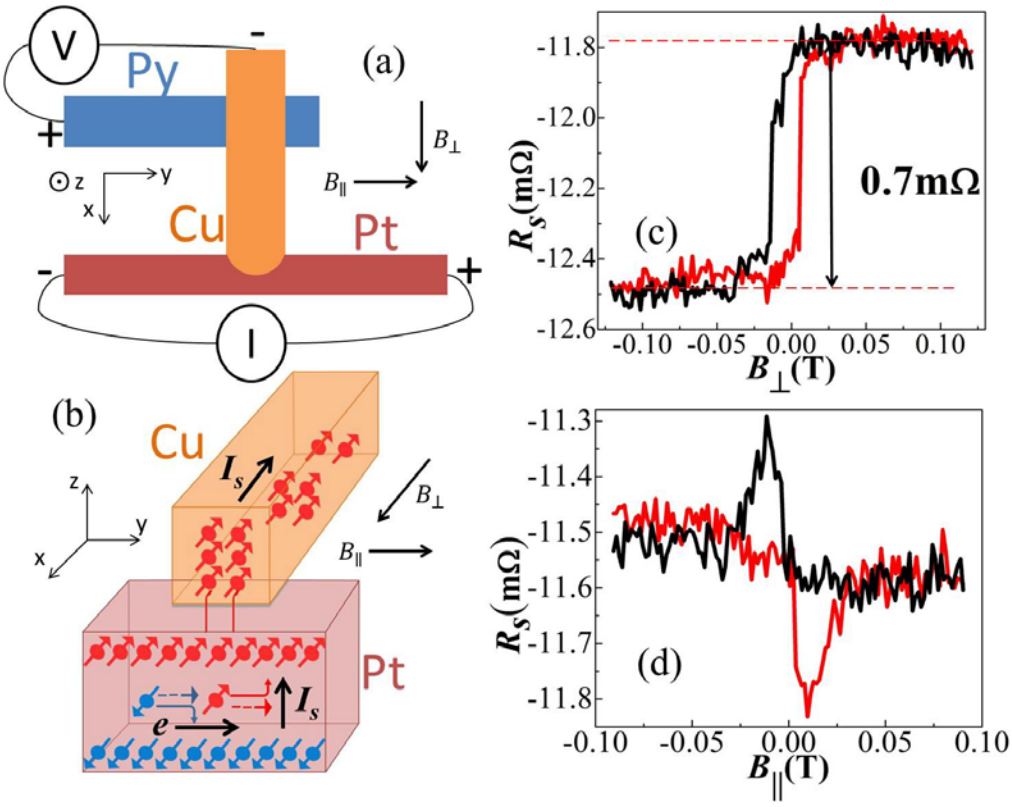

Figure 7.2: (a) Measurement configuration for SHE; (b) distribution of spins (spin moments) throughout the structure; (c) R_s versus B curve with field applied along x axis; (d) R_s versus B curve with field applied along y axis.

7.2.2 SHE Measurement Set-up and Results

The SHE measurement configuration is shown in Figure 7.2 (a). An a.c. current I of 100μA at 346Hz is passed through the Pt wire, and a voltage V is measured

by lock-in detector between the Py wire and the Cu channel. Figure 7.2 (b) illustrates the distribution of spin accumulation in the SHE/ISHE structure, when a charge current *I* (with current density J_c) flows in the Pt along the -*y* direction. Electrons flow in the + *y* direction, and opposite spins (spin moments) are scattered in opposite transverse direction due to spin-orbit coupling: +*x* spins are scattered toward –*z* direction and –*x* spins toward + *z* direction. As a result, –*x* spins accumulates on the top surface and +*x* spins accumulates on the bottom surface of Pt. This is equivalent to a transverse spin current density along the z direction $J_s = \alpha_{SHE} J_c$, where α_{SHE} is the spin Hall angle. In the open circuit situation, this spin current is eventually balanced by the opposite spin current driven by the spin accumulation on Pt surfaces.

The spin accumulation on the Pt top surface also drives spins across the AlO_x barrier into the Cu. The spins in the Cu channel is detected as a ΔR_s when the Py spins and the spins in Cu vary between P and AP states (Because of pure spin current, there should be blue spin current decays along +*x* direction in Cu channel. We did not denote it here to avoid crowding.). A magnetic field ($B_\perp$) is applied perpendicular to the longitudinal direction of Py wires to sweep the Py spins between the +*x* and –*x* directions, which is required for better capturing the spin accumulation in Cu channel. A spin signal ΔR_s = 0.7 mΩ is observed as shown in Figure 7.2 (c).

The measurement in Figure 7.2 (d) is carried out using magnetic fields ($B_\parallel$) along ±y and an asymmetric hysteresis loop is plot out as the measurement result. The change of R_s is only seen near the reversal fields of the Py wire. When saturated along ±*y*, the Py spins are perpendicular to the spins in Cu. Therefore a full reversal (magnetization lies in the sample plane) between +*y* and –*y* does not yield a change of R_s. However, near the reversal fields, the magnetization gradually rotates and develops

an *x* component leading to variations of R_s (Note that the spin orientation in Cu is always parallel to x-axis and only depends on the SHE in Pt rather than the applied field.). Since the Py magnetization is never fully along –*x* or + *x*, the ΔR_s of 0.5 mΩ is smaller than the full 0.7 mΩ in Figure 7.2 (c). The ratio of the two values should be the cosine of the minimum angle, estimated ~ 45°, between the Py magnetization and the x axis.

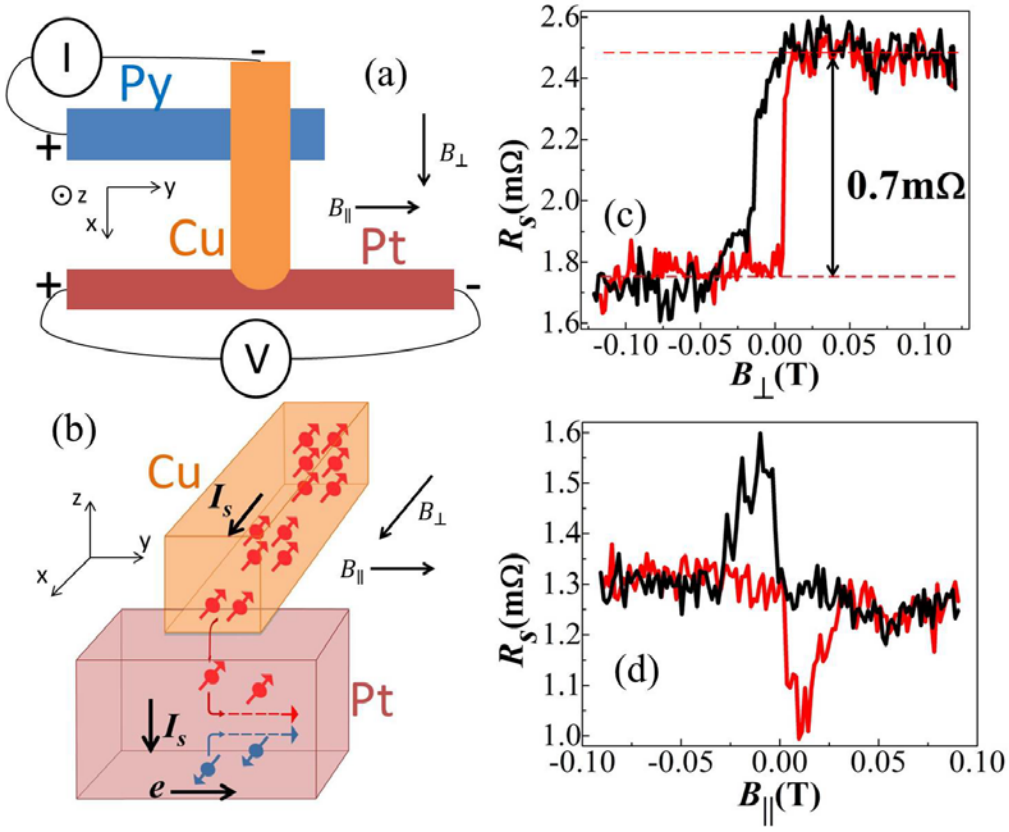

Figure 7.3: (a) Measurement configuration for the ISHE; (b) distribution of spins throughout the structure; (c) R_s versus *B* curve with field applied along x axis; (d) R_s versus *B* curve with field applied along y axis.

7.2.3 ISHE Measurement Set-up and Results

The measurement configuration for ISHE is shown in Figure 7.3 (a). An a.c. current *I* of 100μA at 346Hz flows from the Py wire into the Cu channel, thereby inducing a spin accumulation in the Cu and a pure spin current along +*x*. The voltage is measured between the two ends of the Pt wire. The spins in the structure is illustrated in Figure 7.3 (b) for magnetic field ($B_\perp$) applied along +*x*. At the lower end of the Cu channel a fraction of the pure spin current is absorbed by the Pt and the rest is reflected back toward –*x*. The absorbed pure spin current flows across the Cu/AlO_x/Pt interface along –*z*, and can be seen as –*x* spins moving along –*z* direction and +*x* spins moving along +*z* direction (Because of pure spin current, there should be blue spin current decays along –*x* direction in Cu channel. We did not denote it here to avoid crowding.). Due to spin-orbit scattering, both spins are scattered toward +*y* direction, inducing a charge current. As the reciprocal of the SHE, the ISHE converts a spin current J_s into a transverse charge current $J_c = \alpha_{SHE} J_s$, where α_{SHE} is the same spin Hall angle as in the SHE. The charge current gives rise to a charge voltage between two ends of Pt, which eventually suppresses the charge current.

When the external field ($B_\perp$) sweeps the Py magnetization from +*x* to – *x*, the injected spins in Cu change from –*x* to +*x* and the sign of the charge voltage across the Pt wire changes. This has been observed in the R_s versus *B* curve in Figure 7.3 (c), where a positive field leads to a high R_s state and negative field induces a low R_s state. The ISHE spin signal is ΔR_s = 0.7 mΩ, the same as the ΔR_s in the SHE due to the Onsager reciprocal relationship of the two effects. When the external field ($B_\parallel$) is applied along ±*y* and polarizes injected spins along ±*y*, no transverse charge voltage along the Pt wire (parallel to *y* axis) is expected in the saturated states, as is the case in

Figure 7.3 (d). Similar to the SHE measurement in Figure 7.2 (d), change of R_s is only seen near the Py reversal fields.

The ΔR_s of 0.7 mΩ is substantially higher than previous SHE/ISHE measurements in nonlocal structures. [8, 9, 28, 29] It is noteworthy that the 0.7 mΩ in the SHE/ISHE structure is 40% of the 1.7 mΩ, comparable with that in the NLSV structure in Figure 7.1 (e), which indicates that the SHE can be an efficient way for spin injection as regular electric injection.

7.3 Discussion of Results: Estimation of Spin Hall Angle

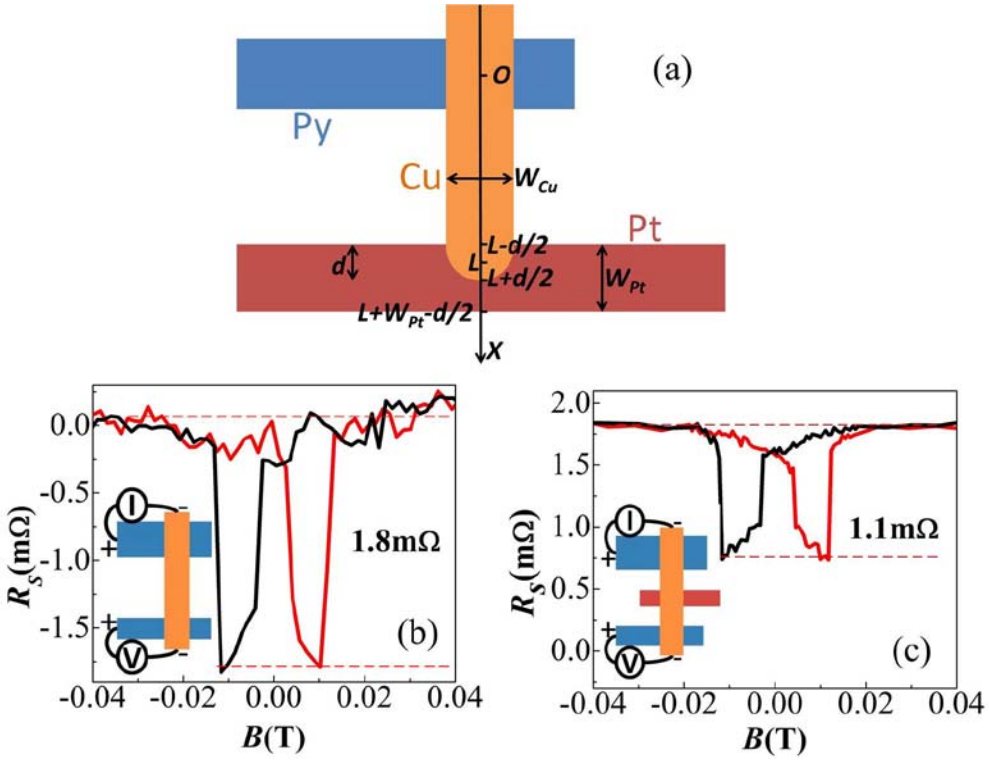

Figure 7.4: (a) Dimensions of the SHE/ISHE structure; (b) R_s versus B curve for a standard NLSV showing a spin signal of 1.8 mΩ; a cartoon of the structure is shown in the inset; (c) R_s versus B curve for a NLSV with a Pt wire under the Cu channel showing a spin signal of 1.1 mΩ; a cartoon of the structure is shown in the inset.

In the following, we will show that the large signal is due to a large spin Hall angle and a large spin absorption coefficient of the Cu/AlO_x/Pt interface. According to conventions, we define SHE and ISHE signal as $\Delta R_{SHE} = \Delta R_s/2 = 0.35\ m\Omega$ for the following analysis.

The analysis [30] is relevant to the dimensions illustrated in Figure 7 4 (a). In the context of ISHE, the pure spin current in Cu along +x is $I_s = \frac{1}{2} P I e^{-\frac{L}{\lambda_{cu}}}$ upon arriving at the Cu/AlO_x/Pt interface. A fraction (γ) of the spin current I_s is absorbed into the Pt and the rest is reflected back toward –*x*, and γ is known as the spin absorption coefficient [31] of the interface. The shape of the Cu/AlO_x/Pt interface is near triangular due to the tapering end of the Cu channel. The width of Pt is w_{pt} and the width of Cu channel is $w_{cu}(x)$, which varies near the end of the channel. The overlapping depth between Pt and Cu is *d*. The area of the junction is $A_j = \int_{L-d/2}^{L+d/2} w_{Cu}(x)dx$. We assume the spin current is absorbed across the interface uniformly with a spin current density of $\gamma\, I_s/A_j$. The charge voltage due to the ISHE depends on *x*: $v_H(x) = \gamma \alpha_H w_{Cu}(x) \rho_{pt} \left(I_s/A_j\right)$. [30] The average voltage over *x* is $V_H' = \gamma \alpha_H \rho_{pt} \left(I_s/A_j\right) \int_{L-d/2}^{L+d/2} \frac{w_{Cu}(x)dx}{d} = \gamma \alpha_H \rho_{pt} I_s/d$. The measured voltage is scaled down by a factor of d/w_{pt} due to the shunting effect of the Pt at $x > L + d/2$, and therefore $V_H = I\Delta R_{SHE} = \gamma \alpha_H \rho_{pt} I_s/w_{pt}$. This voltage is independent of overlap depth *d* and the form of $w_{Cu}(x)$. Substituting the expression of I_s, we obtain

$$\gamma \alpha_H = \frac{2\Delta R_{SHE} w_{pt}}{\rho_{pt} P} e^{\frac{L}{\lambda_{cu}}} \qquad (7.1).$$

In this sample, $w_{Pt} = 130\ nm$, *L* = 557 nm, and the Pt resistivity $\rho_{pt} = 26\ \mu\Omega \cdot cm$. Using *P* = 11.5% and $\lambda_{Cu} = 300\ nm$ from the NLSV estimates, the signal ΔR_{SHE} = 0.35 mΩ yields $\gamma \alpha_H = 0.0195$. Using *P* = 14.1% and λ_{cu} = 260 nm,

we obtain $\gamma\alpha_H = 0.0211$. Two values are close and we conclude $\gamma\alpha_H = 0.020 \pm 0.003$, where the uncertainty is mainly due to resistivity and dimension measurements.

For determination of γ, spin absorption coefficient, we adapt Kimura's spin absorption method [9, 31] as shown in Figure 7.4 (b) and (c). Two NLSV structures, a standard NLSV (Fig. 7.4(b)) and a NLSV with a Pt inserted between injector and detector (Fig. 7.4(c)), are fabricated in the same batch. After adjusted by the 10% for the difference of Cu channel widths, the ratio of two spin signals is $\eta = 0.67 \pm 0.03$. Using one-dimensional diffusion equations with matched boundary conditions, a relationship between γ and η can be established as $\gamma = 2(1-\eta) = 0.66 \pm 0.06$. Then the spin Hall angle $\alpha_H = 0.030 \pm 0.007$. Note that we have assumed Pt spin diffusion length $\lambda_{pt} > 6$ nm.

In the context of the SHE, a charge current I in Pt, with a current density of $j_c = I/t_{pt}w_{pt}$, gives rise to a transverse spin current density $j_s = \alpha_H j_c = \frac{\alpha_H I}{t_{pt}w_{pt}}$, where t_{pt} is the thickness of the Pt wire. Assuming that $\lambda_{pt} > t_{pt} = 6\ nm$, the spin accumulation on the top surface is $\Delta\mu_0 = j_s t_{pt}\rho_{pt} = \left(\alpha_H I\rho_{pt}\right)/w_{pt}$. The spin accumulation in Cu can be described as $\gamma'\Delta\mu_0$, and γ' is the transfer rate of spin accumulation from Pt into Cu. The spins in the Cu channel decays over distance and is detected as a nonlocal voltage change: $\frac{P\gamma'\alpha_H I\rho_{pt}}{w_{pt}} e^{-\frac{L}{\lambda_{cu}}} = 2\Delta V_H$. From this it follows that

$$\gamma'\alpha_H = \frac{2\Delta R_{SHE} w_{pt}}{P\rho_{pt}} e^{\frac{L}{\lambda_{cu}}} \qquad (7.2).$$

Comparing Eq (7.1) and (7.2) we have $\gamma = \gamma'$, which indicates the spin absorption efficiency and the transfer rate of spin accumulation are the same. Then this leads to the previous conclusion that $\gamma\alpha_H = 0.020 \pm 0.003$. With the measured value $\gamma = 0.66 \pm 0.06$, it follows that $\alpha_H = 0.030 \pm 0.007$.

We assume the spin diffusion length $\lambda_{pt} > t_{pt} = 6\ nm$ in the above SHE/ISHE analysis. When λ_{pt} < 6 nm, only a depth of λ_{pt} in the 6 nm Pt film is efficiently used for the ISHE/SHE and therefore the α_H is underestimated by a factor of λ_{pt}/t_{pt}. If we assume $\lambda_{pt} = 2\ nm$, then $\alpha_H = 0.09 \pm 0.02$, which is very close to previous measurement results by spin-pumping. [32] As a comparison, recent measurements of Pt spin Hall angle ranges from 0.01 to 0.07. [6, 12, 13, 14, 33-35]

The spin absorption coefficient of 0.66 ± 0.06 for the Cu/AlO_x/Pt interface is not well explained by existing theories. The resistance of such interfaces is 80 Ω - 400 Ω as measured in similar structures using four-probe method. Kimura *et al.* [31] defined spin resistances for metals and have shown that a spin current is absorbed efficiently from a metal with larger spin resistance into a metal with a smaller spin resistance. Since the Cu spin resistance (~ 0.8 Ω) is much larger than that of Pt (~ 0.1 Ω), γ is large for transparent Cu/Pt interfaces. [9] However, the resistance of AlO_x barrier is 10^2 times of the Cu spin resistance. Therefore > 99% of the spin current should be reflected by the AlO_x barrier and γ < 0.01. Thus the origin of large γ still needs further theoretical and experimental investigations. Recently, the resistivity of Py strip has been revealed to much higher than bulk materials, which may result in a much higher nonlocal voltage. It is also found out that SHA is related to the thickness and geometrical dimension of Pt from recent research.

7.4 Conclusion

In conclusion, both direct spin Hall effects and inverse spin Hall effects have been observed in mesoscopic structures with a Pt wire and a Cu channel. The spin accumulation from the Pt wire due to the spin Hall effect is injected across an AlO_x barrier into the Cu channel, and the magnitude is comparable to that of a conventional

electrical spin injection from a ferromagnet. We quantify the system using a spin Hall angle α_H of the Pt and a spin accumulation transfer rate γ for the Cu/AlO_x/Pt interface. The demonstrated large spin Hall angle of Pt and large spin accumulation transfer rate of AlO_x are promising for spintronic applications. For future work, various materials' SHA can be characterized by this method, such as Au, Ta, Nb, etc. Also, the origin of effective spin injection through low resistive oxide AlO_x barrier needs more study to understand. The so called shunting effect should also be evaluated based on a more comprehensive analysis.

REFERENCES

[1] J. E. Hirsch, Physical Review Letters, **83**, 1834 (1999);

[2] S. F. Zhang, Physical Review Letters, **85**, 393 (2000);

[3] Y. K. Kato, R. C. Myers, A. C. Gossard, and D. D. Awschalom, Science, **306**, 1910 (2004);

[4] A. Hoffmann, IEEE Transactions, Magnetics, **49**, 5172 (2013).

[5] S. O. Valenzuela and M. Tinkham, Nature, **442**, 176 (2006).

[6] L. Q. Liu, O. J. Lee, T. J. Gudmundsen, *et al*., Physics Review Letters, **109**, 096602 (2012).

[7] L. Q. Liu, C. F. Pai, Y. Li, *et al*., Science, **336**, 555 (2012).

[8] T. Kimura, Y. Otani, T. Sato, *et al*., Physical Review Letters, **98**, 156601 (2007).

[9] L. Vila, T. Kimura, and Y. Otani, Physical Review Letters, **99**, 226604 (2007).

[10] T. Seki, Y. Hasegawa, S. Mitani, *et al*., Nature Materials, **7**, 125 (2008).

[11] E. Saitoh, M. Ueda, H. Miyajima, and G. Tatara, Applied Physics Letters, **88**, 182509 (2006).

[12] O. Mosendz, J. E. Pearson, F. Y. Fradin, *et al*., Physics Review Letters, **104**, 046601 (2010).

[13] K. Ando, S. Takahashi, K. Harii, *et al*., Physical Review Letters, **101**, 036601 (2008);

[14] L. Q. Liu, T. Moriyama, D. C. Ralph, and R. A. Buhrman, Physical Review Letters, **106**, 036601 (2011).

[15] I. M. Miron, G. Gaudin, S. Auffret, *et al*., Nature Materials, **9**, 230 (2010).

[16] S. Y. Huang, X. Fan, D. Qu, *et al*., Physical Review Letters, **109**, 107204 (2012).

[17] L. Q. Liu, R. A. Buhrman, and D. C. Ralph, e-print arXiv:1111.3702.

[18] M. Johnson and R. H. Silsbee, Physical Review Letters, **55**, 1790 (1985);

[19] F. J. Jedema, A. T. Filip, and B. J. van Wees, Nature, **410**, 345 (2001);

[20] F. J. Jedema, H. B. Heersche, A. T. Filip, *et al*., Nature, **416**, 713 (2002);

[21] S. O. Valenzuela and M. Tinkham, Applied Physics Letters, **85**, 5914 (2004);

[22] Y. Ji, A. Hoffmann, J. S. Jiang, and S. D. Bader, Applied Physics Letters, **85**, 6218 (2004);

[23] T. Kimura, J. Hamrle, Y. Otani, *et al.*, Applied Physics Letters, **85**, 3501 (2004).

[24] Y. Ji, A. Hoffmann, J. E. Pearson, and S. D. Bader, Applied Physics Letters, **88**, 052509 (2006).

[25] H. Zou and Y. Ji, Applied Physics Letters, **101**, 082401 (2012).

[26] M. Johnson, Physical Review Letters, **70**, 2142 (1993).

[27] X. J. Wang, H. Zou, and Y. Ji, Physical Review B, **81**, 104409 (2010).

[28] Y. Niimi, M. Morota, D. H. Wei, *et al*., Physical Review Letters, **106**, 126601 (2011);

[29] Y. Niimi, Y. Kawanishi, D. H. Wei, *et al*., Physical Review Letters, **109**, 156602 (2012).

[30] S. Takahashi and S. Maekawa, Science and Technology: Advanced Materials, **9**, 014105, (2008).

[31] T. Kimura, J. Hamrle, and Y. Otani, Physical Review B, **72**, 014461 (2005).

[32] W. Zhang, V. Vlaminck, J. E. Pearson, *et al*., Applied Physics Letters, 103, 242414 (2013)

[33] Z. Feng, J. Hu, L. Sun, *et al*., Physical Review B, **85**, 214423, (2012);

[34] O. Mosendz, V. Vlaminck, J. E. Pearson, *et al*., Physical Review B, **82**, 214403 (2010);

[35] M. Morota, Y. Niimi, K. Ohnishi, Physical Review B, **83**, 174405 (2011).

Appendix A

REPRINT PERMISSION LETTERS

Reprint Permission for Chapter 2.3.1:

Hi Shuhan,

Sorry for the delaying of the response. Please cite my part as you need for the dissertation.

Regards,
Xiaojun

Reprint Permission for Chapter 3.1.2:

Hi Shuhan,

Yes, you have my permission to cite my dissertation.

Regards,
Han

Han Zou, Ph.D.
Reader Design
HGST, a Western Digital company

Reprint Permission for Figure 2.5 (a):

Dear Shuhan Chen,

Congratulations on the imminent completion of your doctoral degree. I'm pleased to learn that my past research has been of help to you and Prof. Ji. Of course you have my permission to re-use Figure 1(c). Please contact me if you have a permissions form that requires my signature.

Sincerely yours,

Mark

Mark Johnson, Ph. D.

Materials Physics, NRL

American Physical Society
License Details

Oct 26, 2015

This is an Agreement between Shuhan Chen ("You") and American Physical Society ("Publisher"). It consists of your order details, the terms and conditions provided by American Physical Society, and the payment instructions.

License Number	3736611496983
License date	Oct 26, 2015
Licensed content publisher	American Physical Society
Licensed content publication	Physical Review Letters
Licensed content title	Interfacial charge-spin coupling: Injection and detection of spin magnetization in metals
Licensed copyright line	Copyright © 1985, American Physical Society
Licensed content author	Mark Johnson and R. H. Silsbee
Licensed content date	Oct 21, 1985
Volume number	55
Type of Use	Thesis/Dissertation
Requestor type	Student
Format	Print, Electronic
Portion	chart/graph/table/figure
Number of charts/graphs/tables/figures	1
Portion description	Figure 1 (c)
Rights for	Main product
Duration of use	Life of current edition
Creation of copies for the disabled	no
With minor editing privileges	no
For distribution to	Worldwide
In the following language(s)	Original language of publication
With incidental promotional use	no

The lifetime unit quantity of new product	0 to 499
The requesting person/organization is:	Shuhan Chen/University of Delaware
Order reference number	None
Title of your thesis / dissertation	PURE SPIN CURRENT IN LATERAL STRUCTURES
Expected completion date	Dec 2015
Expected size (number of pages)	170
Total	0.00 USD

Reprint Permission for Figure 2.5 (b):

Dear Shuhan Chen

You have my permission.
Best regards
Bart van Wees

NATURE PUBLISHING GROUP LICENSE
TERMS AND CONDITIONS

Oct 26, 2015

This is a License Agreement between Shuhan Chen ("You") and Nature Publishing Group ("Nature Publishing Group") provided by Copyright Clearance Center ("CCC"). The license consists of your order details, the terms and conditions provided by Nature Publishing Group, and the payment terms and conditions.

All payments must be made in full to CCC. For payment instructions, please see information listed at the bottom of this form.

License Number	3736620988329
License date	Oct 26, 2015
Licensed content publisher	Nature Publishing Group
Licensed content publication	Nature
Licensed content title	Electrical detection of spin precession in a metallic mesoscopic spin valve
Licensed content author	F. J. Jedema, H. B. Heersche, A. T. Filip, J. J. A. Baselmans and B. J. van Wees
Licensed content date	Apr 18, 2002
Volume number	416
Issue number	6882
Type of Use	reuse in a dissertation / thesis
Requestor type	academic/educational
Format	print and electronic
Portion	figures/tables/illustrations
Number of figures/tables/illustrations	1
High-res required	no
Figures	Figure 1 (a)
Author of this NPG article	no
Your reference number	None
Title of your thesis / dissertation	PURE SPIN CURRENT IN LATERAL STRUCTURES
Expected completion date	Dec 2015
Estimated size (number of pages)	170
Total	0.00 USD

Reprint Permission for Figure 2.7:

NATURE PUBLISHING GROUP LICENSE TERMS AND CONDITIONS

Oct 26, 2015

This is a License Agreement between Shuhan Chen ("You") and Nature Publishing Group ("Nature Publishing Group") provided by Copyright Clearance Center ("CCC"). The license consists of your order details, the terms and conditions provided by Nature Publishing Group, and the payment terms and conditions.

All payments must be made in full to CCC. For payment instructions, please see information listed at the bottom of this form.

License Number	3736621421418
License date	Oct 26, 2015
Licensed content publisher	Nature Publishing Group
Licensed content publication	Nature
Licensed content title	Direct electronic measurement of the spin Hall effect
Licensed content author	S. O. ValenzuelaandM. Tinkham
Licensed content date	Jul 13, 2006
Volume number	442
Issue number	7099
Type of Use	reuse in a dissertation / thesis
Requestor type	academic/educational
Format	print and electronic
Portion	figures/tables/illustrations
Number of figures/tables/illustrations	1
High-res required	no
Figures	Figure 2 (a)
Author of this NPG article	no
Your reference number	None
Title of your thesis / dissertation	PURE SPIN CURRENT IN LATERAL STRUCTURES
Expected completion date	Dec 2015
Estimated size (number of pages)	170
Total	0.00 USD

Reprint Permission for Figure 2.8:

Dear Dr. Shuhan Chen,

Thank you very much.

Of course, it is no problem.

Sincerely,

Takashi

American Physical Society
License Details

Oct 26, 2015

This is an Agreement between Shuhan Chen ("You") and American Physical Society ("Publisher"). It consists of your order details, the terms and conditions provided by American Physical Society, and the payment instructions.

License Number	3736630311920
License date	Oct 26, 2015
Licensed content publisher	American Physical Society
Licensed content publication	Physical Review Letters
Licensed content title	Room-Temperature Reversible Spin Hall Effect
Licensed copyright line	Copyright © 2007, American Physical Society
Licensed content author	T. Kimura et al.
Licensed content date	Apr 12, 2007
Volume number	98
Type of Use	Thesis/Dissertation
Requestor type	Student
Format	Print, Electronic
Portion	chart/graph/table/figure
Number of charts/graphs/tables/figures	1
Portion description	Figure 1 (a)
Rights for	Main product
Duration of use	Life of current edition
Creation of copies for the disabled	no
With minor editing privileges	no
For distribution to	Worldwide
In the following language(s)	Original language of publication
With incidental promotional use	no

The lifetime unit quantity of new product	0 to 499
The requesting person/organization is:	Shuhan Chen/University of Delaware
Order reference number	None
Title of your thesis / dissertation	PURE SPIN CURRENT IN LATERAL STRUCTURES
Expected completion date	Dec 2015
Expected size (number of pages)	170

Reprint Permission for Figure 2.9 (a):

NATURE PUBLISHING GROUP LICENSE TERMS AND CONDITIONS

Oct 26, 2015

This is a License Agreement between Shuhan Chen ("You") and Nature Publishing Group ("Nature Publishing Group") provided by Copyright Clearance Center ("CCC"). The license consists of your order details, the terms and conditions provided by Nature Publishing Group, and the payment terms and conditions.

All payments must be made in full to CCC. For payment instructions, please see information listed at the bottom of this form.

License Number	3736630782223
License date	Oct 26, 2015
Licensed content publisher	Nature Publishing Group
Licensed content publication	Nature
Licensed content title	Perpendicular switching of a single ferromagnetic layer induced by in-plane current injection
Licensed content author	Ioan Mihai Miron, Kevin Garello, Gilles Gaudin, Pierre-Jean Zermatten, Marius V. Costache, Stéphane Auffret
Licensed content date	Jul 31, 2011
Volume number	476
Issue number	7359
Type of Use	reuse in a dissertation / thesis
Requestor type	academic/educational
Format	print and electronic
Portion	figures/tables/illustrations
Number of figures/tables/illustrations	1
High-res required	no
Figures	Figure 1 (a)
Author of this NPG article	no
Your reference number	None
Title of your thesis / dissertation	PURE SPIN CURRENT IN LATERAL STRUCTURES
Expected completion date	Dec 2015
Estimated size (number of pages)	170

Reprint Permission for Figure 2.9 (b):

Dear Mr. Chen,

It is certainly fine with me that you use our figure as indicated below in your publication. As you note you will need to contact the Science publisher for this permission also.

Best regards

Robert Buhrman
John Edson Sweet Professor of Engineering
211 Clark Hall
Cornell University
Ithaca, NY 14853-3501
phone: 607-255-3732

THE AMERICAN ASSOCIATION FOR THE ADVANCEMENT OF SCIENCE LICENSE TERMS AND CONDITIONS

Oct 26, 2015

This is a License Agreement between Shuhan Chen ("You") and The American Association for the Advancement of Science ("The American Association for the Advancement of Science") provided by Copyright Clearance Center ("CCC"). The license consists of your order details, the terms and conditions provided by The American Association for the Advancement of Science, and the payment terms and conditions.

All payments must be made in full to CCC. For payment instructions, please see information listed at the bottom of this form.

License Number	3736650419323
License date	Oct 26, 2015
Licensed content publisher	The American Association for the Advancement of Science
Licensed content publication	Science
Licensed content title	Spin-Torque Switching with the Giant Spin Hall Effect of Tantalum
Licensed content author	Luqiao Liu, Chi-Feng Pai, Y. Li, H. W. Tseng, D. C. Ralph, R. A. Buhrman
Licensed content date	May 4, 2012
Volume number	336
Issue number	6081
Type of Use	Thesis / Dissertation
Requestor type	Scientist/individual at a research institution
Format	Print and electronic
Portion	Figure
Number of figures/tables	1
Order reference number	None
Title of your thesis / dissertation	PURE SPIN CURRENT IN LATERAL STRUCTURES
Expected completion date	Dec 2015
Estimated size(pages)	170
Total	0.00 USD

Reprint Permission for Figure 2.10:

Dear Shuhan,

You are very welcome to reuse any figure from my paper.

I think you don't need to contact the editor, as long as you have my agreement.

Good luck with ending your PhD,

Best regards,

Kevin

NATURE PUBLISHING GROUP LICENSE
TERMS AND CONDITIONS

Oct 26, 2015

This is a License Agreement between Shuhan Chen ("You") and Nature Publishing Group ("Nature Publishing Group") provided by Copyright Clearance Center ("CCC"). The license consists of your order details, the terms and conditions provided by Nature Publishing Group, and the payment terms and conditions.

All payments must be made in full to CCC. For payment instructions, please see information listed at the bottom of this form.

License Number	3736631242417
License date	Oct 26, 2015
Licensed content publisher	Nature Publishing Group
Licensed content publication	Nature Nanotechnology
Licensed content title	Symmetry and magnitude of spin-orbit torques in ferromagnetic heterostructures
Licensed content author	Kevin Garello, Ioan Mihai Miron, Can Onur Avci, Frank Freimuth, Yuriy Mokrousov, Stefan Blügel
Licensed content date	Jul 28, 2013
Volume number	8
Issue number	8
Type of Use	reuse in a dissertation / thesis
Requestor type	academic/educational
Format	print and electronic
Portion	figures/tables/illustrations
Number of figures/tables/illustrations	1
High-res required	no
Figures	Figure 1 (b)
Author of this NPG article	no
Your reference number	None
Title of your thesis / dissertation	PURE SPIN CURRENT IN LATERAL STRUCTURES
Expected completion date	Dec 2015
Estimated size (number of pages)	170

Reprint Permission for Chapter 4 and Figure 4.1-4.4:

[Notice]

If you are the one of the authors of the paper, you don't have to apply for a permission with the following conditions.

1. Follow the Copyright Policy of the Japan Society of Applied Physics
2. A credit line of "Copyright (published year) The Japan Society of Applied Physics" should be added to the end of the figure caption in the Content.
3. The Content must be cited as a reference in the Publication.

/_____/
To: President of the Japan Society of Applied Physics
Day Month Year

Submit to:
Publication Center for Pure and Applied Physics, The Japan Society of Applied Physics
2-31-22-5F, Yushima, Bunkyo-ku, Tokyo 113-0034, Japan
TEL: +81-3-5844-3291 FAX: +81-3-5844-3290 E-mail address: permission@jsap.or.jp

Application for Permission to Reproduce Material

I request permission to reproduce the following material, copyrighted by the Japan Society of Applied Physics.

Publication where material is reproduced (the Publication)

Name of the Publication (e.g., journal title, book title):
Publisher (e.g., publishing company):
Planned date of publication:
Number of copies:

Content of reproduction (the Content)

Journal title:
Volume/Year/ID(starting page): / /
Article title:
Author(s):
Content to be reproduced (please specify):

Applicant (only to be completed by the author of the Publication)

Name:

Affiliation (e.g., university, company, organization):

E-mail address:

I will abide by the following conditions of reproduction.

1. A credit line “Copyright *publication year* The Japan Society of Applied Physics” must be added to the Content (in the figure caption(s)). The material containing the Content, copyrighted by the Japan Society of Applied Physics, must be cited in the references of the Publication.
2. The Content will not be modified.
3. The Content will not be reproduced in other materials.

Signature of applicant:_____

* The purpose of reproduction will be considered before permission is granted.

ENDORSEMENT

Dr.

I permit the reproduction of the Content in the Publication.

...../...../.....

Day Month Year

President, The Japan Society of Applied Physics

Reprint Permission for Chapter 5:

AIP PUBLISHING LLC LICENSE
TERMS AND CONDITIONS

Oct 26, 2015

All payments must be made in full to CCC. For payment instructions, please see information listed at the bottom of this form.

License Number	3736600618487
Order Date	Oct 26, 2015
Publisher	AIP Publishing LLC
Publication	Journal of Applied Physics
Article Title	Asymmetric spin absorption across a low-resistance oxide barrier
Author	Shuhan Chen,Chuan Qin,Yi Ji
Online Publication Date	Jul 17, 2015
Volume number	118
Issue number	3
Type of Use	Thesis/Dissertation
Requestor type	Author (original article)
Format	Print and electronic
Portion	Excerpt (> 800 words)
Will you be translating?	No
Title of your thesis / dissertation	PURE SPIN CURRENT IN LATERAL STRUCTURES
Expected completion date	Dec 2015
Estimated size (number of pages)	170
Total	0.00 USD

Reprint Permission for Figure 5.1-5.4:

AIP PUBLISHING LLC LICENSE
TERMS AND CONDITIONS

Oct 26, 2015

All payments must be made in full to CCC. For payment instructions, please see information listed at the bottom of this form.

License Number	3736600729762
Order Date	Oct 26, 2015
Publisher	AIP Publishing LLC
Publication	Journal of Applied Physics
Article Title	Asymmetric spin absorption across a low-resistance oxide barrier
Author	Shuhan Chen,Chuan Qin,Yi Ji
Online Publication Date	Jul 17, 2015
Volume number	118
Issue number	3
Type of Use	Thesis/Dissertation
Requestor type	Author (original article)
Format	Print and electronic
Portion	Figure/Table
Number of figures/tables	4
Title of your thesis / dissertation	PURE SPIN CURRENT IN LATERAL STRUCTURES
Expected completion date	Dec 2015
Estimated size (number of pages)	170
Total	0.00 USD

Reprint Permission for Chapter 6:

AIP PUBLISHING LLC LICENSE
TERMS AND CONDITIONS

Oct 26, 2015

All payments must be made in full to CCC. For payment instructions, please see information listed at the bottom of this form.

License Number	3736601124141
Order Date	Oct 26, 2015
Publisher	AIP Publishing LLC
Publication	Journal of Applied Physics
Article Title	Large spin accumulation near a resistive interface due to spin-charge coupling
Author	Shuhan Chen,Han Zou,Siu-Tat Chui, et al.
Online Publication Date	Dec 11, 2013
Volume number	114
Issue number	22
Type of Use	Thesis/Dissertation
Requestor type	Author (original article)
Format	Print and electronic
Portion	Excerpt (> 800 words)
Will you be translating?	No
Title of your thesis / dissertation	PURE SPIN CURRENT IN LATERAL STRUCTURES
Expected completion date	Dec 2015
Estimated size (number of pages)	170
Total	0.00 USD

Reprint Permission for Figure 6.1-6.9:

AIP PUBLISHING LLC LICENSE
TERMS AND CONDITIONS

Oct 26, 2015

All payments must be made in full to CCC. For payment instructions, please see information listed at the bottom of this form.

License Number	3736601181882
Order Date	Oct 26, 2015
Publisher	AIP Publishing LLC
Publication	Journal of Applied Physics
Article Title	Large spin accumulation near a resistive interface due to spin-charge coupling
Author	Shuhan Chen,Han Zou,Siu-Tat Chui, et al.
Online Publication Date	Dec 11, 2013
Volume number	114
Issue number	22
Type of Use	Thesis/Dissertation
Requestor type	Author (original article)
Format	Print and electronic
Portion	Figure/Table
Number of figures/tables	9
Title of your thesis / dissertation	PURE SPIN CURRENT IN LATERAL STRUCTURES
Expected completion date	Dec 2015
Estimated size (number of pages)	170
Total	0.00 USD

Reprint Permission for Chapter 7:

AIP PUBLISHING LLC LICENSE
TERMS AND CONDITIONS

Oct 26, 2015

All payments must be made in full to CCC. For payment instructions, please see information listed at the bottom of this form.

License Number	3736600897805
Order Date	Oct 26, 2015
Publisher	AIP Publishing LLC
Publication	Applied Physics Letters
Article Title	Efficient room temperature spin-Hall injection across an oxide barrier
Author	Shuhan Chen,Chuan Qin,Yi Ji
Online Publication Date	Aug 26, 2014
Volume number	105
Issue number	8
Type of Use	Thesis/Dissertation
Requestor type	Author (original article)
Format	Print and electronic
Portion	Excerpt (> 800 words)
Will you be translating?	No
Title of your thesis / dissertation	PURE SPIN CURRENT IN LATERAL STRUCTURES
Expected completion date	Dec 2015
Estimated size (number of pages)	170
Total	0.00 USD

Reprint Permission for Figure 7.1-7.4:

AIP PUBLISHING LLC LICENSE
TERMS AND CONDITIONS

Oct 26, 2015

All payments must be made in full to CCC. For payment instructions, please see information listed at the bottom of this form.

License Number	3736600958948
Order Date	Oct 26, 2015
Publisher	AIP Publishing LLC
Publication	Applied Physics Letters
Article Title	Efficient room temperature spin-Hall injection across an oxide barrier
Author	Shuhan Chen,Chuan Qin,Yi Ji
Online Publication Date	Aug 26, 2014
Volume number	105
Issue number	8
Type of Use	Thesis/Dissertation
Requestor type	Author (original article)
Format	Print and electronic
Portion	Figure/Table
Number of figures/tables	4
Title of your thesis / dissertation	PURE SPIN CURRENT IN LATERAL STRUCTURES
Expected completion date	Dec 2015
Estimated size (number of pages)	170
Total	0.00 USD